Pieces to the puzzle of Galaxy Formation

Thesis for the degree of Doctor of Philosophy

Johan P. U. Fynbo

Institute of Physics and Astronomy
University of Århus

January 2000

Contents

Preface

Thus, while the mute creation downward bend
Their sight, and to their earthly mother tend,
Man looks aloft; and with erected eyes
Beholds his own hereditary skies.
From such rude principles our form began;
And earth was metamorphos'd into Man.

Ovid 'Metamorphoses' (the last six verses from book 1)

This thesis is submitted to the Faculty of Natural Sciences at the University of Århus, Denmark, in order to fulfill the requirements for the degree of Ph.D. The thesis is based mainly on observations made with ground based optical telescopes during the last four years. Chapters 8 and 9 are based on Hubble Space Telescope data. The analysis of the data have been done mainly by me under supervision of Dr. P. Møller and Dr. B Thomsen.

The outline of the thesis is as follows. I shall start in Chapter 1 by giving an introduction to the basic framework of structure formation, in particular to galaxy formation and so called Damped Lyα Absorbers. In Chapter 2 I briefly describe some of the methods central to the work presented in this thesis. Chapters 3–9 present the main results of this thesis in the form of papers that are either published (Chapters 3, 4, 6, 7 and 9), submitted (Chapter 5) or in preparation (Chapter 8). Hence, the papers that constitute Chapter 5 and 8 do not appear in their final form. The only changes that has been added to the published papers are *i)* the references (which have been updated) and *ii)* the figure sizes. Finally in Chapter 10 the thesis is concluded with a summary and outlook.

List of Publications

- "Extended Emission from a damped absorber at z = 1.9 : The size of a DLA", **Fynbo J.U.**, Møller P., and Warren S.J., In : Proceedings of the 13th IAP Colloquium, 'Structure and Evolution of the IGM from QSO Absorption Lines', eds. P. Petitjean, S. Charlot (Editions Frontiere), p.408
- "On the nature of $z_{abs} \approx z_{em}$ Damped Lyα Absorbers in quasar spectra", Møller P., Warren S.J., and **Fynbo, J.U.**, 1998, A&A **330**, 19
- "Optical and near-infrared follow-up observations of GRB980329", Palazzi E., Piau E., Masetti N., et al., 1998, A&A **336**, L95
- "The Gas Reservoir for present day Galaxies : Damped Lyα Absorption Systems", **Fynbo J.U.**, Thomsen B., and Møller P., In : Proceedings of the June 1998 Vatican Symposium, "Astrophysics Research and Science Education", ed. C. Impey, (Notre Dame Press), p. 237
- "Science Education in a Nordic Welfare State", **Fynbo J.U.**, In : Proceedings of the June 1998 Vatican Symposium, "Astrophysics Research and Science Education", ed. C. Impey, (Notre Dame Press), p. 40
- "Finding typical high redshift galaxies with the NOT", **Fynbo J.U.**, Møller P., and Thomsen B., In : Proceedings of the conference held in Turku 1998 "Astrophysics with the NOT", eds. H. Karttunen and V. Piirola (Silverprint), p. 109
- "NTT service mode observations of the Lyman Limit Absorber towards Q1205-30", **Fynbo J.U.**, Thomsen B., and Møller P., *The Messenger* **95**, 32
- "Extended Lyα emission from a damped absorber at z = 1.93, and the relation between DLAs and Lyman-break galaxies", **Fynbo J.U.**, Møller P., and Warren S.J., 1999, MNRAS **305**, 849
- "Lyα Emission from a Lyman Limit Absorber at z=3.036", **Fynbo J.U.**, Thomsen B., and Møller P., 2000, A&A **353**, 457

- "Clustering of Galaxies at faint magnitudes",
  Fynbo J.U., Freudling W., and Møller P., 1999, A&A accepted

- "The Host Galaxy of Q0151+048A",
  Fynbo J. U., Burud I., Møller P., In the proceedings for the conference 'Lifecycles of radio galaxies', Baltimore, 1999, in press

- "The sources of extended continuum emission towards Q0151+048A : The host galaxy and the Damped Lyα Absorber",
  Fynbo J.U., Ingunn B., and Møller P., 1999, A&A submitted

- "Discovery of the optical counterpart and early optical observations of GRB990712",
  Sahu K.C., Vreeswijk P., Bakos G. et al., 2000, ApJ in press

Chapter 1

Introduction

The question underlying all the work presented in this thesis is how the universe evolved from an extremely homogeneous state roughly 10^5 years after the Big Bang to the very lumpy universe we see today. In this introduction I will first briefly describe the general framework for the study of structure formation in the universe. I will then introduce the concept of Quasi Stellar Object (QSO) absorption line systems and the so called Lyman α (Lyα) forest and describe how one can answer a variety of essential questions about structure formation through the study of QSO absorption line systems. From there I will focus on the study of the most highly gas rich QSO absorption line systems, so called Damped Lyα Absorbers, which for a number of reasons are prime candidates for being primeval galaxies. The study of Damped Lyα Absorbers will be the main subject of this thesis. I will then describe another population of primeval galaxies, termed Lyman Break Galaxies in the literature, and try to describe how one can bring together knowledge of Damped Lyα Absorbers and Lyman Break Galaxies to obtain a more complete understanding of early galaxies. Finally I will briefly describe what the study of clustering in the angular distribution of faint galaxies on the sky can tell us about structure formation.

1.1 From Quantum fluctuations to the Milky Way

One of the most important scientific discoveries of this century is that of the cosmic microwave background radiation. The results from the COBE mission (e.g. Fixen et al. 1996, 1997) show that the matter density ρ at the time when radiation decoupled from matter, though extremely homogeneous, had small density fluctuations at the level $\delta \equiv \frac{\Delta\rho}{\rho} \approx 3\times10^{-5}$. The inflation scenario suggests that these anisotropies originated from quantum fluctuations in a microscopic part of space-time that was inflated (through one or more phase transitions in the fundamental interactions a tiny fraction of a second after the big bang) into the macroscopic regime, and hence became our entire observable universe. Truly, this is a staggering scenario.

The aim of the study of structure formation is to gain insight into how the universe evolved from the very homogeneous state probed by COBE to the lumpy universe we see today containing large galaxy "walls", clusters and galaxies (see Guzzo (1999) for a recent and very thorough review about large scale structure). A crucial limitation to our understanding of the formation of structure is the fact that we do not know the nature of (by far the most) massive matter in the universe - the so called dark matter or hidden mass. Comparisons of predicted abundances from Big Bang Nucleosynthesis to measured abundances of the light elements (the stable isotopes of Hydrogen, Helium and Lithium) constrain the baryon contribution to the density (relative to the critical density) to be $\Omega_{baryon}h^2 = 0.019 \pm 0.001$, where h is the Hubble constant in units of 100 km s^{-1} Mpc^{-1} (e.g. Hannestad 1999). The contribution to Ω_m from luminous matter today is $<0.004\ h^{-1}$ (Fukugita et al. 1998). Hence, for a value $h = 0.7$, less than 15% of the baryons are found in stars within galaxies. The majority of baryons are today in hot, ionised plasma in groups and clusters of galaxies. However, the *total* density of matter is measured to be in the range Ω_m=0.1–0.5 (e.g. Bahcall & Fan 1998, Weinberg et al. 1999a), which means that more than 90% of the mass in the universe is in the form of non-baryonic dark matter. In fact, one of the strongest observational supports for the existence of dark non-baryonic matter is the low amplitudes of the primordial density fluctuations seen in the COBE data. No existing model considering only baryonic matter can account for the structure seen in todays universe (see Weinberg et al. 1999b for a review). Fortunately, the interaction controlling the build up of structure, namely gravity, is well known in the non-relativistic regime relevant for galaxy formation. It should be noted, however that rather ad hoc and non-covariant modifications of the theory of gravity exist which are considered by some to be more plausible than invoking dark matter (e.g. Milgrom 1983, McGaugh 1999). Furthermore, electromagnetic interaction and atomic/molecular physics are important for controlling the cooling of baryonic material that collapses into the potential wells formed by the dark matter. More specifically, it is possible to some extent to understand the characteristic masses and sizes of galaxies and clusters from the criteria that the gas cooling time should be smaller than the gravitational free fall time (Rees & Ostriker 1977).

The following subsections describe the theoretical approach to the study of structure formation.

1.1.1 Theoretical models

In general theoretical models for structure formation involve several steps. Of course, one has to assume an underlying cosmology, i.e. the values of the Hubble constant H_0, the matter density in units of the critical matter density Ω_m and the contribution to the density from the cosmological constant, Ω_Λ. The next step is to specify the initial spectrum of perturbations as a function of scale (or wavelength) λ. Normally this is expressed in terms of the *power*

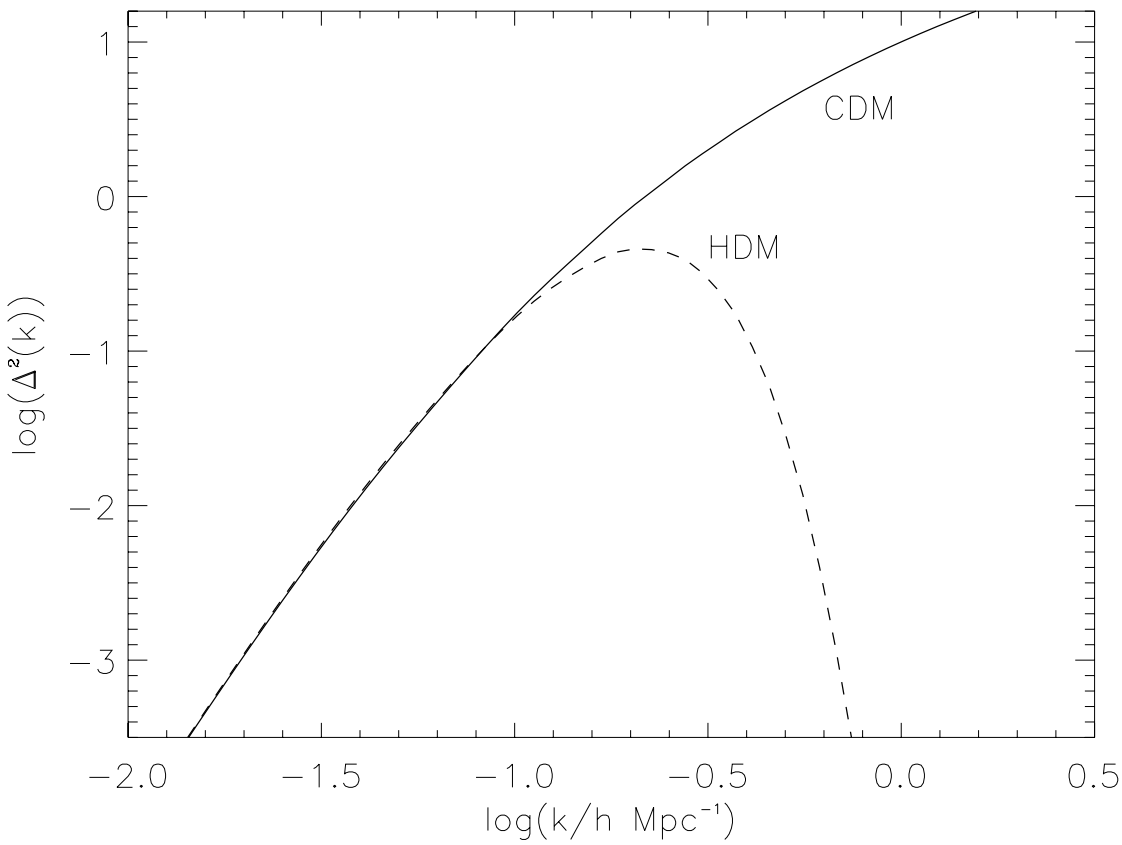

Figure 1.1: The dimensional power spectrum $\Delta(k) = \frac{k^3 P(k)}{2\pi^2}$ at the epoch of recombination for hot dark matter (HDM) and cold dark matter (CDM) assuming $\Omega_m = 1$ and $\Omega_\Lambda = 0$. The abscissa is normalized to the power measured by COBE at $\log(k) < -1.2$.

spectrum $P(k) = |\delta_k|^2$, where the wavenumber k is $\frac{2\pi}{\lambda}$ and δ_k is the Fourier transform of the spatial density contrast :

$$\delta_k \propto \int \delta(\vec{x}) \exp(i\vec{k} \cdot \vec{x}) d^3x. \tag{1.1}$$

From inflation the initial power spectrum is predicted to have a simple power-law form, $P(k) \propto k^n$, with n close to 1. The spectrum for $n = 1$ is called the Harrison-Zel'dovich spectrum.

When a fluctuation of wavelength λ enters the horizon, i.e. when the size of causally connected regions in the universe reach the size λ, it will be modulated by a variety of processes depending on the nature of the dark matter. By definition *hot* dark matter (HDM) particles moved at relativistic velocities at the time (roughly one year after the Big Bang) when the horizon of the observable universe encompassed a mass of 10^{12} $M_\odot$, which corresponds to the mass of a large galaxy halo today. In the contrast, *cold* dark matter (CDM) particles moved at non-relativistic velocities at this time (see e.g. Larsen 1996, Kolb & Turner 1994).

For hot dark matter particles X which contribute Ω_X to the total density and have temperature T_X, fluctuations at comoving scales smaller than $\approx 30(\Omega_X h^2)^{-1}(T_X/T)^4$ Mpc, where T is the photon temperature, will be smeared out by free-streaming (e.g. Kolb & Turner 1994). Free-streaming means that the particles move freely and hence stream out of overdense regions and into underdense regions, in the process smoothing out inhomogeneities. For cold dark matter this will not happen and structure can build up also at the smallest scales. Fig. 1.1 shows the COBE normalized dimensionless power spectra $\Delta(k) = \frac{k^3 P(k)}{2\pi^2}$ predicted from the Harrison-Zel'dovich spectrum for both HDM and CDM at the time of recombination (assuming $\Omega_m = 1$ and $\Omega_\Lambda = 0$), roughly 3×10^5 years after the Big Bang.

From the time of recombination until today the perturbations developed under gravity. This process is normally simulated numerically using N-body computer codes. The resulting build-up of structure is again strongly dependent on the nature of the dark matter. In the CDM scenario, structures at small scales form first and the larger structures form later (so called hierarchical clustering), whereas in the HDM scenario structures at larger scales will form first since the seeds for the build-up of structure on smaller scales have been erased by free-streaming. Structure at smaller scales forms later by fragmentation. Finally, to compare the models with observations the concept of *biasing* is introduced. Bias is generally introduced as the relation between the standard deviation of the density contrast of galaxies $\sigma(\delta_g)$ and the standard deviation of the density contrast of dark matter halos $\sigma(\delta_{DM})$, $\sigma(\delta_g) = b \times \sigma(\delta_{DM})$. The bias parameter b may be a function of both time and scale. In all, it is far from trivial to compare observations with models.

I now describe the concept of QSO absorption line systems and show how they can provide essential information for the study of structure formation.

1.1.2 Lyα absorption line systems

A very promising method for obtaining observational insight into evolution of large scale structure in the universe at redshifts $z < 5$, corresponding to a look back time of 90–95% of the age of the universe, is based on the study of absorption lines in the spectra of high redshift QSOs. QSOs are very brigt, and therefore it is relatively inexpensive with todays large telescopes to obtain high signal–to–noise and high resolution spectra of them. The QSO absorption lines are mainly due to gas intersecting the line of sight to the QSOs. For example Fig. 1.2 shows a spectrum of the $z = 3.6$ QSO Q1422+231 (Kim et al. 1997). The emission line at 5590Å, seen in the lower panel, is Lyα from the QSO. Bluewards of this can be seen a very large number of absorption lines, almost all of which are due to neutral hydrogen in clouds along the line of sight to the QSO. These absorption lines are denominated 'the Lyα forest' (see Rauch 1998 for a review). The lines in the region redwards of the Lyα emission line, of which a 100Å region is shown in the upper panel, are due to metal ions, mainly CIV and SiIV, associated with some of the stronger Lyα systems (see

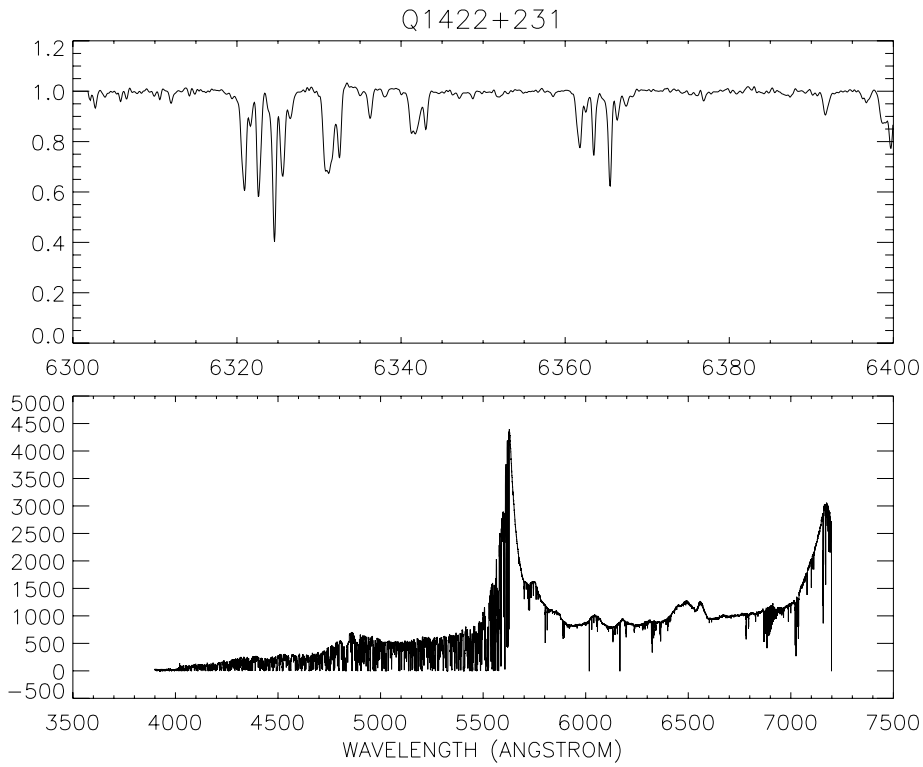

Figure 1.2: The spectrum of Q1422+231 from Kim et al. (1997). The units on the y-axis are flux units.

below). These lines are believed to originate in extended galactic halos or gas expelled from galaxies.

Fig. 1.3 shows the number of clouds per unit z and unit HI column density (N_{HI}) as a function of N_{HI} from a study by Hu et al. (1995). As seen, the Lyα absorption line systems are detected with N_{HI} ranging from $10^{12.5}$ cm^{-2} to $10^{21.8}$ cm^{-2}. At a redshift of 3, $N_{HI} = 10^{12.5}$ cm^{-2} corresponds to a baryonic overdensity δ smaller than 1 for a structure of dimensions $\approx$ 100 kpc, whereas, $N_{HI} = 10^{21}$ cm^{-2} corresponds to the present column density of mass in stars and gas in the Galaxy. Lyα absorption line systems are found from redshifts $z \approx 0$ to z $\approx$ 4.5 (Wolfe et al. 1995,, Lanzetta et al. 1995, Storrie-Lombardi et al. 1997). The density of baryons in the Lyα forest clouds at high redshifts is consistent with the predicted baryon abundance from Big Bang Nucleosynthesis (Rauch et al. 1997). By far (>90%) the majority of these baryons are found in highly ionized gas in the low column density systems, whereas almost all the *neutral* gas is in the highest column density systems with $N_{HI} \gtrsim 10^{20}$ cm^{-2}. This is seen from the following argument : the number dn of clouds with column density in the interval $[N, N + dN]$ is proportinal to N^{β} ($\frac{dn}{dN} \propto N^{\beta}$) with $\beta \approx -1.5$. The neutral gas content is proportional to the integral of $N \times \frac{dn}{dN}$, hence the integrand is proportinal to $N^{-0.5}$ and the integral will be dominated by its upper limit.

By looking for metal absorption at the redshifts of known Lyα absorption lines it is

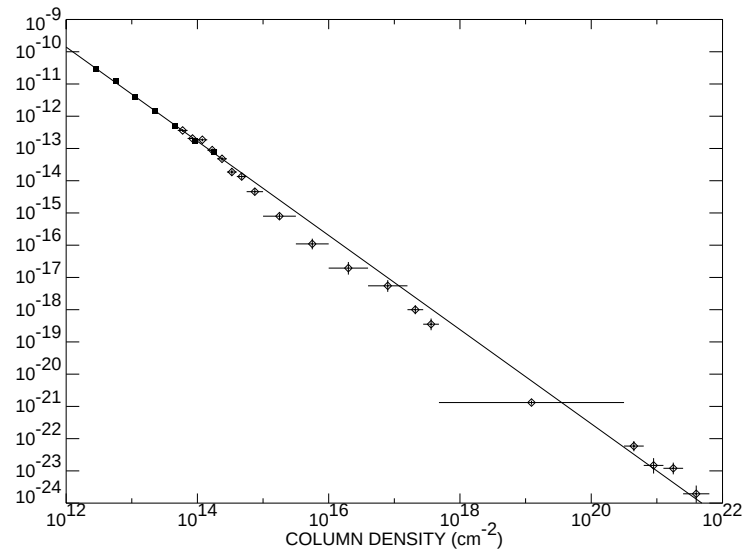

Figure 1.3: The number of clouds per unit z and unit N_{HI} as a function of N_{HI}. The units on the y-axis are cm^2.

possible to study the metallicity of QSO absorption line systems. Nearly all systems with HI column densities larger than 10^{15} cm^{-2} have associated metal absorption mainly due to SiIV and CIV with extracted abundances of Carbon roughly 10^{-2} of the solar abundance and roughly 3×10^{-2} of the solar abundance for Silicium (Songaila et al. 1996). About 50% of all systems with N(HI)>$10^{14.5}$ cm^{-2} have associated CIV absorption, whereas it is unclear whether even fainter absorption systems have associated metal absorption (Ellison et al. 1999). As the HI column density rises above 10^{19} cm^{-2} the gas becomes predominantly neutral and many low ionization metal lines appear. I will in the next section 1.2 describe what is known about the metallicity of these systems.

Recently is has been shown that the power spectrum $P(k)$ at scales 2-12 comoving h^{-1} Mpc can be determined directly from Lyα forest measurements (Croft et al. 1998, 1999, Phillips et al. 2000). The result of these measurements supports the CDM model for Ω_m=0.4.

In conclusion the study of Lyα absorption line systems can provide information on structure formation and the evolution of element composition for a wide range of systems; from very dilute clouds only slightly denser than the mean, to very dense clouds with column densities similar to those of present day galaxies, and also from when the universe was less than 5–10% of its age to the present day.

I will now describe how to find galaxies in the Lyα forest.

1.2 Damped Lyα Absorbers

The main subject of this PhD project is the study of the nature of the rare high HI column density absorption line systems seen in the lower right corner of Fig. 1.3. Primarily the study is concerned with the Damped Lyα Absorbers (DLAs, Wolfe et al. 1986). Wolfe et al. (1986) initiated a survey for signatures of primeval galaxies in the spectra of QSOs. Motivated partly by observations of the HI column densities of local spiral galaxies and partly by the demand that DLAs should be relatively unambiguously identifiable in low resolution spectra of QSOs they defined DLAs as systems with $N_{HI} > 2\times10^{20}$ cm^{-2}. Hence, DLAs are *per definition* prime candidates for being primeval galaxies.

An example of a high resoltion spectrum of an absorption line caused by a DLA at the redshift $z = 2.8268$ towards the z = 3.2 QSO Q1425+6039 is shown in Fig. 1.4 (Lu et al. 1996). A broad absorption trough centred at 4652Å, which is the wavelength of redshifted

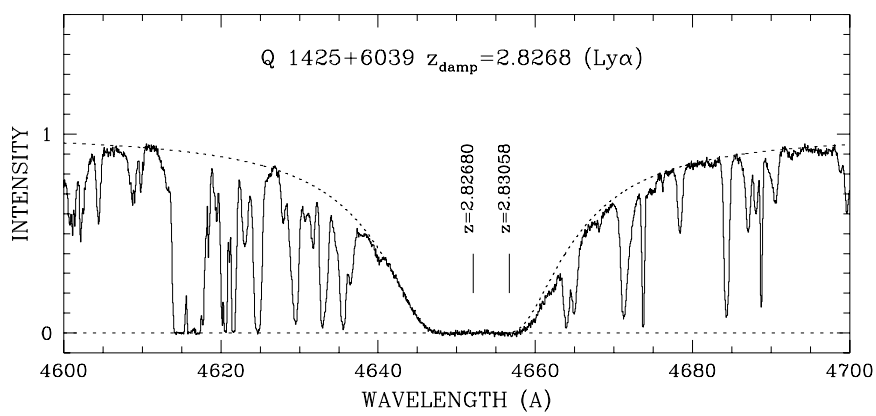

Figure 1.4: The damped Lyα line in the spectrum of Q1425+6039. The dotted line shows a fit to the data for $N_{HI} = 2\times10^{20}$ cm^{-2}.

Lyα (1215.67Å), can be seen. DLAs owe their name to the broad damping wings seen on the sides of the trough. The column density of this absorber is $N_{HI} = 2\times10^{20}$ cm^{-2}. The other redshift indicated (z = 2.83058) is that of a second component with $N_{HI} = 1\times10^{19}$ cm^{-2}.

At the present time approximately 100 DLA systems are listed in the literature (Wolfe et al. 1995, Lanzetta et al. 1995, Storrie-Lombardi et al. 1997). From studies of the spectra of the underlying QSOs, one can derive information about the average cross-section, the metallicities and the gas dynamics of the different regions of DLAs probed by ions in different ionization stages.

I will now review the current knowledge of DLAs. The essential questions are : What is the baryon content of DLAs compared to baryon content of present day galaxies? What are the typical metallicities of DLAs? What is the nature of typical galaxy counterparts of

DLAs?

1.2.1 The redshift density of DLAs and their contribution to Ω_m

The relation between the redshift density $\frac{dn}{dz}$ of absorption systems along the line of sight to a QSO (i.e. the number of absorption systems in the range z to $z + dz$) and the comoving space density $n_{abs}(z)$ and cross-section σ_{abs} for the population of objects responsible for the absorption is given by Eq. A.2 in appendix A. The most recent measurements of $\frac{dn}{dz}$ for DLAs at high redshift are in Wolfe et al. (1995) and Storrie-Lombardi et al. (1996). Because Eq. A.2 for $\Omega_\Lambda = 0$ and $\Omega_m = 1$ is a power law in $(1+z)$, it is customary to represent the number density as :

$$\frac{dn}{dz} = N_0\,(1+z)^\gamma. \tag{1.2}$$

Wolfe et al. and Storrie-Lombardi et al. derive the following fits to their measured number densities of DLAs as a function of redshift :

$$\begin{aligned} N_0 &= 0.055 \pm 0.007,\ \ \gamma = 1.15 \pm 0.55 \quad (Wolfe) \\ N_0 &= 0.04,\ \ \gamma = 1.3 \pm 0.5 \quad (Storrie - Lombardi). \end{aligned} \tag{1.3}$$

Since $\frac{dn}{dz}$ depends on the product of number density $n_{abs}(z)$ and the cross-section for absorption σ_{abs} it is not possible to derive both of these quantities from the observations. However, from the column density distribution and redshift density it is possible to measure the total amount of neutral baryons in DLAs as a function of redshift. This can be seen qualitatively from the following argument : $\frac{dn}{dz}$ is proportional to the probability of intersecting a DLA at redshift z with a random line of sight. This probability is in turn proportional to the total solid angle of DLAs at redshift z across the sky. Assuming a specific cosmological model this solid angle can be converted to an area, and when we integrate the HI column density distribution over this area we obtain the total amount of neutral hydrogen in DLAs at redshift z. The exact expression for $\Omega(HI)$ can be derived following Longair (1998) and using Appendix A :

$$\begin{aligned} \Omega_{HI}(z) &= \frac{\mu m_H}{\rho(z)_{crit}} \frac{dz}{dr_{prop}} \int_{N_{min}}^{N_{max}} N f(N,z) dN \\ &= \frac{8\pi G \mu m_H}{3H_0^2 c} \frac{\sqrt{(1+z)^2(\Omega_m z + 1) - \Omega_\Lambda z(z+2)}}{(1+z)^2} \int_{N_{min}}^{N_{max}} N f(N,z) dN, \end{aligned} \tag{1.4}$$

where H_0 is the Hubble constant, μ is the mean molecular weight of the gas (1.3 for 75% Hydrogen and 25% Helium), m_H is the mass of a Hydrogen atom, ρ_{crit} is the current critical density for closure of the universe, N_{min} is the lower limit of 2×10^{20} cm^{-2} defining of DLAs, N_{max} is the maximum column density for DLAs (which is a rather ill defined quantity) and $f(N,z)$ is the column density distribution function. Values of Ω_{HI} at various redshift

ranges are presented in Wolfe (1986a), Wolfe et al. (1995), Storrie-Lombardi et al. (1996), and Priyamvada & Pettini (1997). All these measurements consistently support a scenario, where Ω_{HI} at $z \approx 4$ is similar to the present day contribution to Ω_m from luminous matter and where Ω_{HI} from $z = 3$ to $z = 0$ steadily decline to reach the present day contribution to Ω_m from neutral gas in galaxies as measured by Rao & Briggs (1993). In other words, DLAs are consistent with being the baryon reservoir out of which the stars in present day galaxies formed (Wolfe 1986). The measured decline is in broad agreement with models of chemical evolution of galaxies (e.g. Pei et al. 1999). Very recently, this scenario has been questioned by new measurements of Ω_{HI} at $z < 1.7$, which suggest that Ω_{HI} is declining significantly less rapidly than previously thought (Rao & Turnshek 1999). Here it should be emphasized, that the number of baryons in highly ionized gas is roughly 10 times larger than the number of baryons in DLAs. Hence, even a small change in the degree of ionization of the total distribution of baryons, e.g. due to a change in the intensity of the UV-background, can have a dramatic impact on the evolution of Ω_{HI}.

1.2.2 Metallicity and dust

One of the large advantages of DLAs for the study of the formation and early evolution of galaxies is the fact that it is relatively easy to measure even very small abundances of ions in them. This is done by studying absorption lines due to metal-ions in the DLA in the spectrum of the background QSO. By comparing the abundance patterns in DLAs with the abundance patterns in population I and II stars, we can infer the main source of metal production in DLAs, and by studying the metallicity of DLAs at different redshifts we can constrain the cosmic history of metal enrichment.

Lu et al. (1996) present a thorough and comprehensive study of the abundances of 11 chemical elements in 14 DLAs in the redshift range $0.7 < z < 4.4$. The abundance ratio (Fe/H) for these DLAs falls in the range 1/10 to 1/300 of the solar ratio with a tendency that the lowest metallicities are found at highest redshifts as expected if DLAs are primeval galaxies that gradually evolve into the range of galaxies we see locally. Lu et al. argue that the abundance patterns are consistent with Type II supernovae metal production and show no or only very little depletion of metals onto dust grains. However, these later two conclusions have been disputed by Kulkarni et al. (1997) who find that the same data are consistent with a disc star abundance pattern with a dust-to-metal ratio equal of 40-90% of that in the Milky Way, and not with an undepleted halo star abundance pattern. Pettini et al. (1994, 1997a, 1997b, 1999) study the abundance of Zn and Cr in a large sample of DLAs in the redshift range $0.7 < z < 3.4$. The electron configuration of Zn is $[Ar]3d^{10}4s^2$, i.e. a filled 3d orbital and a filled 4s orbital. On the other hand the electron configuration of Cr is $[Ar]3d^5 4s^1$, i.e. a half full 3d orbital and a half full 4s orbital. Hence, Zn and Cr are expected to have very different chemical properties. In galactic clouds along the lines of

sight to halo stars Zn and Cr are observed to both trace Fe. However, Zn depletes very little onto dust grains whereas Cr depletes strongly onto dust (see also Sembach et al., 1995). Based on these empirical relations Pettini et al. measure (or derive upper limits to) the metallicities and dust contents of the DLAs in their sample. They derive a mean metallicity of 1/15 of solar metallicity and a mean dust-to-gas ratio of about 1/30 of the Milky Way value. Both quantities have a large scatter. Similar results have been found by Prochaska & Wolfe (1999).

Both Prochaska & Wolfe (1999) and the most recent work of Pettini and collaborators do not detect significant evolution of metallicity with redshift. This is contrary to recent work by Savaglio et al. (2000) who find that the mean metallicity of DLAs increases from 1/30 of solar metallicity at $z \approx 4$ to 3/5 of solar metallicity at $z \approx 0.5$. I am not able to judge, which of the authors that are most likely in error (if any), but I will refer to the comment by Savaglio et al. who state that their detection of evolution would not have been significant if they had only studied Zn.

In a very recent study Centurion et al. (2000) estimate the alpha/Fe ratio from measurements of the [S/Zn] abundance ratio in 11 DLAs. They find that although [S/Zn] decreases with increasing metallicity [Zn/H], the observed [S/Zn] ratios are not similar to those of metal–poor stars at comparable metallicity in the galactic halo. This indicates that DLAs form stars at a lower rate than the early Milky Way.

Two issues are important for the above results. The first issue is the question of the presence of molecular hydrogen in DLAs. If a significant fraction of the hydrogen is in the molecular phase then the metallicities and dust contents will be overestimated. However, only for two DLAs at high redshifts have lines (from molecular hydrogen H_2) been detected. In one of these the fraction of hydrogen in molecular form was 0.22±0.05 (Ge & Bechtold 1997), in the other 10^{-5}–10^{-4} (Levshakov & Varshalovich 1985, Foltz et al. 1988, Srianand & Petitjean 1998). More observations are needed to constrain the amount of molecules in DLAs. Two claimed detections of CO emission from DLAs (Brown & Vanden 1993, Frayer et al. 1994) were both not confirmed by later observations (Braine et al. 1996, Ivison et al. 1998). The second issue is the question of the presence of ionized gas in DLAs. If a significant fraction of the hydrogen is ionized then the metallicities and dust-to-gas ratio will also be overestimated. Howk & Sembach (1999) find that the presence of ionized gas leads to systematically overestimated abundances in the lowest column density DLAs.

Pei, Fall and Bechtold (1991) used a completely independent method to measure the amount of dust in DLAs. By comparing the spectral slopes of a sample of QSOs with intervening DLAs to the spectral slopes of QSOs in a control sample they measured a significant reddening due to DLAs. The derived dust-to-gas ratio was 5%–20% of the Milky Way value. Finally Knudsen (2000) compare the broad band colours of a sample of QSOs with intervening DLAs with the broad band colours of a control sample of QSOs without intervening

DLAs. The reddening of the QSOs in the DLA sample is consistent with a dust–to–gas ratio of 25%–80% of the Milky Way value; a rather surprising result.

1.2.3 Information from the velocity profiles of the absorption lines

Very little is known about the sizes and morphologies of DLAs. It is a long standing controversy whether DLAs are large rotationally supported spiral discs or rather, as in CDM models, small galaxy subunits that later, through merging, build up the galaxies we see today (e.g. Haehnelt et al. 1998 and references therein). The velocity profiles of low ionisation metal lines due to DLAs has been the subject of quite intense study aimed at resolving this controversy about the nature of DLAs.

Prochaska & Wolfe (1997, 1998) argue, from so-called edge leading asymmetries in 31 low ionization line velocity profiles, that DLAs are rapidly rotating thick discs, and that the profiles are highly inconsistent with the predictions of CDM models. However, these results have been cast in doubt by the work of Haehnelt et al. (1998) who show that similar edge leadingly assymmetric velocity profiles are predicted from CDM models with a proper hydrodynamic treatment of the gas. Lu et al. (1997) examine two DLAs for which they argue that the systemic redshift has been found from the Lyα emission line. Using this they find evidence for rotation in one of the two, but not the other. It is fair to say that the evidence from velocity profiles at present is inconclusive about the nature of DLAs.

1.2.4 Narrow band imaging and long slit spectroscopy

A more direct way of examining the size and morphology of DLAs is the study of their emission. The technique which has been used in the main part of the observational work of this thesis is narrow band imaging. By performing imaging in a filter tuned to Lyα at the redshift of the absorber and with a filter width similar to the equivalent width of the damped absorption line, one circumvents the problem of the strong emission from the QSO, which is typically only 0–3 arcsec away from the line of sight to the DLA. However, due to the damped absorption line the QSO emission will be almost completely absent in the narrow band image making the DLA itself, if it is a Lyα *emitter*, stand out. For DLAs at redshifts $z < 4$ Lyα falls at $\lambda < 5000$Å, where the sky background is very low during dark time (near new moon). By using long exposure times and suitable binning of the detector, one can reduce the combined detector and sky noise and obtain very faint detection limits for Lyα (see Chapter 2). Long slit spectroscopy also gains from the low background and the removal of QSO light by the damped absorption line, but the drawback is the limited sky coverage. The probability that the slit will miss the DLA is high (e.g. Bunker et al. 1999).

A very important question is accordingly how and when Lyα photons are produced. Lyα photons are produced when hydrogen recombines. Hence, the production of Lyα photons in

galaxies is directly related to the production of ionizing UV-photons ($\lambda < 912$ Å). For regions with large optical depth for hydrogen absorption (so called case B recombination) 68% of all ionizing photons produce a Lyα photon. The flux of ionizing photons is in turn proportional to the presence of young massive stars and hence the star formation rate (SFR). With the Kennicutt (1983) prescription SFR = L(Hα)/(1.12 x 10^{41} erg s^{-1}) $M_\odot$ yr^{-1} and assuming L(Lyα)/L(Hα)=10 (case B recombination) and negligible dust extinction, this leads to

$$SFR = L(Ly\alpha)/(1.12 \times 10^{42} ergs^{-1}) M_\odot \ yr^{-1} \tag{1.5}$$

For instance, assuming $z = 3$, Ω_m =0.3 and $\Omega_\Lambda = 0.7$ a flux of 1×10^{-17} erg s^{-1} cm^{-2}, which can be measured with current instrumentation, corresponds to a SFR of 0.3 h^{-2} $M_\odot$ yr^{-1}. Normal spiral galaxies today convert gas into stars at a rate of a few to 10 $M_\odot$ yr^{-1} (Kennicut 1983), hence Lyα imaging of DLAs can be successful even for DLAs forming stars at relatively modest rates.

Eq. 1.5 only provides a rough estimate of the SFR when dust extinction can be neglected. The shape of the initial mass function and the geometry of the Lyα photon escape paths add large uncertainties to this scaling. However, the crucial complication is the fact that even small amounts of dust will extinguish the Lyα flux. This is because the Lyα line is a resonant line for which resonant scattering dramatically increases the optical depth. Even a dust-to-gas ratio of 10% of the Milky Way value can decrease the Lyα flux by an order of magnitude (e.g. Charlot & Fall 1991, 1993).

Much telescope time has been dedicated to narrow band imaging and long slit spectroscopy of DLAs over the past decade (e.g. Møller & Warren 1993, Lowenthal et al. 1995, and references therein). Lowenthal et al. (1995) report null results in 11 DLA fields reaching a 5σ detection limit of 5×10^{-17} erg s^{-1} cm^{-2} from long slit spectroscopy and Fabry-Perot narrow band imaging (however, this was in rather poor conditions with seeing 2-3 arcsec). They do not confirm two (conflicting) earlier reports on detection of Lyα emission from the DLA towards Q0836+113 (Hunstead et al. 1990, Wolfe et al. 1992). Pettini et al. (1995) report on early results from a long slit spectroscopic survey of 21 DLAs reaching a 5σ detection limit of about 2×10^{-17} erg s^{-1} cm^{-2}. They report to have confirmed the Hunstead et al. (1990) detection towards Q0836+113 and report on a detection of Lyα emission from the DLA towards Q2059-360. This later detection has recently been confirmed (Robertson & Leibundgut 1998, Leibundgut & Robertson 1998). In 1993 Møller & Warren reported on a spectroscopically confirmed narrow band detection of Lyα emission from the DLA towards PKS0528-250. One of the results of this thesis is the detection of Lyα from another DLA, namely the DLA towards Q0151+048A (Chapter 4).

1.2.5 $z_{abs} \approx z_{em}$ DLAs

The DLAs towards Q2059-360, PKS0528-250 and Q0151+048A are all $z_{abs} \approx z_{em}$ systems for which the absorber redshift z_{abs} only differ by a few thousand km s^{-1} from the quasar emission redshift z_{em}. Most of the absorbers studied in this thesis are such $z_{\rm abs} \approx z_{\rm em}$ systems. We have decided to study this class of absorbers motivated primarily by *i)* the large number of null detections of emission from intervening DLAs as of primo 1996, which led us to study DLAs for which there were reasons to believe that they were stronger emitters than intervening absorbers (due to e.g. photoionisation by the QSO or induced star formation), and *ii)* the fact that the study of $z_{\rm abs} \approx z_{\rm em}$ systems might tell us something about the influence of QSOs on galaxy formation in their environments. Chapter 3 discusses the nature of $z_{\rm abs} \approx z_{\rm em}$ systems in more detail.

1.2.6 Results from Broadband imaging

In addition, two spectroscopically confirmed broad band detections of emission from high redshift DLA-absorbing galaxies have been published (Steidel et al. 1995a, Djorgovski et al. 1996, Djorgovski 1998), as well as a number of mainly low and intermediate redshift DLA candidates, which have not yet been confirmed by spectroscopy (Steidel et al. 1995b, Aragón-Salamanca et al. 1996, Le Brun et al. 1997). Finally, Chapter 8 presents some of the first results from a large survey for galaxy counterparts of DLAs conducted with the STIS[1] and NICMOS[2] instruments on the Hubble Space Telescope.

1.3 Lyman-break Galaxies (LBGs)

I now describe a completely different approach to the observational study of high redshift galaxies, which has recently proved extremely successful. This method is based on broad band imaging in a set of filters designed to identify star forming galaxies at redshifts above 3. In the spectrum of star forming galaxies there will be a strong discontinuity at the Lyman limit (restframe wavelength $\lambda = 912$Å corresponding to the ionization energy of 13.6eV for hydrogen) resulting in virtually no emission bluewards of the lyman limit. This discontinuity is normally in the literature refered to as the Lyman break. Steidel & Hamilton (1992) and collaborators have designed three special broad band filters optimized for the detection of galaxies for which the lyman break is redshifted into the observed near-ultraviolet. The samples of galaxies selected by this Lyman Break technique (Steidel & Hamilton 1992, Steidel et al. 1999) now contain roughly a thousand galaxies.

[1]Space Telescope Imaging Spectrograph.
[2]Near Infrared Camera and Multi-Object Spectrometer.

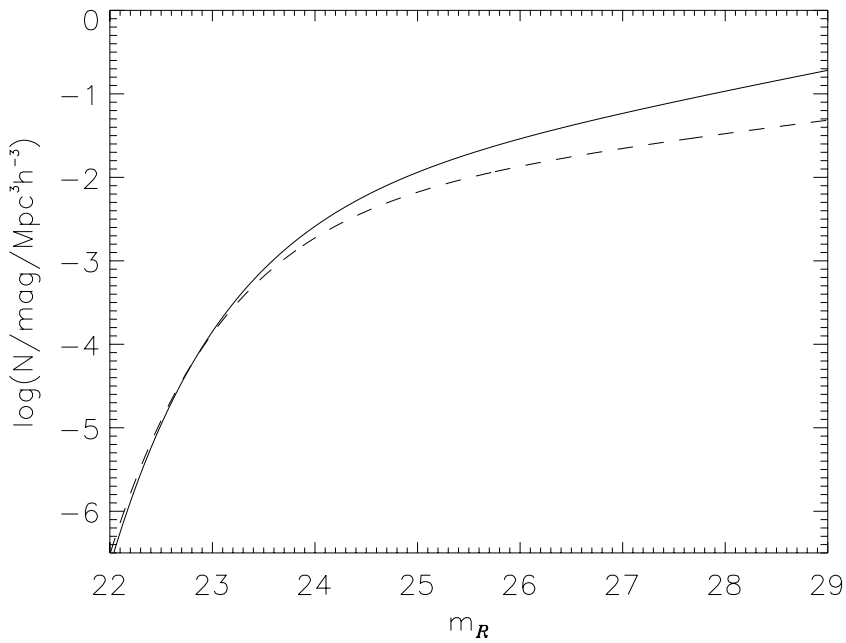

Figure 1.5: The two determinations of the Luminosity Function of Lyman Break Galaxies. The dashed line shows the Luminosity Function presented in Dickinson (1999), and the full drawn line shows the Luminosity Function presented in Steidel et al. (1999).

The Luminosity Function (LF) (number of objects per unit magnitude per cubic comoving Mpc as a function of magnitude) of LBGs was first presented by Dickinson (1999). For a Schechter parameterization of the LF (Schechter, 1976)

$$\Phi(L)dL = \Phi^* \left(\frac{L}{L^*}\right)^{\alpha} \exp\left(\frac{L}{L^*}\right) d\left(\frac{L}{L^*}\right), \tag{1.6}$$

Dickinson derived the following parameters : $\alpha = -1.38$, $\phi^* = 1.0 \times 10^{-2} h^3 Mpc^{-3}$ and $m^* = 24.45$. In order to add together information from the ground based survey and the Hubble Deep Field (HDF), Dickinson had to renormalize the counts in the HDF by a factor of 2.5. In Steidel et al. (1999) the LF was re-evaluated using a better determined effective volume, and in this new determination of the LF no renormalization was necessary. The parameters for a Schechter parameterization of this better determined LF are : $\alpha = -1.60 \pm 0.13$, $\phi^* = 1.6 \times 10^{-2} h^3 Mpc^{-3}$ and $m^* = 24.48 \pm 0.15$. The re-evaluated LF is significantly steeper and has a higher normalization ϕ^* than the LF of Dickinson (1999). Fig. 1.5 shows the luminosity functions of Dickinson (1999) and Steidel et al. (1999).

The LF was derived by both Dickinson and Steidel et al. assuming a $\Omega = 1$ and $\Lambda = 0$ universe. The effect of changing the cosmology is a stretching of the ordinat. The number density is inversely proportional to the volume element given in A.1. To derive the LF for a $\Omega = 0.3$ and $\Omega_\Lambda = 0.7$ universe the number densities (and hence ϕ^*) should be multiplied

by 0.25, which is the ratio between the volume element at z=3 for the two cosmologies.

The study of these Lyman Break Galaxies have lead to a tremendous progress in our understanding of the high redshift universe. In fact, the present knowledge about the emissivities, number densities, clustering and star formation rates of normal galaxies at high redshift is almost entirely based on studies of LBGs.

An obvious question is now how LBGs and DLAs relate to each other. The following section tries to adress this question.

1.4 The relation between DLAs and LBGs

A few studies have addressed the relation between DLAs and LBGs. Mo, Mao and White (1999) study the nature of LBGs from semi-analytical models of hierarchical structure formation. They conclude that the bright $R < 25.5$ LBGs from ground based surveys are likely to have only a small overlap with current samples of DLAs. This is because the highest star formation rates in their models predominantly occur in galaxies with low specific angular momentum, whereas the DLAs are biased towards systems with large specific angular momenta and smaller star formation rates. Another line of attack has been presented in a series of papers by Pei and Fall and collaborators (Pei & Fall 1995, Fall et al. 1996, Pei et al. 1999). These authors have setup a framework for combining information from the absorption statistics of DLAs, the integrated star formation rate of galaxies at different epochs (including the LBGs) and in the most recent paper also the integrated far-infra-red background. The result of their work is that it is possible to combine these different sources of information into a consistent picture of galaxy formation and evolution in which the cold gas in DLAs at high redshift is gradually turned into stars. Finally Fynbo, Møller and Warren (1999, Chapter 4 in this thesis) compare the absorption statistics of DLAs at $z = 3$ with the luminosity function of LBGs at $z = 3$ based on the ground based samples and the LBGs in the Hubble Deep Field (HDF) from Dickinson (1999) mentioned above. The result, though tentative due to the uncertainties in the determination of the luminosity function, of this comparison is that about 70% of DLAs at $z \approx 3$ must be fainter than $R = 28$. As this comparison is important, we shall repeat it here with the LF determined by Steidel et al. (1999) and also show how the comparison depends on cosmology.

We assume that every LBG lies at the centre of a DLA HI disc. To relate the LBG LF to observables of the DLA population we suppose that the size of the DLA disc R_{gas} (the radius beyond which the column density falls below 2 x 10^{20} cm^{-2}) is related to the galaxy luminosity by the Holmberg relation $R_{gas}/R^*_{gas} = (L/L^*)^t$. The average absorption cross-section $A(L)$ for a galaxy with luminosity L is then

$$\begin{aligned} A(L) &= \pi R(L)^2/2 \\ &= (\pi {R^*_{gas}}^2/2)(L/L^*)^{2t}. \end{aligned} \tag{1.7}$$

The value of R^*_{gas} is fixed so as to reproduce the observed line density of DLAs dn/dz given in Eq. 1.3. For randomly inclined discs the relation between dn/dz and R^*_{gas} can be derived from Eq. A.2 following Wolfe et al. (1986)

$$\begin{aligned}\frac{dn}{dz} &= (1+z)^3 \frac{dr_{prop}}{dz} \int_0^\infty dL \Phi(L) A(L) \\ &= \frac{\pi}{2}\frac{c}{H}\Gamma(1+2t+\alpha)\phi^* R^{*2}_{gas} \times \\ &\quad \frac{(1+z)^2}{\sqrt{(1+z)^2(\Omega_0 z+1)-\Omega_\Lambda z(z+2)}},\end{aligned}$$

where Γ is the gamma function. Hence, R^* is given by

$$R^* = \sqrt{\frac{dn}{dz}\frac{2H\ \sqrt{(1+z)^2(\Omega_0 z+1)-\Omega_\Lambda z(z+2)}}{\pi c \Gamma(1+2t+\alpha)\phi^*(1+z)^2}}. \tag{1.8}$$

For an infinitely thin disc of radius R and with inclination θ ($\theta = 0$ for an edge-on disc) the average impact parameter $b(\theta)$ can be calculated as the mean radius of an ellipse with major axis R and minor axis $\sin(\theta)R$. For randomly inclined discs of radius R the average impact parameter $\bar{b}$ is then the average value of $b(\theta)$ weighted with $\sin(\theta)$ from the area and $\cos(\theta)$ from the random inclination, i.e.

$$\begin{aligned}\bar{b} &= 2R\int_0^{\pi/2} d\theta \sin(\theta)\cos(\theta) b(\theta) \\ &= 2R\int_0^{\pi/2} d\theta \sin(\theta)\cos(\theta)\left(4\int_0^1 dx \int_0^{\sin(\theta)\sqrt{1-x^2}} dy \frac{\sqrt{x^2+y^2}}{\pi\sin(\theta)}\right) \\ &= 0.566R\end{aligned} \tag{1.9}$$

(In Section 4.4.2 of Chapter 4 we use the slightly lower conversion $\bar{b} = 0.524R$ since we only use as weight $\cos(\theta)$).

If we assume that the gas is distributed spherically symmetric instead of in a thin disk, R^* would decrease by a factor of $\sqrt{2}$ and the relation between the average impact parameter $\bar{b}$ and R would be $\bar{b} = \frac{2}{3}R$.

Together with the Holmberg relation Eq. 1.8 and Eq. 1.9 provide the expected average impact parameter as a function of apparent magnitude, at $z = 3$, and the expected apparent magnitude distribution of a sample of DLAs selected by gas cross section. Using the updated LF these results are plotted in Fig. 1.6, for different values of the parameter t. As seen by comparing the two parts of Fig.1.6, changing the cosmology from ($\Omega = 1, \Omega_\Lambda = 0$) to ($\Omega = 0.3, \Omega_\Lambda = 0.7$) is only causing a stretching of the abscissa. This is because of the cancellation of *i)* the increased volume, which will decrease the space density of LBGs, and *ii)* the increased length of the line of sight per unit redshift, which means that objects with smaller space density can produce the observed $\frac{dn}{dz}$.

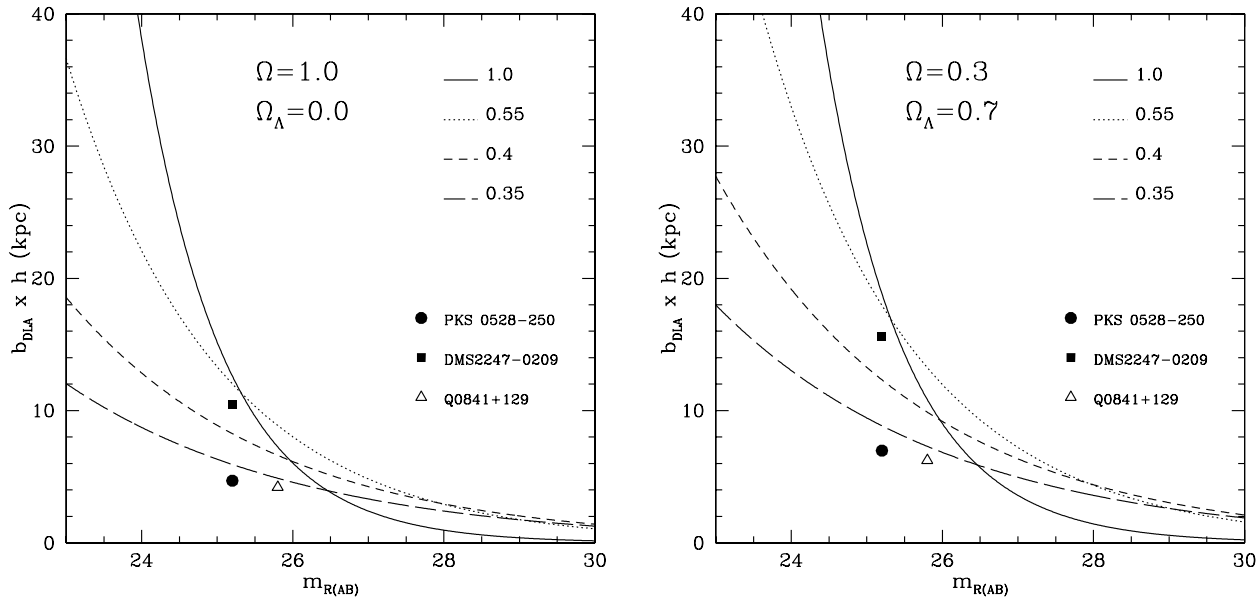

Figure 1.6: Predicted properties of the DLA population at $z = 3$ if DLAs are gaseous disks surrounding Lyman-break galaxies. The curves show predicted values of the mean impact parameter from the LBG to the line of sight to the quasar for different values of the Holmberg parameter t, as a function of apparent magnitude. The points are measured impact parameters for the two known DLA galaxies (and one likely candidate) for which the continuum magnitude of the galaxy has been measured. The left plot is for $\Omega = 1$ and Ω_Λ=0, and the right plot is for $\Omega = 0.3$ and Ω_Λ=0.7.

In Fig.1.7 is plotted the cumulative distribution for the observed R band magnitude for a sample of galaxies selected by gas cross-section. By comparing Fig.1.7 with the two parts of Fig. 1.6 we can estimate which value of the parameter t is most compatible with the data. For nearby spirals a value of $t \sim 0.4$–0.6 is measured (Wolfe et al., 1986). Chen et al. (1999) find a Holmberg type correlation between the gaseous extent of galaxies and B band luminosity with $t = 0.40 \pm 0.09$, however, they probe the gas at much lower column density. As seen, $t \sim 0.35$–0.45 is compatible with the few detected galaxy counterparts of DLAs, however, more observed galaxy counterparts of DLAs are needed to constrain t. For $t = 0.4$ we derive $R^* = 19.0h^{-1}$ kpc and $R^* = 26.9h^{-1}$ kpc for $\Omega = 1, \Omega_\Lambda = 0$ and $\Omega = 0.3, \Omega_\Lambda = 0.7$ respectively. These values are quite similar to the value $R^* = 35$ kpc used by Wolfe et al. (1986) for nearby spirals.

To illustrate the picture put forward here we have selected galaxies with photometric redshifts between 2.8 and 3.2 in a sub-image of size 1×1 arcmin^2 in the HDF North from the catalog of Fernández-Soto et al. (1999). These galaxies have R band magnitudes in the range 23.6< R <27.0 and all have colours in accordance with the LBG colour selection

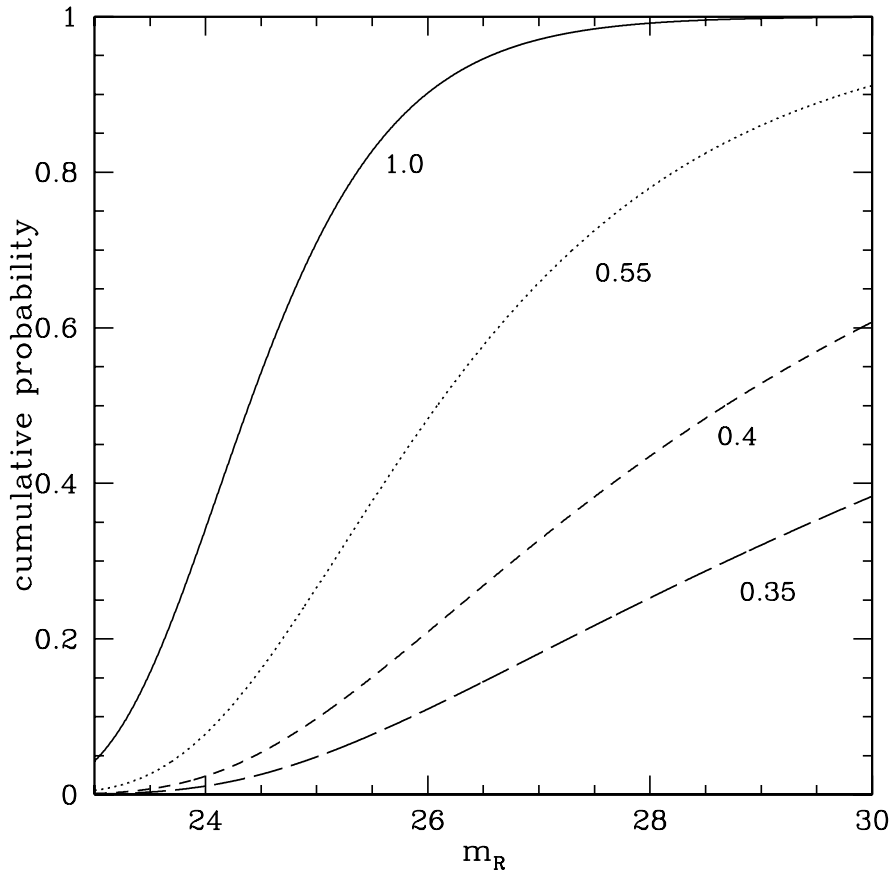

Figure 1.7: The predicted cumulative distribution of apparent magnitudes of DLA galaxy counter parts if DLAs are the gaseous halos of LBGs.

criteria in Dickinson (1999). For each LBG we have then assigned a HI radius according to the prescription given above, and over-plotted a randomly inclined disk with the given radius. Fig. 1.8 shows the result of this exercise. The dashed circle in Fig. 1.8 shows the estimated total absorbing area of galaxies with magnitudes $27 < R < 30$, i.e. galaxies that are too faint to be included in the LBG samples. The inserted star has a R band magnitude of about 19, which is at the faint end of the QSO luminosity function at $z = 3$. This illustrates the difficulties in identifying DLA galaxy counterparts.

If indeed DLAs have HI radii given by the Holmberg relation $R_{gas}/R^*_{gas} = (L/L^*)^t$ and if $t = 0.35$–0.45 then 50-80% of the DLAs at $z = 3$ must be fainter than $R = 27$. If true, the bulk of DLA galaxy counterparts have brightnesses similar to present day dwarf galaxies. A similar scenario is suggested by Lu et al. (1996) based on the metallicities of DLAs around z=3, which is very similar to that of stars in dwarf galaxies with ages corresponding to

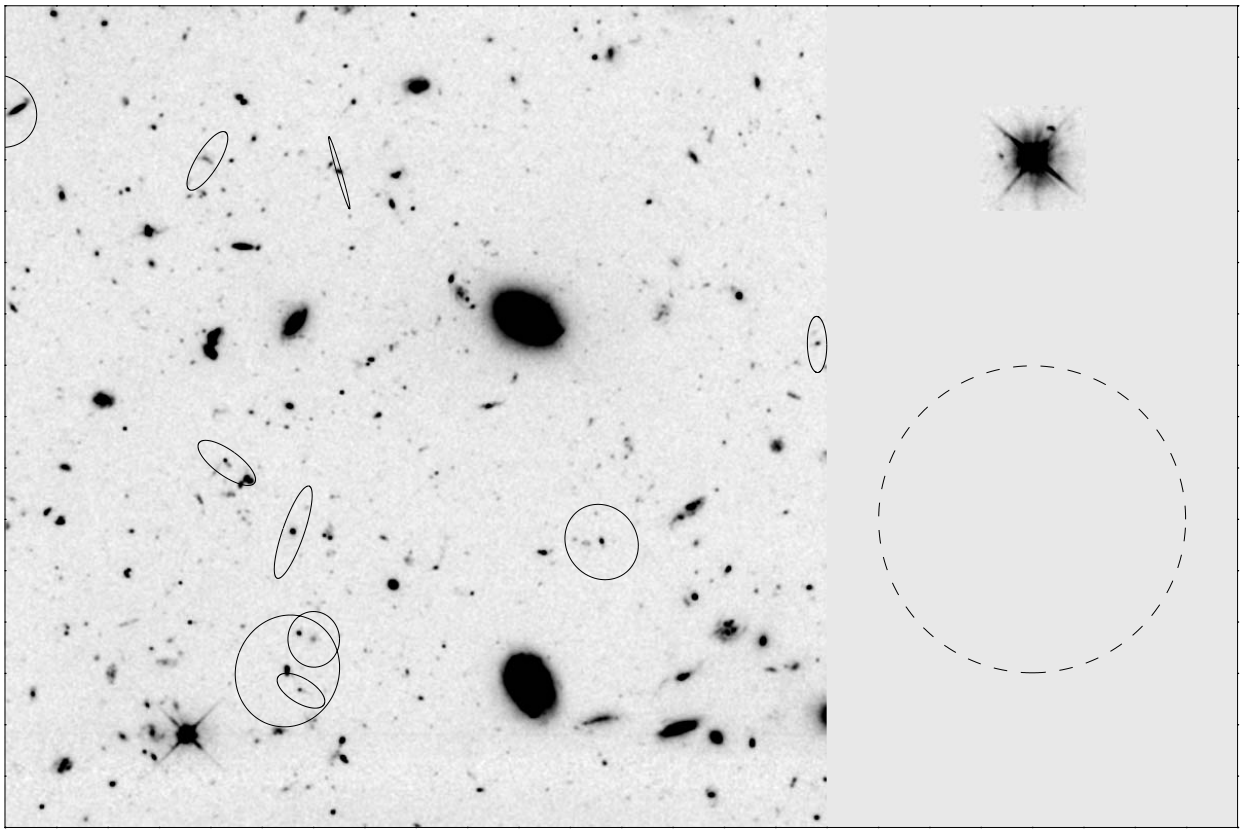

Figure 1.8: A 1×1 arcmin^2 subfield from the HDF North R band image. We have selected LBGs with redshift between 2.8 and 3.2 from the catalog of photometric redshifts of Fernández-Soto et al. (1999). Over-plotted on each LBGs is the extend of a randomly inclined HI disk with a radius given in the text. The dashed circle shows the estimated total absorbing area of galaxies with magnitudes $27 < R < 30$, and the insert in the upper right corner shows a point source with R band magnitude about 19.

formation redshifts near 3.

In terms of the measured light, which to first order must be proportional to the star formation, there are quite similar contributions from galaxies with R <25.5, 25.5< R <27.0 and R >27 (30%, 26% and 46% respectively). Hence, if the luminosity function derived by Steidel et al. (1998) is correct, only about a third of the total star formation at z=3 is traced by the LBGs studied in the ground based samples. On the other hand, for $t = 0.40$, the contributions to the total DLA cross-section of galaxies from the same three magnitude bins are 17%(R <25.5), 19%(25.5< R <27.0) and 64% (R >27).

To study DLA galaxy counterparts with broad band imaging we have to be able to detect a $R = 27$–30 galaxy 0–3 arcsec from a QSO that typically has an apparent R band magnitude of 17–19. This is an extremely difficult task.

1.5 Clustering of Galaxies

I end this introduction by briefly outlining the background for Chapter 9. By studying the clustering of galaxies it is possible to draw conclusions about structure formation on scales 1–100h^{-1} Mpc, which cannot be probed by individual galaxies (see e.g. Fall 1979 and Guzzo 1999 for reviews on large scale structure).

For very faint galaxies it is unfeasible to conduct redshift surveys. Hence it is not possible to measure their spatial correlation function. One can however, still obtain useful information by measuring the angular two point correlation function $w(\theta)$, which is defined as the over-probability to find two galaxies at a separation θ compared to a random Poissonian distribution :

$$dP(\theta) = (1 + w(\theta))\frac{d\Omega_1 d\Omega_2}{(4\pi)^2}. \tag{1.10}$$

A model prediction for the amplitude of the angular two-point correlation function $w(\theta)$ for a galaxy catalog with a given limiting magnitude can be calculated with the following inputs :

- **The spatial galaxy two-point correlation function $\xi(r)$**

  At low redshift $\xi(r)$ is measured to have the form

  $$\xi(r) = (\frac{r}{r_0})^{\gamma}, \tag{1.11}$$

  where r is the proper length, r_0 is about 4–5Mpc, and $\gamma = 1.8$.

- **The evolution of ξ with redshift**

  Evolution of $\xi(r)$ is normally parameterized by the term ϵ as :

  $$\xi(r, z) = \xi(r, z = 0)(1 + z)^{-(3+\epsilon)}. \tag{1.12}$$

  No evolution in proper space corresponds to $\epsilon = 0$. No evolution in comoving space corresponds to $\epsilon = \gamma - 3 = -1.2$. If $\epsilon > 0$, clustering evolves with time in proper coordinates, with $\epsilon = 0.8$ corresponding to linear evolution and $\epsilon > 0.8$ corresponding to nonlinear evolution (see e.g. Woods and Fahlman 1997).

- **The redshift distribution of the galaxy catalog**

  Since the angular correlation function is effectively the the spatial correlation function averaged over all redshifts and over different scales (dependent on redshift) one also has to assume a redshift distribution for the galaxies in the catalog.

Different authors assume different shapes of this redshift distribution. Villumsen et al. (1996) assume a redshift distribution of the form :

$$N(z) = \frac{\beta z^2}{z_0^3 \Gamma[3/\beta]} \exp(-(\frac{z}{z_0})^\beta), \tag{1.13}$$

where $\beta = 2.5$. z_0 is then specified for each magnitude bin. Brainerd and Smail (1998) use the same formula but with $\beta = 2$.

When $N(z), r_0, \gamma$, ϵ and the cosmology are specified, $w(\theta)$ can be determined and compared to measurements by the integral (Limber 1954) :

$$w(\theta) = C r_0^\gamma \theta^{1-\gamma} \int_0^\infty dz D_A(z)^{1-\gamma} H(z)(1+z)^{-(3+\epsilon)} N(z)^2, \tag{1.14}$$

where $D_A(z)$ is the angular diameter distance (see Appendix A), and $H(z)$ is given by :

$$H(z) = \frac{H_0}{c}(1+z)\sqrt{(1+z)^2(\Omega z + 1) - \Omega_\Lambda z(z+2)}. \tag{1.15}$$

The angular correlation function has been measured in various broad band filters to larger and larger depth during the last decade. In Chapter 9 a measurement of $w(\theta)$ in the Hubble Deep Field North and South fields is presented. These fields constitute the deepest optical images ever obtained and hence allow a measurement $w(\theta)$ at extremely faint magnitudes $m \approx 28$–29.

Chapter 2

Methods

In this chapter I describe the most important methods and concepts related to the observations, reductions and analysis behind the work presented in this thesis.

2.1 Observations

Here I will briefly outline some essential aspects of the data collection process, which for the material presented in this thesis is predominately through optical imaging using Charged Coupled Devices (CCDs). I will focus on what can be achieved with present day instrumentation rather than trying to outline in detail all steps along the way from collecting CCD exposures at the telescope to the calculation of absolute fluxes of objects.

The complicated process of taking an exposure (an array of counts $Counts(x, y)$ at pixel positions x, y) may be expressed mathematically as :

$$\begin{aligned} Counts(x,y) &= GAIN \int_{t_1}^{t_2} dt \int_{\lambda} d\lambda \frac{F_\lambda(\theta,\phi,t)}{hc/\lambda} \otimes (PSF(x,y,t,\lambda)\epsilon(x,y,t,\lambda)) \\ &\quad + BIAS(x,y) + RON(x,y), \end{aligned} \tag{2.1}$$

where $F_\lambda(\theta, \phi, t)$ is the so called monochromatic flux from a point on the celestial sphere with declination θ and right-ascension ϕ, corresponding to pixel coordinates x and y, at time t. $PSF(x, y, t, \lambda)$ is the Point Spread Function by which $F_\lambda(\theta, \phi, t)$ is folded, and $\epsilon(x, y, t, \lambda)$ is the fraction of photons with wavelength λ above the atmosphere detected at the pixel with coordinates x and y. The $GAIN$, the Read Out Noise (RON) and the $BIAS$ are multiplied/added/added to the counts during readout of the CCD. The efficiency factor $\epsilon(x, y, t, \lambda)$ is a product of several contributions :

$$\epsilon = \epsilon_{atmosphere} \times \epsilon_{mirrors} \times \epsilon_{instrument} \times \epsilon_{filter} \times \epsilon_{CCD}, \tag{2.2}$$

i.e. with photons being lost in the atmosphere (due to scattering and absorption), at the telescope mirrors (due to absorption and transmission), at the mirrors and lenses within

Table 2.1: Johnson UVBRI filter characteristics (from Landolt-Börnstein 1982)

Filter	F_0 [a]	$\lambda_{central}$	$\Delta\lambda$
	erg cm^{-2} s^{-1} Å^{-1}	Å	Å
U	4.22×10^{-9}	3600	400
B	6.40×10^{-9}	4400	1000
V	3.75×10^{-9}	5500	800
R	1.75×10^{-9}	7100	2100
I	0.84×10^{-9}	9700	2200

[a] the monochromatic flux F_λ above the atmosphere for an object with magnitude 0.

the instrument, at the filter and at the detection process in the CCD. The typical total efficiencies one can reach in imaging from the ground is approximately 3–5% in the U–band and 20–30% from the B–band through to the I–band (see Table 2.1 for the characteristics of broad band filters in the Johnson system). The largest contribution to ϵ in the near ultraviolet is from the atmosphere, the low filter transmissions and the typically low CCD efficiencies below 4000Å.

2.1.1 Detection limits

The signal-to-noise (SN) resulting from an exposure of duration t, a total efficiency ϵ, a telescope collecting area of A for a source with magnitude m in a given broad band filter and extension $d\Omega$ (in units of arcsec^2) on the sky is given by :

$$SN \approx \frac{\frac{F_0\times\lambda_{central}\Delta\lambda}{hc}\times 10^{-0.4m}\times\epsilon\times A\times t}{\sqrt{\frac{F_0\times\lambda_{central}\Delta\lambda}{hc}\times(10^{-0.4m}+d\Omega 10^{-0.4m_{sky}})\times\epsilon\times A\times t+d\Omega/p^2*RON^2}}, \quad (2.3)$$

where p is the pixel scale (i.e. the number of arcsec on the sky per pixel), f_0 is the zero-point monochromatic flux for the filter as given in the first column in Table 2.1, and m_{sky} is the magnitude per arcsec^2 of the sky in the given filter. F_0, $\lambda_{central}$ and $\Delta\lambda$ are given in Table 2.1. This is illustrated by two examples : For a point source $d\Omega$ is determined by the Full-Width-at-Half-Maximum (FWHM) of the PSF, which is also called the *seeing*. About 95% of the energy is contained within the area $d\Omega = \pi \times seeing^2$. The High Resolution Adaptive Camera (HiRAC) on the 2.56m Nordic Optical telescope (NOT) has a pixel scale of 0.1082 arcsec per pixel and an efficiency about 20% in the B–band. The sky brightness during dark time is about 22.3 mag arcsec^{-2}. For point sources a 1 hour exposure on the Nordic Optical Telescope in the B–band with seeing 0.8 arcsec reach a 5σ limiting magnitude of B≈=26. For FORS1 on the 8.2m Very Large Telescope (VLT) with a pixel scale of 0.200

arcsec per pixel in the standard resolution mode, a sky background in the B during dark time about 22.7 mag arcsec^{-2} gives approximately B=27.5.

For narrow–band imaging in a filter with width $\Delta\lambda$ the signal-to-noise ratio per arcsec^2 for an emission line with total surface brightness F (erg cm^{-2} s^{-1} arcsec^{-2}) within the filter is :

$$SN \approx \frac{\frac{F\times\lambda_{central}}{hc} \times \epsilon \times A \times t \times d\Omega}{\sqrt{(\frac{F\times\lambda_{central}}{hc} + \frac{F_\lambda^{sky}\times\Delta\lambda\lambda_{central}}{hc})d\Omega \times \epsilon \times A \times t + d\Omega/p^2 * RON^2}}, \tag{2.4}$$

where F_λ^{sky} in this case is the specific intensity (units erg cm^{-2} s^{-1} Å^{-1} arcsec^{-2}) of the background in the filter. A rough estimate of F_λ^{sky} is $F_0 \times 10^{-0.4m_{sky}}$, i.e. assuming that the specific intensity can be calculated from the broad band sky background m_{sky}. Consider as an example a 20Å (fwhm) narrow filter centred at 3550Å. With HiRAC on the NOT, assuming a total efficiency of 5% and a pixel scale of 0.1082 arcsec/pixel leads to a 5σ detection limit of about 1.5×10^{-16} erg cm^{-2} s^{-1} Å^{-1} arcsec^{-2} in a 4000sec exposure. In this case, more than 90% of the variance comes from read-out noise. Binning the detector 3 times in both directions leads to a 5σ limit of 7×10^{-17} erg cm^{-2} s^{-1} Å^{-1} arcsec^{-2} and a contribution of 45% from read-out-noise to the total variance. This illustrates the importance of binning the CCD when observing in the U–band. For FORS1 with 0.200 arcsec per pixel and assuming a 5% efficiency, the corresponding 5σ limit is 4×10^{-17} erg cm^{-2} s^{-1} Å^{-1} arcsec^{-2}.

2.2 Reduction

2.2.1 Basic Reductions

The basic reduction of the frames produced at the telescope involves *bias subtraction* and *flat-fielding*. For a thorough explanation of the purpose, strategy and important issues of these basic reductions see Gilliland (1992).

2.2.2 Image combination

Following the basic reductions we need to combine the individual frames into one combined frame. The goal of image combination is in an optimal way to combine n reduced images with slight offsets, different seeings, different sky background levels and with different flux-levels (due to varying airmass or perhaps un-photometric observing conditions) and with cosmic ray hits into one image. The first step in this process is to subtract the sky from all n images and to scale the images, so that objects with constant flux have the same flux in all frames, and to transform the n frames to a common coordinate system. We then need to find an optimal way to combine the n values for a given pixel into a final combined value. The combination should maximize the final signal-to-noise (SN) ratio for objects for which

the noise is dominated by background shot-noise. For such objects the variance in frame j is given by $Var_j = sky_j + RON^2$, where RON is the readout noise and sky_j is the sky-level in frame j. The optimal weight is then $W_j = (sky_j + RON^2) \times scale_j^2$, where $scale_j^2$ is the scaling used to bring $frame_j$ onto the common flux scale.

The combination of the counts measured in the n pixels belonging to n individual frames is illustrated in a flow diagram in Fig. 2.1. We first reject pixels in bad columns, hot pixels and other pixels for which we have an *a priori* knowledge that they do not contain useful information. We then wish to calculate the optimally weighted average of the remaining $N = n - n_{bad}$ pixels. In this average we might have to reject more pixels, e.g. pixels affected by cosmic ray hits, hence we need an objective strategy for the rejection of pixels that are not to be included in the weighted average. The strategy we use is a variant of what is generally refered to as "σ-clipping". Since we combine images with different seeing, and since we only transform individual frames to a common frame of reference with integral pixel shifts, strong sources will cause large deviations at a given pixel. In an attempt to prevent the rejection of these pixels, we use the following scheme : we define a function $\chi_{lim}(\overline{s})$ that gives the acceptable χ for a pixel with expected signal $\overline{s}$ after sky subtraction. $\chi_{lim}(\overline{s})$ is given by a σ cut level χ_0, a rejection ceiling C, and a rejection ceiling scaling α in the following way

$$\chi_{lim}(\overline{s}) = \begin{cases} \chi_0 & \text{if } \overline{s} < C\sigma_{sky} \\ \alpha \frac{\overline{s}}{\sigma_{sky}} + \beta & \text{if } \overline{s} > C\sigma_{sky} \end{cases} , \tag{2.5}$$

where β can be calculated from the condition that $\chi_{lim}(\overline{s})$ should be continuous in $\overline{s}$: $\beta = \chi_0 - \alpha C$. The values of χ_0, C, and α have to be optimized for each set of images to be combined from the criteria that *i)* there should not be an overdensity of rejections around bright objects (this determines α), *ii)* cosmic ray hits should be rejected (this determines χ_0 and C). Typical values are χ_0=4.5, C=1, and α=0.4–1.

2.3 Analysis

2.3.1 PSF subtraction

After the image combination an important part of the analysis of much of the work presented in this thesis is modeling and subtraction of the Point Spread Function (PSF) of the point source emission from QSOs. The Point Spread Function is the distribution of light on the detector from a point source outside the atmosphere of the earth. The Full Width at Half Maximum (FWHM) of this distribution (also refered to as the seeing) is determined by *i)* the diffraction due to the finite size of the primary mirror, and *ii)* the turbulence in the atmosphere along the light-path. The seeing at the best sites are a few tenths of an arcsec, but under poor seeing conditions it may be several arcsec. Since the radii of stars ($\sim 10^9$–10^{11}m) are much smaller than their distances ($> 10^{16}$m), their angular extent on the sky

are normally so small (much smaller than the seeing) that they may be considered to be point sources (note, however, that a red giant with a distance of about 1 pc would have an angular extent of ≈ 1 arcsec). The extent of the broad line region in QSOs, where most of the emission originates, is of the order 100 light-days (10^{15}m), whereas their distances are several hundred Mpc, so it is clearly justified to consider them point sources (hence their names). Accordingly, we may model the light distribution from a QSO in a given combined frame with the light distribution determined from stars in the field.

The determination of a good PSF-model can be delicate. In principle, the PSF may depend on the position on the detector, the colour of the object and maybe even on the brightness of the object if the detector is non-linear. An important first step in any PSF-subtraction is hence to examine the variation of the PSF across the field. However, this requires that there are several point sources across the field, which is not always the case. For the two detectors we have used for this work, namely the HiRAC (High Resolution Adaptive optics Camera) instrument on the Nordic Optical Telescope (NOT) and the EMMI (ESO Multi Mode Instrument) instrument on the ESO New Technology Telescope (NTT), our experience is that the PSF is very stable across the field with HiRAC, whereas it does depend slightly on the field for frames obtained with EMMI.

In the work presented in this thesis we always used the software package DAOPHOT-II (Stetson 1997) to model the PSF. The PSF in DAOPHOT-II is represented by the sum of an analytical function fitted within a preselected fitting radius plus an interpolated value derived from a table of residuals covering an area out to a preselected PSF radius. The analytical function is fitted to the rapidly varying central core of the PSF, whereas the PSF radius is chosen such as to include any scattered light component in the halo part of the stellar images. We use a function for the fit consisting of a Gaussian core plus a Lorentzian wing, where the Lorentzian and Gaussian may be tilted in different directions (this function is called 'PENNY2' in DAOPHOT-II).

2.3.2 The "narrow minus on–band–broad" versus "narrow minus off–band–broad" colour/colour plot technique

For a systematic identification of objects with Lyα emission lines we use a colour/colour plot technique where we plot a narrow minus on–band–broad colour against a narrow minus off–band–broad colour. Here I describe in detail how we compare the measured distribution of galaxy colours in this diagram with colours of model galaxy spectra. In all the work presented in this thesis we calculate magnitudes on the so called AB-magnitude system defined by (e.g. Oke 1990) :

$$AB = -0.4 \log(\bar{f}_\nu) - 48.60, \tag{2.6}$$

Table 2.2: The range of ages of starburst models from the Bruzual & Charlot 95 spectral synthesis models, and the range of redshifts for each group of models. The resulting colour-colour plot calculated from Eq. 2.7 is seen as Fig. 2.3a.

Ages Gyr	redshifts	symbol
6–17	0–0.5	□
0.6–5	0–1.5	△
0.02–0.6	1.5–3.5	◊

where $\bar{f}_\nu$ is the specific intensity of the sources averaged over the transmission curve of the filter. Hence, it is straight forward to calculate the colours in the AB-system of model galaxy spectra. We have used the 1995 version of Bruzual and Charlot's spectral synthesis models. These models provide the spectral energy distribution of galaxies of different ages and with different star formation histories in units of $L_\odot$ Å^{-1} (proportional to f_λ). We can then calculate the $(m1 - m2)_{AB}$ colour in two filters $m1$ and $m2$ with filter transmission curves $T_1(\lambda)$ and $T_2(\lambda)$ for a model galaxy with spectral energy distribution f_λ^{model} at redshift z as

$$\begin{aligned}(m1 - m2)_{AB} &= -0.4 \log \left(\frac{\bar{f}^{model}_{\nu(1+z),1}}{\bar{f}^{model}_{\nu(1+z),2}} \right) \\ &= -0.4 \log \left(\frac{\int d\lambda T_1(\lambda) f_\lambda^{model}(\frac{\lambda}{1+z})\lambda^2 / \int d\lambda T_1(\lambda)}{\int d\lambda T_2(\lambda) f_\lambda^{model}(\frac{\lambda}{1+z})\lambda^2 / \int d\lambda T_2(\lambda)} \right) . \end{aligned} \tag{2.7}$$

As an example we will show the range of colours expected for galaxies without emission lines in the field of the redshift $z = 3.036$ QSO Q1205-30 (Chapter 7). We imaged this field in the broad band filter B and I and in a 20Å narrow filter centred at 4906Å. The filter transmission curves are shown in Fig. 2.2. As seen in Fig. 2.2, the narrow filter is centred in the red wing of the transmission curve of the broad band B-filter, so in this case the B-filter is not exactly on band relative to the narrow filter. Hence, objects with a red spectral energy distribution will appear to have excess emission in the narrow filter compared to broad band B, i.e. have a negative "narrow minus on–band–broad" colour. To simulate the strength of this effect we calculate the colours of spectral synthesis models following Eq. 2.7 for the range of models listed in Table 2.2.

Fig. 2.3 compares the predicted range of colours of galaxies with the observed distribution of galaxy colours from the work presented in Chapter 7. As seen there is good agreement.

→ **1.** Input n pixels with counts s_j and variance $Var_j = scale_j^2 \times (s_j + sky_j + RON^2)$.

→ **2.** Reject bad pixels with $s_j > badsig$. Use the remaining $N = n - n_{bad}$ pixels in the following.

→ **3.** Use as weight
$W_j = scale_j^2 \times (sky_j + RON^2)$.
Calculate weighted mean and χ.
$\overline{s} = (\sum_{j=1}^{N} \frac{s_j}{W_j}) / \sum \frac{1}{W_j}$
$\chi = \sqrt{\sum_{j=1}^{N} \frac{(s_j - \overline{s})^2}{Var_j} / (N-1)}$

→ **4.** If $\chi > \chi_{lim}(\overline{s})$: Goto 5
If $\chi < \chi_{lim}(\overline{s})$: Goto 6

→ 5. Reject the highest and lowest s_j, one by one, and calculate χ of the remaining pixels. Choose the set of pixels with the smallest χ. Goto 4.

→ 6. $\overline{s}$ is now a good guess for the "true" value of the flux in the given pixel. Now perform σ-clipping : Run through the list of pixels from 2. and reject pixels with $\sqrt{\frac{(s_j - \overline{s})^2}{Var_j}} > \chi_{lim}(\overline{s})$.

→ 7. Calculate the weighted mean and variance of the remaining $N_{final} = n - n_{bad} - n_{rej}$ pixels. This is the final value for the flux in the pixel and its variance.
$\overline{s}_{final} = (\sum_{j=1}^{N_{final}} \frac{s_j}{W_j}) / \sum \frac{1}{W_j}$
$Var_{final} = (\sum_{j=1}^{N_{final}} \frac{Var_j}{W_j^2}) / (\sum \frac{1}{W_j})^2$

Figure 2.1: A flow diagram describing the σ-clipping used to combine images.

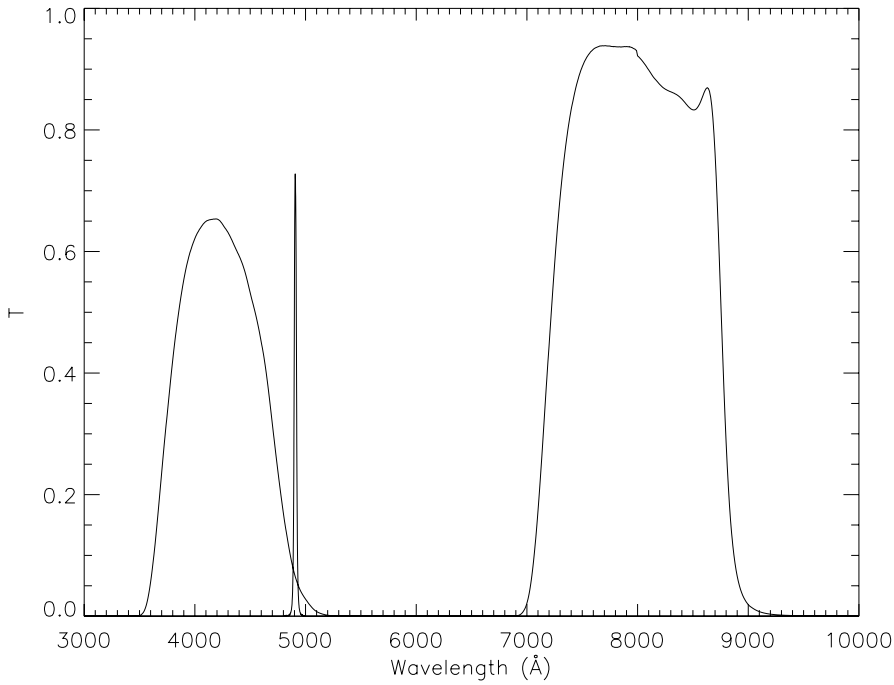

Figure 2.2: Transmission curves for (from left to right) the broad band B filter, the 20Å narrow filter and the broad band I filter.

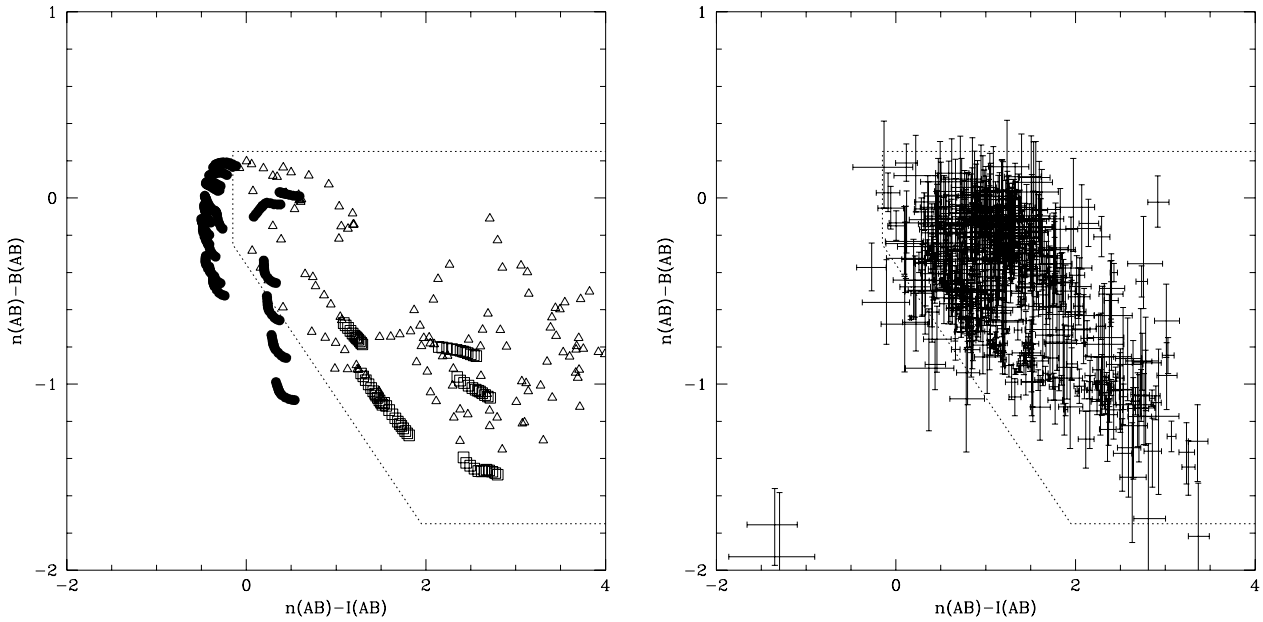

Figure 2.3: *Left plot :* The $n(AB) - B(AB)$ vs. $n(AB) - I(AB)$ colour-colour plot for the range of models and redshifts listed in Table 2.2. *Right plot :* The $n(AB) - B(AB)$ vs. $n(AB) - I(AB)$ colour-colour plot for objects in the field of Q1205-30.

Chapter 3

On the nature of $z_{\rm abs} \approx z_{\rm em}$ damped absorbers in quasar spectra

Møller P., Warren S.J., Fynbo J.U., 1998, A&A, **330**, 19

3.1 Introduction

Two optical strategies have been employed to search for high–redshift normal galaxies. Using narrow–band imaging to detect Lyα , relatively few have been discovered (e.g. Lowenthal et al.1991, Møller & Warren 1993a (hereafter Paper I), Francis et al.1996). However, recently Steidel and collaborators have had considerable success with broad-band imaging, identifying candidates by the expected Lyman break in their spectra (Steidel et al., 1996b). The same strategy applied to the Hubble Deep Field data has provided a measurement of the global star formation rate in galaxies in the redshift interval $2 < z < 4$ (Madau et al. 1996).

The searches for starlight from high–redshift galaxies are complemented by the analysis of the damped Lyα (DLA) absorption lines in the spectra of high–redshift quasars. The DLA studies have yielded measurements of the mass density of neutral hydrogen in the universe (e.g. Wolfe 1986; Lanzetta et al.1991), and the abundance of heavy elements in the gas (e.g. Pettini et al.1994; Lu et al., 1996), and how these quantities have changed with redshift. The relation between the DLA absorbers and the Lyman-break galaxies is not yet well established, but is important, as it will connect the measured global rate of star formation with the evolution of the global density of neutral gas, and its chemical enrichment. This will allow a more detailed comparison with theories of how galaxies are assembled. For this reason considerable effort has been devoted to the detection of DLA absorbers in emission, in order to measure the star formation rate for the absorber, and the sizes of the cloud of neutral gas, and of the region of star formation.

Unfortunately to date only two DLA absorbers have been successfully, and unambiguously, identified. These are i.) the system at $z = 2.81$, of column density $\log(\mathrm{N_{HI}}) = 21.35$, seen in the spectrum of the quasar PKS0528-250 (Paper I), and ii.) the system at $z = 3.15$, of column density $\log(\mathrm{N_{HI}}) = 20.00$, seen in the spectrum of the quasar Q2233+131 (Djorgovski et al. 1996). In the latter case the column density is below the value usually recognised as defining a DLA system, but we will treat it as a DLA absorber here. The PKS0528-250 $z = 2.81$ DLA absorber has been the subject of extensive imaging and spectroscopic observations by ourselves. These have yielded clues to the connection between DLA absorbers and the Lyman break galaxies, described below. The absorber is nevertheless unusual as the redshift is similar to the redshift of the quasar. There are only a few such $z_{\rm abs} \approx z_{\rm em}$ DLA absorbers known.[1]

The detection of Lyα emission from the PKS0528-250 $z = 2.81$ DLA absorber, as well as from two companions with similar redshifts, was reported in Paper I. The DLA absorber (as well as the companions) has subsequently been detected in the continuum, with the Hubble Space Telescope (HST), confirming that the Lyα emission is due to star formation

[1] In this paper we refer to absorbers with redshifts within a few thousand km s^{-1} of the quasar emission redshift as $z_{\rm abs} \approx z_{\rm em}$ absorbers, and to absorbers at lower redshift as intervening absorbers.

rather than photoionisation by the quasar (Møller & Warren 1996). The measured half light radius of the continuum emission, $r_{0.5} = 0.13''$, and the apparent magnitude, $m_B = 25.5$, are within the range measured for Lyman-break galaxies, which led us to suggest that the two are essentially the same population (Møller & Warren 1998, hereafter Paper III). The two companions in this field are similarly small in size. These HST observations support our earlier suggestion (Warren & Møller 1996, hereafter Paper II), based on dynamical evidence, that these three objects are sub-units of a galaxy in the process of assembly.

Pettini et al. (1995) have detected a similar slightly-offset emission line in the trough of a second $z_{\rm abs} \approx z_{\rm em}$ damped absorber at $z = 3.083$, towards the quasar 2059-360. Lyα emission may therefore be more common in or near DLA absorbers near quasars than in or near intervening DLA absorbers. Because of the unusual nature of the PKS0528-250 absorber, and to investigate the possibility that Lyα emission in DLA absorbers is in some way enhanced in $z_{\rm abs} \approx z_{\rm em}$ systems, over intervening systems, we have obtained spectra of a third $z_{\rm abs} \approx z_{\rm em}$ DLA absorber, the system at $z = 1.93$ seen in the spectrum of the quasar Q0151+048A. This absorber was first studied by Williams & Weymann (1976). The quasar (=UM144=PHL1222, 1950.0 coordinates RA 1 51 17.43, Dec 4 48 15.1) is radio quiet, optically is relatively bright ($m_V = 17.63$, $m_B = 18.03$), non variable, and has a faint ($m_V = 21.2$) companion quasar Q0151+048B lying 3.3$''$to the NE, and at a similar redshift, discovered by Meylan et al.(1990).

The spectroscopic observations are described in Sect. 3.2. In Sect. 3.3 we present the spectrum. By fitting a Voigt profile to the damped absorption line we find evidence for an emission line near the base of the trough, just blueward of the absorption line centre. In Sect. 3.4 we provide a discussion of the question of whether the $z_{\rm abs} \approx z_{\rm em}$ DLA absorbers are intrinsically different to the intervening DLA absorbers, and in Sect. 3.5 we list our conclusions.

3.2 Observations and data reduction

On the nights of 1994 August 3 and 4 we obtained two spectra of Q0151+048A, of combined integration time 6200 seconds, using the blue arm of the EMMI instrument on the ESO 3.5m NTT. We used grism # 3 (1200 grooves mm^{-1}, blazed at 3800Å) and a 1.5$''$ slit, yielding a resolution of 2.0Å. The detector was a Tektronix 1024 × 1024 CCD, binned by a factor two in the dispersion direction, giving a pixel size of 0.38$''$ × 0.90Å. The readout noise of the chip was $8e^-$. The journal of observations is provided in Table 3.1.

The spectra were reduced using standard techniques for bias and dark subtraction, and flatfielding. One dimensional spectra were extracted and combined using the optimising extraction routine described by Møller & Kjærgaard (1992). The final spectrum is shown in Fig. 3.1.

Table 3.1: Journal of observations

Date	Target	Exp. (sec)	Seeing ($''$)	PA (E of N)
3 Aug 94	Q0151+048A	2600	2.2	90°
4 Aug 94	Q0151+048A	3600	3.8	120°

3.3 Results

3.3.1 Absorption lines in the spectrum of Q0151+048A

The line search algorithm described in Møller et al.(1994) was used to find, measure, and identify absorption lines. In this case the continuum against which absorption lines were measured included the absorption of a damped Voigt profile near 3567Å, with parameters as described below. The resulting line list, excluding the DLA line, and complete to 4σ, is provided in Table 3.2. Listed there are the observed vacuum wavelength, the observed equivalent width $W_{\rm obs}$, and the 1σ error on the equivalent width $\sigma_{\rm W}$, for each line. The error on the wavelengths of the line centroids is dominated by the uncertainty associated with centring the quasar in the slit, and is estimated to be 0.4Å.

Sargent et al.(1988) have identified lines 14 and 15 as the CIV(1548, 1550) doublet at $z = 1.468$. With our identification the wavelength difference between the OI(1302) and SiII(1304) lines, at $z = 1.9342$, is 6.46Å, whereas with their identification the wavelength difference is only 0.11Å less. With these data it is not possible to distinguish between these two possibilities, but given the strength of the other SiII lines at $z = 1.9342$ we find the most natural identification is that given in Table 3.2.

The DLA line near 3567Å absorbs part of the quasar Lyα and NV emission lines, so to determine the best-fit parameters for the damped line it was necessary to allow for the fact that the unabsorbed spectrum (the "continuum") is not at all flat in the region of the DLA line. By dividing the spectrum by the Voigt profile for trial values of redshift and column density, a first solution for these parameters was found, which produced a realistic unabsorbed quasar emission line profile – disregarding the wavelength region over which the absorption line is saturated. A smooth continuum, including Lyα and NV emission lines, was fitted to this corrected spectrum, interpolating across the saturated region, 3560Å – 3573Å. For this continuum we now determined the Voigt profile which best fit the observed spectrum. Dividing again by the model, the procedure was iterated to a solution. The results of this process are illustrated in Fig. 3.2, which shows an expanded plot of the spectrum in the region of the damped line, together with the best fit to the absorption line.

While there is a certain amount of arbitrariness in the details of the final model for the

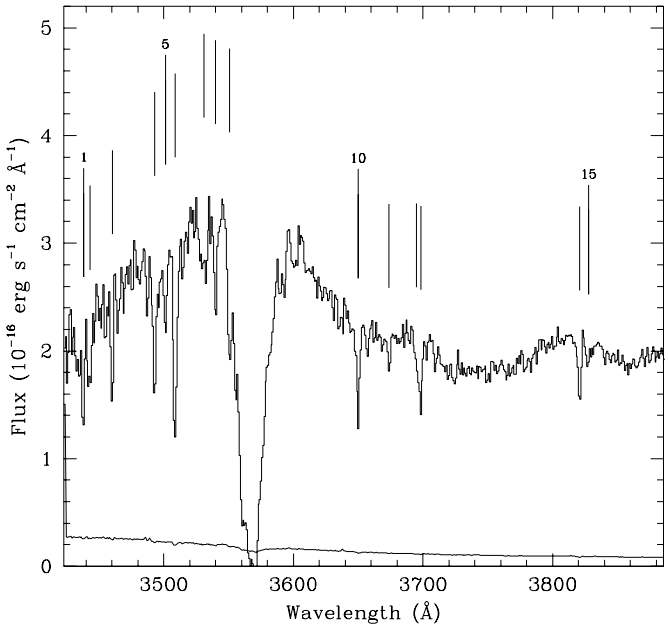

Figure 3.1: Combined spectrum of Q0151+048A in the region of the DLA absorption line. Flux per unit wavelength is plotted against wavelength. The lower solid line shows the 1σ noise spectrum. The spectrum has not been corrected for relative slit losses which were substantial (see text Sect. 3.3.2).

quasar emission lines, the same is not true for the DLA absorption line. The parameters of this line are strongly constrained by the saturated central part and by the steep sides. The best fit was obtained with N(HI) $= 2.3 \times 10^{20}$cm^{-2}, $z_{\rm abs} = 1.9342$, but acceptable fits could be obtained for column densities in the range $2 - 4 \times 10^{20}$cm^{-2}.

3.3.2 Emission from the DLA absorber

Inspection of Fig. 3.2 shows that the model provides a close match to the profile of the absorption trough, except in the bottom of the DLA line where there appears to be a weak narrow emission line at the blue edge of the saturated part of the profile. On the assumption that the model absorption profile is correct, as evinced by the excellent fit at all other wavelengths, this emission feature is significant at the 4.5σ level. Note that while it is possible to obtain other acceptable fits to the absorption trough by adjusting slightly the modelled Lyα and NV quasar emission lines, and making corresponding changes to the DLA parameters, this can never significantly change the saturated part of the absorption line profile, so the flux in this emission feature is quite insensitive to the details of the fitting. To illustrate the emission feature more clearly we have subtracted the model absorption profile from the data, and divided the difference by the 1σ error spectrum. The resulting residuals (smoothed for display purposes) are shown in Fig. 3.3.

Table 3.2: Absorption lines in Q0151+048A

No.	$\lambda_{\rm obs}$ (Å)	$W_{\rm obs}$ (Å)	$\sigma_{\rm W}$ (Å)	ID	$z_{\rm abs}$
1	3438.4	0.94	.18		
2	3443.1	0.98	.23		
3	3460.6	0.97	.15		
4	3493.0	1.24	.14	SiII (1190)	1.9343
5	3501.3	1.02	.18	SiII (1193)	1.9342
6	3509.0	2.24	.17		
7	3530.9	1.07	.17		
8	3539.8	0.84	.12		
9	3550.7	1.13	.13		
10	3649.8	1.15	.13	SiIV (1393)	1.6187
11	3673.9	0.34	.09	SiIV (1402)	1.6190
12	3695.1	0.57	.11		
13	3698.3	0.80	.09	SiII (1260)	1.9342
14	3820.8	0.76	.07	OI (1302)	1.9342
15	3827.4	0.52	.12	SiII (1304)	1.9343

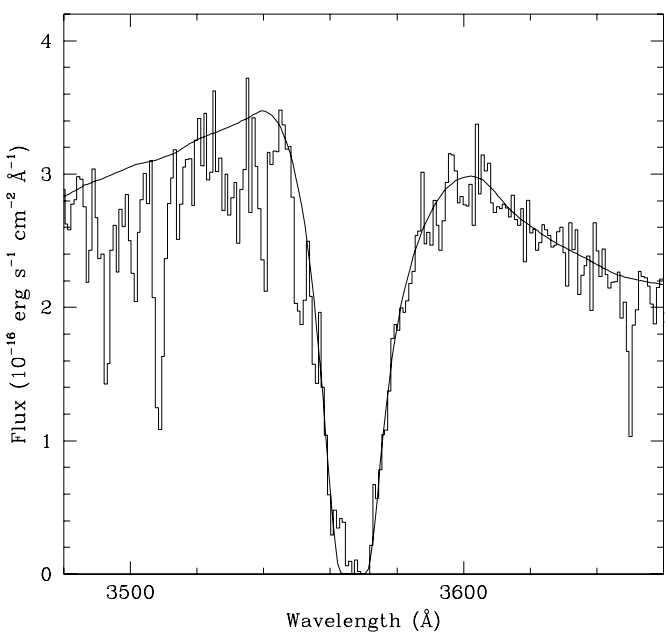

Figure 3.2: Observed spectrum of Q0151+048A. The smooth line shows the fit to the damped absorption line, for values of N(HI) = 2.3×10^{20}cm^{-2}, $z_{\rm abs} = 1.9342$. Note the residual in the blue side of the saturated part of the DLA line.

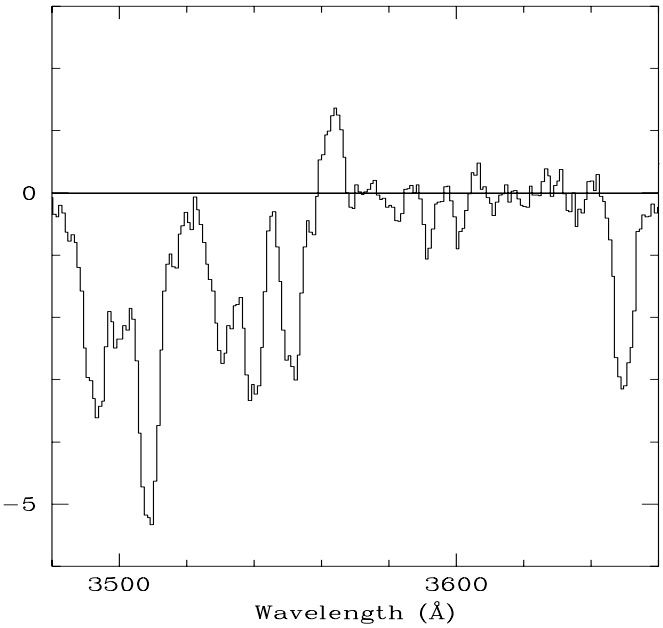

Figure 3.3: Illustration of the emission feature at 3563.4 Å. After subtraction of the model absorption profile, the residuals of the quasar spectrum were divided by the 1σ error spectrum. Plotted is the resultant signal-to-noise spectrum, smoothed with a 5-pixel boxcar filter. The emission feature, if Lyα, is blueshifted relative to the DLA line by $\approx 300\,{\rm km\,s^{-1}}$.

The wavelength centroid of the emission line is 3563.4 Å, and the measured line flux is $1.2 \pm 0.3 \times 10^{-16}{\rm erg\,cm^{-2}\,s^{-1}}$. However the spectrum of Fig. 3.1 has not been corrected for relative slit losses between the quasar and the spectrophotometric standard. These were substantial because the quasar was observed at large zenith distance. Therefore we calibrated our spectrum by firstly scaling to the spectrum of Osmer et al. (1994), and then scaling their spectrum to the literature UBV magnitudes. This brings the line flux to $\approx 3.5 \times 10^{-16}{\rm erg\,cm^{-2}\,s^{-1}}$, and indicates that we only captured about 35% of the flux. The new value for the line flux may still be an underestimate of the total line flux, dependent on the angular size of the emission-line region relative to the slit width. If the line is interpreted as Lyα emission the redshift of the object is $z_{\rm em} = 1.9312$, which is $300\,{\rm km\,s^{-1}}$ to the blue of the absorber. The line luminosity would be several times that for the DLA absorber towards PKS0528-250 (object S1, Paper I).

3.3.3 The emission redshifts of Q0151+048A, B

In considering the nature of the DLA absorber, and the object responsible for the emission line, it is important to measure accurately the redshift of the quasar. The Balmer lines or narrow forbidden lines can be used to measure the systemic redshift, but have yet to be

Table 3.3: Emission lines and derived emission-line redshifts

Object	Ion	$\lambda_{\rm vac}$ (Å)	$z_{\rm em}$ (peak)	$W_{\rm obs}$ (Å)	$W_{\rm rest}$ (Å)	$z_{\rm em}$ TF
Q0151+048A:	Lyα [a]	1215.67	[1.917]	140	48	
	NV[a]	1240.13	1.904	12.3	4.2	1.906
	SiII	1264.7	1.921	6.1	2.1	1.922
	OI	1304.46	1.924	11.9	4.1	1.924
	SiIV+OIV][b]	1399.7	[1.898]	41	14	
	CIV[b]	1549.1	1.908	64	22	1.911
	MgII[c]	2798.74	1.921			1.922
Q0151+048B:	MgII[c]	2798.74	1.936			1.937

[a] Measured after correction for DLA absorption

[b] From Sargent et al.1988

[c] Measured on spectrum in Meylan et al.1990

observed for this object. Instead we must use lines in the restframe UV. However it is well documented that the high ionization lines (e.g. CIV here) are blueshifted relative to the quasar systemic redshift by typically several hundred km s^{-1} (e.g. Espey 1989, Tytler & Fan 1992, Espey 1997). Any blueshift for the low ionisation lines (e.g. SiII, OI, MgII here) fortunately is small.

In Table 3.3 we collect values of the redshift measured for a number of lines in the spectrum of the quasar Q0151+048A, as well as the MgII line in the spectrum of the quasar Q0151+048B. All estimates are from fits to the line peak. The values for the weak SiII and OI lines are our own measurements from the spectrum of Fig. 3.2. For both of these lines we used rest wavelengths of both multiplets under the assumption that the lines are optically thick. The values for the Lyα and NV lines are also our own measurements from the spectrum of Fig. 3.2, but here after division by the model DLA line. This correction does not strongly add to the uncertainty of the NV emission redshift, but the error on the Lyα emission redshift is dominated by the uncertainty due to the absorption correction. The data for the SiIV and CIV lines are taken from Sargent et al. (1988). The SiIV redshift is not very useful however, as the line is chopped up by strong absorption lines, and it is only included in the table for the sake of completeness. The values for the MgII lines for the two quasars were measured by us from the plots of the spectra provided by Meylan et al (1990).

In a large study Tytler & Fan (1992) found that, after accounting for measurement errors, the intrinsic scatter of the blueshift of any particular line relative to the systemic redshift is small, no more than 200km s^{-1}, and they tabulated mean values of the blueshift for several

lines. The corrections are smallest for the low ionisation lines. For example for OI and MgII they found mean values of 50 and 100 km s^{-1} respectively. In the last column of Table 3.3 we list the redshifts (TF) after applying the corrections suggested by Tytler & Fan.

As discussed below, the corrections for the high-ionisation lines may not be suitable for bright quasars. Therefore to estimate the quasar systemic redshift we have formed a weighted mean of the redshifts for the three lines SiII, OI, MgII, and added 100 km s^{-1} to the final error as an estimate of the systematic uncertainty. Our best estimate of the systemic redshift for Q0151+048A is then $z = 1.922 \pm 0.003$. For Q0151+048B our best estimate for the redshift is based on the MgII line only, and is $z = 1.937 \pm 0.005$.

From Table 3.3 it can be seen that for the two high ionization lines, CIV and NV, the corrections suggested by Tytler & Fan are too small. The CIV line in Q0151+048A is blueshifted by 1440km s^{-1} relative to the systemic redshift, and this is much larger than the mean blueshift for this line of 310km s^{-1} quoted by Tytler & Fan. Espey (1997), and Møller (1997) have found several other cases of quasars where the CIV line is blueshifted by a similar, or larger, amount. Both Corbin (1990) and Espey (1997) find a correlation between blueshift of the CIV line and quasar brightness, and this is likely to be the explanation for the discrepancy, since the sample of Tytler & Fan contains very few optically bright quasars. In fact the correlation is visible in their Fig. 27. The correlation found by Espey would suggest a correction of $\approx$ 1100km s^{-1} for the CIV line for Q0151+048A, bringing it in line with the low ionisation lines.

To summarise, our best estimate for the systemic redshift of Q0151+048A is 1.922$\pm$0.003, which is 1250 ± 300km s^{-1} lower than the redshift of the DLA absorber.

3.4 Discussion

The redshift of the DLA absorber towards Q0151+048A is larger than the redshift of the quasar, so the system resembles the $z_{\rm abs} \approx z_{\rm em}$ damped absorber at $z = 2.81$ towards the quasar PKS0528-250, for which we have previously reported the detection of Lyα emission (Sect. 3.1). The detection of emission in the trough of the Q0151+048A absorber therefore makes the resemblance closer. The line could be Lyα emission from the absorber or from a companion. We defer a detailed discussion of the nature of the emitter to a subsequent paper, where we will report on narrow-band imaging observations of the line (Fynbo et al. 1999a). However it is interesting to note that Pettini et al. (1995) have discovered a similar, slightly offset, emission line in the trough of a third $z_{\rm abs} \approx z_{\rm em}$ damped absorber, towards the quasar 2059-360. It appears, therefore, that Lyα emission may be more common in or near DLA absorbers near quasars than in or near intervening DLA absorbers. Therefore in this section we firstly consider whether these $z_{\rm abs} \approx z_{\rm em}$ DLA absorbers are representatives of a different population to the intervening DLA absorbers. Two possibilities are considered;

that the clouds belong to the class of intrinsic absorbers, probably ejected by the quasar, or that we are seeing the disks of the host galaxies. Both possibilities are rejected, so it is probable that the $z_{\rm abs} \approx z_{\rm em}$ DLA absorbers are similar to intervening DLA absorbers. This leads us to consider briefly the likely reason for enhanced Lyα emission near quasars.

In the following we limit ourselves to a discussion of the Q0151+048A and PKS0528-250 systems, as the relevant information for the quasar 2059-360 has yet to be published.

3.4.1 The nature of $z_{\rm abs} \approx z_{\rm em}$ DLA systems

Intrinsic $z_{\rm abs} \approx z_{\rm em}$ systems

If the $z_{\rm abs} \approx z_{\rm em}$ DLA absorbers are different from the intervening systems, one possibility is that they belong to the class of intrinsic absorbers, which includes the broad absorption lines (BALs), and the narrow intrinsic $z_{\rm abs} \approx z_{\rm em}$ systems optically thin in the continuum (Savaglio et al.1994; Møller et al.1994; Hamann 1997), which are possibly related to BAL systems. Both types of intrinsic absorber typically display complex, but generally smooth absorption profiles (e.g. Barlow & Sargent, 1997), whereas both the damped systems under discussion are well fit by single-component Voigt profiles. Intrinsic $z_{\rm abs} \approx z_{\rm em}$ systems also typically have very high metal abundances, solar or several tens times solar (Petitjean et al.1994; Møller et al.1994; Hamann 1997). The metallicity of the DLA absorber in PKS0528-250, on the other hand, was measured by Meyer et al.(1989) to be only 12% solar, and by Lu et al.(1996) to be 17% solar. These values are representative of other DLA absorbers. The metallicity of the Q0151+048A DLA absorber has yet to be measured.

The intrinsic $z_{\rm abs} \approx z_{\rm em}$ systems are also typically characterised by high ionization parameter. If one were to increase the column density of such a system to the point where it became optically thick to Lyman continuum photons, low ionization absorption lines would become visible. However, the part of the cloud facing the quasar would remain highly ionized, and one would have a system with mixed ionization (strong CIV and NV as well as SiII and CII). However neither of the DLA systems under discussion show strong NV absorption. Therefore, on the basis of absorption profile, metallicity, and ionisation parameter these two absorbers appear to be representative of other DLA absorbers, rather than the intrinsic $z_{\rm abs} \approx z_{\rm em}$ systems.

Quasar host galaxies

Another possible explanation might be that we are seeing neutral gas in the quasar host galaxy disk. However for Q0151+048A the quasar systemic redshift 1.922 ± 0.003 (§3) and the absorber redshift $z = 1.9342 \pm 0.0003$ are significantly different. The same is probably true of PKS0528-250. Here the absorber redshift is 2.8115 ± 0.0007, which differs from the quasar emission redshift 2.768 ± 0.002, measured by us from the CIV line, by 3440km s^{-1}. As

discussed in §3 the systemic redshift of the quasar will be higher than the value measured from the CIV line. However, if we follow Tytler & Fan (1992) the correction is only 310km s^{-1}, whereas Espey's (1997) work would suggest a correction of no more than $\approx$ 1500km s^{-1}. Therefore these two DLA absorbers do not appear to be the signatures of disks of the quasar host galaxies.

3.4.2 Lyα emission and the effect of the quasar

If, as strongly suggested by the above discussion, the $z_{\rm abs} \approx z_{\rm em}$ DLA systems are the same as intervening DLA systems, the enhanced Lyα emission in or near the $z_{\rm abs} \approx z_{\rm em}$ absorbers implies that they occupy different environments to the intervening systems. The most obvious explanation that comes to mind is that the emission lines in the troughs of the Q0151+048A and 2059-360 absorbers, if Lyα , are due to photoionisation by the quasar. However, one can imagine several other possible explanations for the enhanced emission. For example gravitational interaction between the quasar and absorber might induce star formation. In any case the Lyα emission from the PKS0528-250 DLA appears to be due to star formation, as we have detected continuum emission from the absorber, as well as from two Lyα emitting companions (Paper III). This might suggest, instead, that the explanation for enhanced Lyα emission near quasars is that quasar activity (whatever the cause) is more common in regions where young galaxies are actively forming stars.

Another factor which could play a rôle is the so called proximity effect (e.g. Bajtlik et al.1988). Powerful quasars are able to ionize the neutral hydrogen in the Lyman forest out to large distances from the quasar. The effect of this would be to reduce any line blanketing of Lyα emission from galaxies in the vicinity of the quasar. Although the average line blanketing in the Lyα forest of the continuum of a quasar is only modest at this redshift, ~ 0.3, the average line blanketing of the Lyα emission line of a galaxy might be greater as it would be enhanced by the cloud-galaxy correlation function.

3.5 Summary and conclusions

1. In this paper we have presented spectra of the quasar Q0151+048A, and found evidence for emission in the trough of the $z_{\rm abs} \approx z_{\rm em}$ DLA absorption line at $z = 1.9342$.

2. We have previously reported the detection of Lyα emission from the $z = 2.81$ $z_{\rm abs} \approx z_{\rm em}$ DLA system towards the quasar PKS0528 $-$ 250, while an emission line in the trough of a third $z_{\rm abs} \approx z_{\rm em}$ DLA absorber, at $z = 3.083$, has also recently been reported. There is only one published successful detection of Lyα emission from an intervening DLA absorber, so these results suggest that Lyα emission is more common in or near $z_{\rm abs} \approx z_{\rm em}$ DLA absorbers than in or near intervening DLA absorbers.

3. Despite this we find no evidence that $z_{\rm abs} \approx z_{\rm em}$ DLA absorbers are not members of the same population as intervening DLA absorbers. In particular we are unable to make a connection between the $z_{\rm abs} \approx z_{\rm em}$ DLA absorbers and the so-called intrinsic absorbers, which are of higher metallicity and higher ionisation. Neither is it possible to associate the $z_{\rm abs} \approx z_{\rm em}$ DLA absorbers with the disk of the quasar host galaxy, as the redshifts of the absorbers are not compatible with the measured quasar systemic redshifts.

4. Star formation is almost certainly the cause of the Lyα emission from one of the three absorbers discussed here. Photoionisation by the quasar could be the explanation for the other two emission lines, but this can only be established by more detailed studies, and other explanations are possible.

Acknowledgments

We wish to thank Brian Espey who calculated the emission line redshift corrections given in sections 3.3 and 4.1.2 using his semi-empirical correlation, Pat Osmer for supplying us with his spectrum of Q0151+048A, and Fred Hamann for a number of useful comments on an earlier version of this manuscript. JUF gratefully acknowledges support from the STScI visitors programme.

Chapter 4

Extended Lyα emission from a damped Lyα absorber at z = 1.93, and the relation between DLAs and Lyman-break galaxies

Fynbo, J.U., Møller P., Warren S.J., 1999, MNRAS, **305**, 849

4.1 Introduction

The quest for non-active galaxies at high redshift has gone through a dramatic change in the last few years. The number of galaxies at z>2 found using the Lyman-break technique (Steidel et al. 1996b) is now counted in hundreds, providing information on the global density of star formation at early epochs, and the evolution of galaxy clustering. A different perspective on the formation of galaxies is obtained by studying the population of damped Lyα absorbers (DLAs), the objects responsible for the strongest absorption lines seen in the spectra of quasars. The advantage of DLAs is that they provide a wealth of information on the chemical evolution of galaxies in the form of the measurement of the metallicity and dust content of the gas (e.g. Lu et al. 1996, Pettini et al. 1997a,b, Kulkarni & Fall 1997). The DLAs have column densities larger than 2x10^{20} cm^{-2}, comparable to the column density for a sightline through the disk of a nearby spiral galaxy. In addition the total gas content in DLAs is similar to the mass in stars and gas at the present epoch (Wolfe et al. 1995). For these reasons DLAs are widely believed to be the gas reservoirs from which todays spiral galaxies formed.

The relation between DLAs and Lyman-break galaxies (LBGs) is unclear at present because very few DLAs have been unambiguously detected in emission. At low and intermediate redshifts $z < 1$ a number of candidate counterparts of DLAs have been discovered in deep images (Steidel et al. 1994, 1995b, LeBrun et al. 1997). These candidates display a mix of morphological types from spiral galaxies to very compact objects (LeBrun et al. 1997), but so far none has spectroscopic confirmation. At high redshift there are three DLAs which have been imaged and for which confirmatory spectroscopy exists; the DLA at z_{abs}=2.81 towards PKS0528–250 (Møller & Warren 1993b), the DLA at $z_{abs} = 3.150$ towards Q2233+131[1] (Djorgovski et al. 1996), and the DLA at $z_{abs} = 4.10$ towards DMS2247-0209 (Djorgovski 1998). The first of these has been imaged with HST (Møller & Warren 1998) and has a continuum half light radius of 0.13 ± 0.06 arcsec, similar to that measured for the LBGs (Giavalisco et al. 1996a).

Information on the gas sizes of DLAs comes from the measured impact parameters. Combined with the line density of absorbers dn/dz the space density may be computed. Møller & Warren (1998) produced a preliminary estimate of the space density of high-redshift DLAs by using the impact parameters of confirmed and candidate counterparts. The data suggest that for $q_0 = 0.5$ the space density of DLA clouds at $z > 2$ is more than five times the space density of spiral galaxies locally. For $q_0 = 0.0$ there is no evidence as yet that DLA clouds are more common than spiral galaxies locally. A single measurement of 21cm absorption against an extended radio source, the quasar 0458-020, by Briggs et al. (1989),

[1]When comparing DLA emitters to statistical samples of DLA absorbers, it is important to remember that this object does not meet the N(HI) criterion of a DLA absorber. Statistically speaking this is a Lyman–Limit System

provides additional information on the size of DLAs. Their analysis indicates that the DLA seen in the spectrum of this quasar has a gas size greater than $8h^{-1}$ kpc.

It would clearly be useful to image more high-redshift DLAs, to understand better their relation to LBGs, but also to measure the star formation rates and connect these to the rate of consumption of gas (Pei & Fall 1995). In this paper we present observations of a DLA in the field of the quasar pair Q0151+048A (qA) and Q0151+048B (qB). The two quasars have very similar redshifts z_{em}=1.922 and 1.937 respectively (Møller et al. 1998), and an angular separation of 3.27±0.01 arcsec. The spectrum of qA contains a DLA at z_{abs} = 1.9342, close to the emission redshift, and this was the reason we originally chose this system for study because of the possibility of detecting Lyα emission due to photoionisation by either of the quasars (see Møller & Warren (1993a,b) for a detailed discussion of the predicted effect). In Møller et al. (1998), we presented a spectrum of qA which shows an emission line in the DLA trough, detected at 4σ. The present paper describes follow–up narrow–band and broad–band imaging observations of this system.

In Sect. 4.2 we describe the observations and the data reduction. In Sect. 4.3 we describe the PSF-subtraction of qA and qB and the photometry of the objects found in the field. In Sect. 4.4 we discuss the results obtained. Throughout this paper we adopt $q_0 = 0.5$, $H_0 = 100h$ km s^{-1} Mpc^{-1} and $\Lambda = 0$ unless otherwise stated.

4.2 Observations and Data Reduction

The data were obtained with the 2.56-m Nordic Optical Telescope (NOT) during four nights beginning September 15, 1996. Observations of the Q0151+048A,B field were done in three bands: the standard U and I filters, and a special narrow–band filter manufactured by Custom Scientific. The narrow–band filter (CS 3565/20) is tuned to Lyα at the redshift of the DLA $z = 1.9342$. It has a central wavelength of λ3565Å and a full width at half maximum (FWHM) of 20Å. The peak transmission of the filter is $T(\lambda)_{max} = 0.385$ and red leak is less than 10^{-6} to 1.2 μ. The CCD used was a 1024^2 back-side illuminated thinned Tektronix with a pixel scale of 0.1757±0.002 arcsec and read noise of $5.4e^-$. The QE in the near UV for this detector rises from 0.3 at 3500Å to 0.6 at 4000Å.

Conditions were photometric during most of the run allowing accurate calibration data to be obtained. The seeing ranged from 0.80 arcsec to 1.35 arcsec FWHM in the narrow–band frames and from 0.60 arcsec to 1.30 arcsec FWHM in the U and I frames. Integration times were in most cases 4000 seconds for the narrow–band frames, 1000 seconds for the U, and 300 seconds for the I, ensuring that the noise in each frame is dominated by photon noise from the sky and not by read noise. Between exposures the telescope pointing was jittered in steps of 2 to 5 arcsec to minimize the effect of bad pixels. The total integration times in the different filters are listed in Table 4.1, together with the measured seeing in the

Table 4.1: Observations of Q0151+048A,B, 1996 Sept 15 – 18

Filter	Combined seeing	Exposure sec
CS 3565/20	1.1	62700
U	0.9	12000
I	0.8	7800

combined frames. For the calibration we observed Landolt (1992) photometric standards for the broad–band data, and the HST spectrophotometric standards GD71, BD+28°4211 and BD+25°4655 (Colina & Bohlin 1994) for the narrow–band data.

Bias and dark frames were firstly subtracted from the data frames. Twilight sky frames were obtained and were used to flatten the U and I data directly. For the narrow–band frames however we found that the instrument setup allowed a small, but significant, amount of light to reach the CCD without passing through the filter. This additional source of background light, which could be either light scattered around the filter wheel or light leaking through the camera enclosure, was too weak to be detectable in the broad–band images, but was a very significant contribution in the narrow–band images. Here we shall refer to this source as scattered light.

The scattered light produced a pattern mostly across the upper two thirds of the CCD. We applied a correction for this as follows. Firstly the contribution to the twilight sky frames was measured by placing a blocking filter in the filter wheel. From these frames we determined a model of the scattered light by median and Gaussian filtering. This model was then scaled and subtracted from the flat frames prior to the creation of the normalised master-flat. The scattered light in the data frames did not have exactly the same structure across the CCD as in the flat-field frames. The reason for this is not known, but it is possibly due to a different position of the guide probe. We therefore modelled the scattered light in the data frames by summing all the frames, having removed all objects by interpolation and filtering. This model was then scaled to, and subtracted from, the individual data frames. After flat fielding the residual large scale variations left were less than 5%.

The frames for each filter were then divided in two groups depending on whether the seeing was greater or smaller than 1 arcsec FWHM, in order to optimize the combination of the frames. Both groups were then registered by integer pixel shifts to a common coordinate system and the frames within each group were combined using the optimal combination code described by Møller & Warren (1993b), which maximizes the signal–to–noise ratio for faint sources. The model for the scattered light was included in the calculation of photon noise from the sky. Finally, the two summed frames for each filter were combined by weighting by

Table 4.2: Measured rms of sky surface brightness. For the narrow–band we provide a range due to the presence of the scattered light gradient across the field.

passband	rms SB
	mag. arcsec^{-2}
I(AB)	26.9
u(AB)	28.2
n(AB)	25.7-25.8

the inverse of the sky variance.

All magnitudes quoted in this paper are on the AB system. The narrow–band data were calibrated directly onto the AB system, and magnitudes are denoted $n(AB)$. For the U band we determined the colour equation $u = U + 0.26(U - B)$ relating the instrumental magnitude u to the standard Johnson U. The fit to the U colour equation used data for seven different stars but is not well determined. There was substantial scatter about the fit near $U - B = 0$, ~ 0.05 mag., and evidence that the relation is non–linear. Such results are typical for this band (e.g. Bessell 1990). The instrumental magnitudes u were converted to AB magnitudes using the equation $u(AB) = u + 0.49$, determined by integrating the spectrum of the star GD71 over the passband. Here we have retained the lower case u for the AB magnitude indicating that the effective wavelength of the filter lies significantly away from the standard value. The colour term for the I filter is consistent with zero i.e. $i = I$, and we used the equation $I(AB) = I + 0.43$ (Fukugita et al. 1995) to put the magnitudes onto the AB system. Details of the sky noise in the combined images are provided in Table 4.2.

4.3 Results

The field of the quasar pair is illustrated in Fig. 4.1 which shows the final combined I (upper) and narrow–band (lower) images. The quasars Q0151+048A,B lie near the centre and are marked qA and qB. Also marked on the image are two bright stars (psfA and psfB) and a source, named S5, to be discussed later (Section 3.3).

4.3.1 Lyα emission near Q$0151 + 048$

In the narrow–band image faint emission is seen extending to the east of qA. To get a clearer view of this in Fig. 4.2a (upper panel) we show a contour plot of a small section from the centre of the narrow–band image. Here, in addition to the images of the two quasars, a plume of emission, presumably Lyα from the DLA, is clearly seen extending towards the east of qA. To reveal the full extent of the Lyα emission we subtracted the images of the

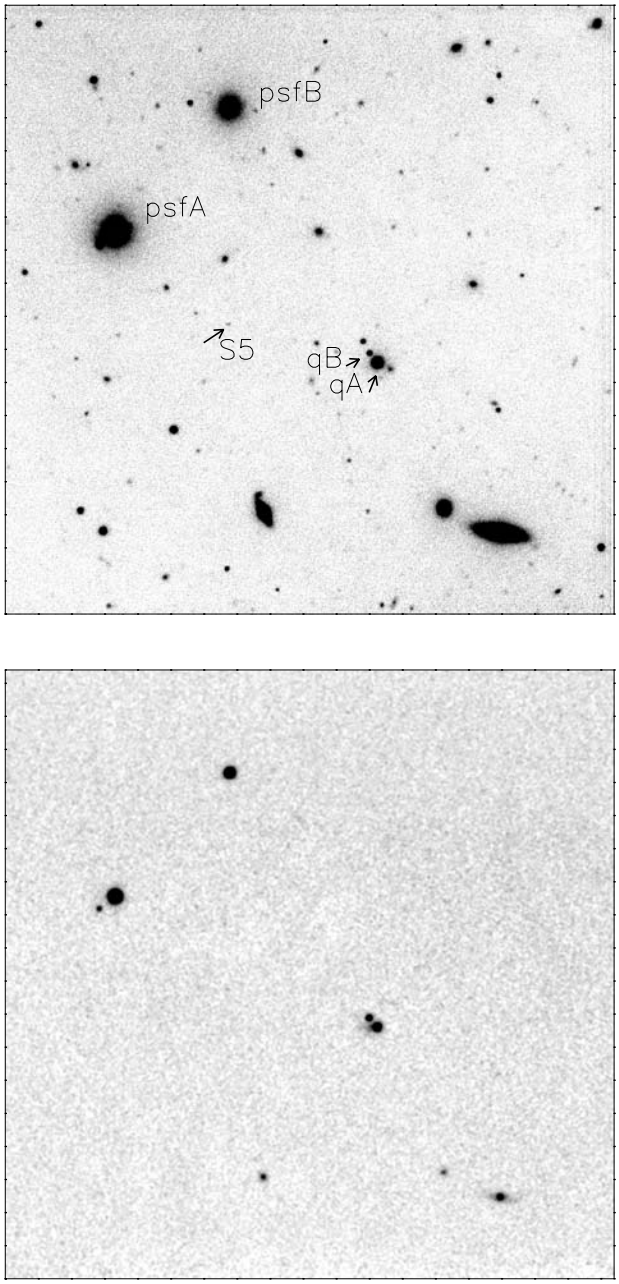

Figure 4.1: Field containing the quasar pair Q0151+048A,B. *Upper:* combined I frame, *Lower:* combined narrow–band frame. The field shown is 920x920 pixels, 162x162 arcsec^2. North is up and east to the left. The two quasars are marked qA and qB. The two bright stars marked psfA and psfB were used for determination of the point spread function. The galaxy marked S5 is discussed in the text (Section 3.3).

two quasars as follows.

The two bright stars marked psfA and psfB in Fig. 4.1 were used with DAOPHOT II (Stetson 1997) to define the point-spread function (PSF). The complex image made up of the extended Lyα emitter super–imposed on the images of the two quasars was decomposed by iteration. First DAOPHOT II was used to fit, and subtract, the two point sources. Because of the Lyα emission this will oversubtract the point sources. We then used a galaxy model to fit the residuals finding the minimum-χ^2 fit of the model convolved with the psf (as in e.g. Warren et al. 1996). The model consists of an exponential surface-brightness profile $\Sigma = \Sigma_s exp(-r/r_s)$, and elliptical shape with constant ellipticity and orientation. Here r is equal to $\sqrt{(ab)}$ i.e. the geometric mean of the semi-major and semi-minor axes. We tried a range of surface-brightness profiles but the exponential function provided the best fit. The best-fit galaxy model was then subtracted from the original image, and a second iteration of DAOPHOT II fitting to the quasar images followed. After 9 rounds of alternating point source subtraction and exponential-disc fitting the procedure reached a stable solution. The frame after subtraction of the images of the two quasars is shown in Fig. 4.2b. The parameters of the fit are $r_s = 0.95$ arcsec, a central surface brightness of 3.3×10^{-16} erg s^{-1} cm^{-2} arcsec^{-2}, ellipticity $e = 0.53$, and PA 98° (E of N). The probability associated with the χ^2 of the final fit to the Lyα emission is 4%. This rather small value is explained by the asymmetric light profile which falls off more sharply to the W than to the E.

In Fig. 4.2b emission is seen from an elongated structure of dimensions approximately 6 x 3 arcsec^2. In the following we shall refer to this source of Lyα emission as S4. To perform photometry of objects in the field we used the package SExtractor (Bertin & Arnouts 1996) and determined *isophotal* magnitudes and so called *Automatic Aperture* magnitudes (AAMs), as described below. The magnitudes of the three objects S4, qA, and qB, were measured individually in frames from which the images of the other two objects had been subtracted. The magnitudes of other objects in the vicinity were measured in frames from which all three images had been removed.

With the exception of S4 the apertures for the *isophotal* magnitudes were set by reference to the frame formed by summing the combined frames for the three passbands. This frame was convolved with a Gaussian detection filter with FWHM equal to the seeing. The isophotes set at 1.5 times the noise measured in the unconvolved frame defined the apertures and the same apertures were then applied to each passband. The detection limit for faint objects was set at a minimum aperture size of 5 pixels (total). Hence, the *isophotal* magnitudes provide photometry appropriate for accurate colour determination. For S4 the same procedure was followed, but only the narrow–band frame was used. Finally, since the catalogue is defined by detection in the three-passband combination frame, we also ran SExtractor on the narrow–band frame and found that, with the exception of S4, no source detected in the narrow–band frame at $S/N > 4$ had been overlooked.

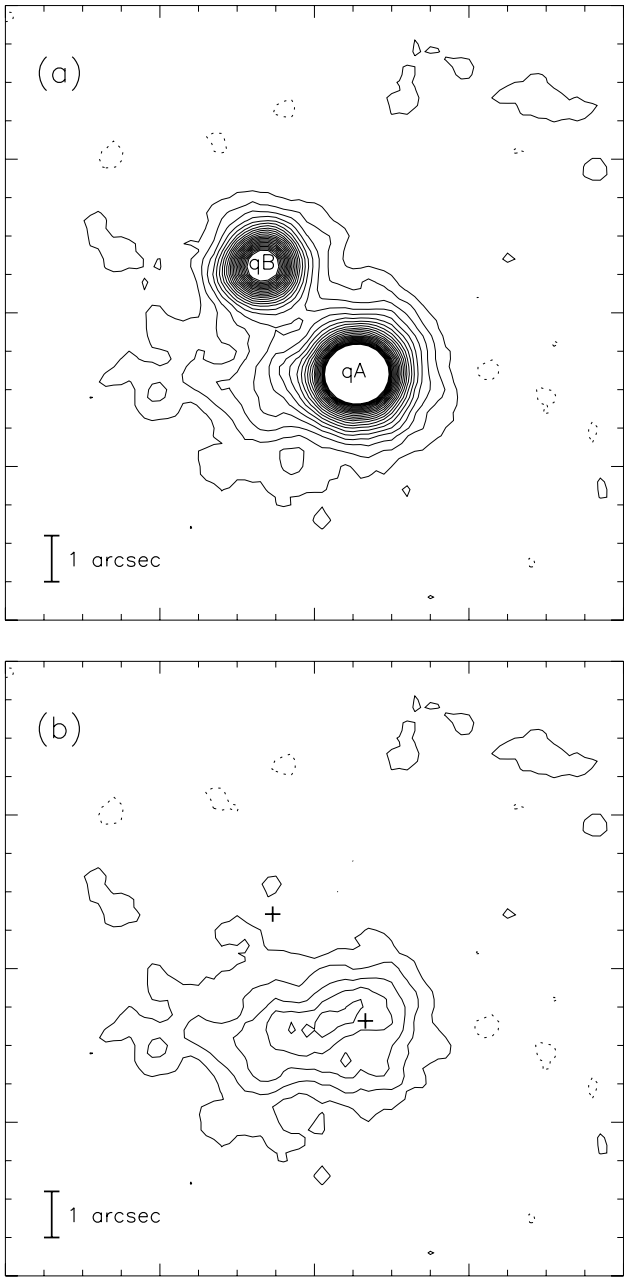

Figure 4.2: Contour plot of the narrow–band frame showing the 80x80 pixels region, 14x14 arcsec^2, surrounding the two quasars. North is up and east to the left. The frame has been smoothed by convolution with a Gaussian with σ corresponding to the PSF. *Upper:* final combined frame showing the two quasars marked qA and qB and excess emission east of qA. The contour levels are at -3, 3, 6, 9, ... $\times 10^{-17}$ erg s^{-1} cm^{-2} arcsec^{-2}, with the dotted contours being negative. *Lower:* final combined frame (same contour levels as above) after subtraction of the quasar images, revealing Lyα emission from the object S4 over a region 6x3 arcsec^2. The positions where quasar psfs were subtracted are marked by crosses.

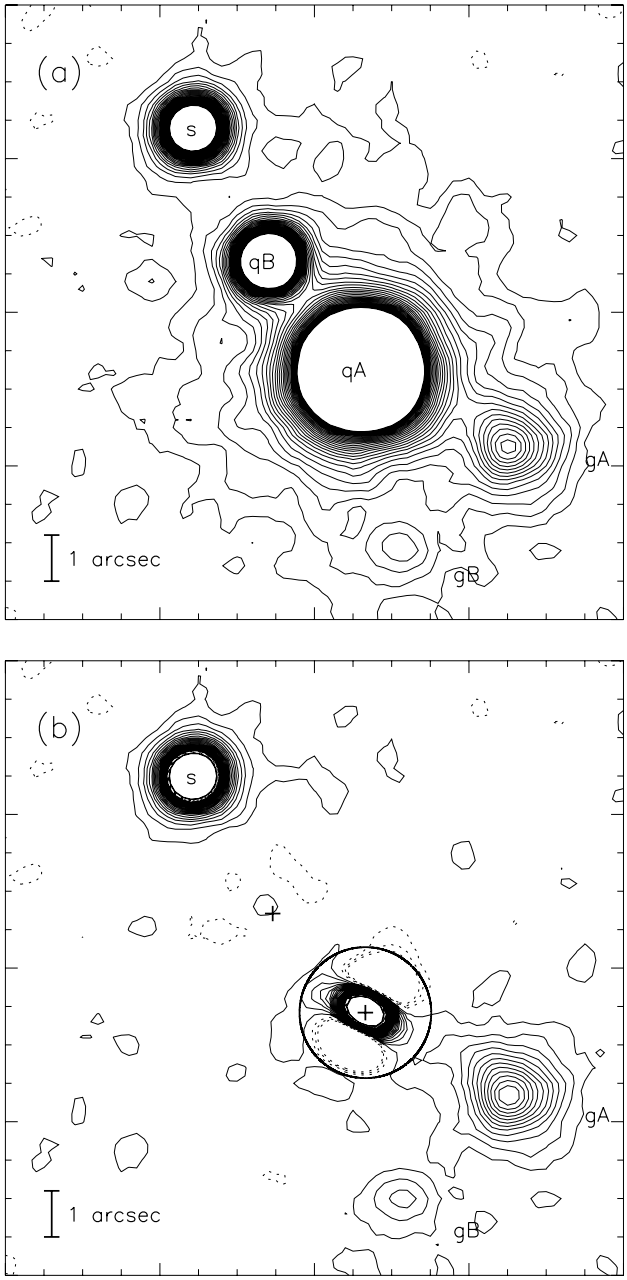

Figure 4.3: I–band contour plot of the same field as in Fig. 4.2. *Upper:* final combined frame showing, in addition to the two quasars, two faint galaxies marked gA and gB, and a star marked s. The contour levels are -9, -6, -3, 3, 6, ... $\times$ 1σ of the skynoise, with the dotted contours being negative. *Lower:* final combined frame (same contour levels as above) after subtraction of the quasar images.

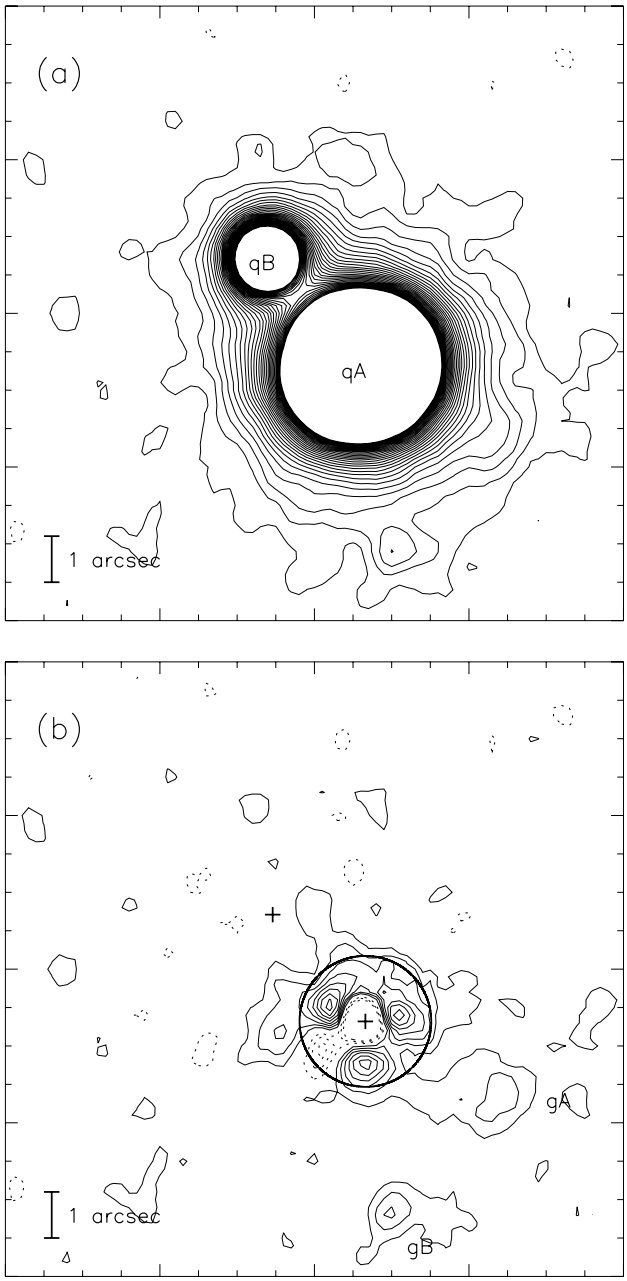

Figure 4.4: U–band contour plot of the same field as in Fig. 4.2. *Upper:* final combined frame showing the two quasars. The contour levels are -9, -6, -3, 3, 6, ... $\times 1\sigma$ of the skynoise, with the dotted contours being negative. *Lower:* final combined frame (same contour levels as above) after subtraction of the quasar images.

Table 4.3: Photometric properties of the quasars qA and qB, of the faint galaxies S4, S5, gA and gB, and of the star s. Magnitudes of extended objects have been determined in two apertures (isophotal and AAM, both defined in Sect. 3.1). For the point sources we only provide AAM. Note that magnitudes marked ^{a} are not true AAM magnitudes, they were determined via scaling of the fitted exponential–disk model as detailed in Sect. 3.2. Lower limits to magnitudes (upper limits to fluxes) are 2σ. For gA and gB the determination of reliable apertures for AAM was impossible due to the nearness of strong residuals of the QSO PSF-subtraction.

Object	u(AB)	I(AB)	n(AB)	Apert. (pix)
Isoph.				
S4			20.76 ± 0.05	254
S5	24.60 ± 0.10	24.04 ± 0.09	24.1 ± 0.2	37
gA	24.28 ± 0.12	22.00 ± 0.04	> 24.0	170
gB	26.0 ± 0.2	24.88 ± 0.14	> 25.3	18
AAM				
qA	17.90 ± 0.02	17.49 ± 0.02	19.72 ± 0.04	241
qB	21.07 ± 0.03	20.87 ± 0.02	20.04 ± 0.03	241
s	> 25.6	20.98 ± 0.02	> 23.8	341
S4	$22.9^a \pm 0.2$	$22.8^a \pm 0.3$	19.95 ± 0.04	690
S5	24.01 ± 0.09	23.70 ± 0.11	23.6 ± 0.2	241

The AAM is intended to give the best estimate of the total flux and is measured using an elliptical aperture with minor axis $b = 2.5 r_1 \epsilon$ and major axis $a = 2.5 \frac{r_1}{\epsilon}$, where r_1 is the first moment of the light distribution and ϵ is the ellipticity. The isophotal narrow–band magnitude and the AAM for S4 correspond to fluxes of $9.0 \pm 0.4 \times 10^{-16}$ and $1.91 \pm 0.07 \times 10^{-15}$ erg s^{-1} cm^{-2} respectively. The AAM for S4 (n(AB)=19.95 ± 0.04) agrees well with the total magnitude of the fitted galaxy model (n(AB)=20.01).

4.3.2 Broad–band photometry of S4

Fig. 4.3a shows a contour plot of the I band image of the same field as in Fig. 4.2. Here we see the two quasars, a star north–east of the quasars which was not visible in the narrow band image, and two faint galaxies marked gA and gB south–west of the quasar qA. In Fig. 4.3b psfs have been subtracted at the positions of the two quasars, leaving behind only the star and the two faint galaxies. In Fig. 4.3b we have also overlaid a circle of radius 1.5 arcsec centred on the position of qA. The strong residuals from the psf–subtraction prevent

any detection of additional faint sources within this region.

In Fig. 4.4a we show the U–band contour plot of the same region, and in Fig. 4.4b again the field after subtraction of the quasar images. Also in Fig. 4.4b we have overlaid a circle of radius 1.5 arcsec centred on the position of qA. In the psf–subtracted U image we see the two faint galaxies gA and gB, but in addition there is a faint extension about 2 arcsec east of qA, roughly at the position of S4.

The narrow band image shows that S4 is extended and that it covers the bright quasar qA. Therefore, when observed through a broad band filter the tail of the psf of qA extends across most of S4 and will, even under good seeing conditions, make the determination of broad–band magnitudes of S4 an extremely difficult task. Simple aperture photometry, after fitting and subtracting the quasar psf, is not possible because of the strong residuals from the psf–subtraction, and because there is a degeneracy in the determination of how much of the faint extended flux is due to the tail of the quasar psf, and how much is due to S4. In order to break this degeneracy, and to obtain an objective measure for the broad–band magnitudes of S4 we proceeded as follows:

On the assumption that the broad–band flux can be fitted by the exponential–disk model defined by the fit to the narrow–band flux, we firstly subtracted a scaled narrow–band model from the broad band image. We then subtracted a psf at the position of qA. The quasar psf was scaled so that the integrated residual flux measured in a rectangular aperture (5.6 arcsec by 3.3 arcsec) covering both the quasar and the central region of S4, was exactly zero. This calculation was performed for a range of values of the scaling of the model for S4, and for each combination of S4–model and quasar psf the total χ^2 of the fit to the data was calculated. The I and U band magnitudes of S4 provided in Table 4.3 are those corresponding to the quasar–psf/S4–model combinations providing the minimum χ^2. The errors quoted are those where χ^2 increased by one. The rectangular aperture was defined so as not to include flux from the galaxy gA. The χ^2 was calculated in a smaller aperture to exclude the central part of the quasar psf where it would be dominated by noise from the strong central psf–residuals. Table 4.3 provides a summary of the photometry of the object S4, both quasars, and several other objects found in the field.

Møller & Warren (1998) found evidence that a DLA–galaxy at z=2.81, as well as its two companion galaxies, all had one (or more) compact cores of continuum–emission, while the Lyα emission from the same objects extended over larger areas. If this is a general feature of high redshift galaxies we could expect to see one (or several) continuum emitting cores in S4. Our current data are not adequate to resolve this question. Clearly higher resolution and deeper broad–band imaging is required.

4.3.3 The impact parameter b_{DLA} of S4

In Møller & Warren (1998) the DLA impact parameter b_{DLA} was defined as the projected distance between the line–of–sight to the quasar to that of the centroid of the continuum flux of the DLA absorber. In the case of Q0151+048 we clearly see extended Lyα emission from the DLA absorber, and our analysis of the broad band data shows that they are not inconsistent with a broad–band flux distribution identical to that of the Lyα flux. The centroid of the model fit to the narrow–band data is located 0.93 arcsec east, 0.03 arcsec south of Q0151+048A ($b_{DLA,Ly\alpha} = 0.93$ arcsec), and we shall for now adopt this as the impact parameter of the DLA in Q0151+048A.

4.3.4 Lyα in the surrounding field

An object with Lyα emission at z=1.93 will appear bright in the narrow–band compared to U and I, so we can use the results of the photometry to search for other Lyα emitters in the field. In Fig. 4.5 we plot the $n(AB) - u(AB)$ *versus* $n(AB) - I(AB)$ two–colour diagram for all objects detected at a signal–to–noise ratio larger than 4 in the narrow–band frame. Strong Lyα emitters at $z = 1.93$ will lie in the lower left region of this diagram. Conversely an object with absorption in the narrow–band filter will lie in the upper right corner. Since our narrow–band filter is fairly well centred in the U–band most objects will have zero $n(AB)-u(AB)$ colour, and horizontal lines in Fig. 4.5 are to a good approximation lines of constant equivalent absorption or emission line width. Lines of constant continuum $U - I$ will appear as diagonals in Fig. 4.5 with the bluest objects in the upper left corner and red objects in the lower right. The dashed curve shows the location of a series of simulated objects with identical power–law continuum on which is superimposed absorption or emission lines of different strengths in the narrow pass–band. The curve mostly falls along a diagonal of the constant $U - I$ of the continuum, but bends to the left as the emission line starts to dominate the flux in the U–band filter. The dashed curve approaches asymptotically a model with an emission line of infinite equivalent width (dot–dash line).

The quasar qA lies in the upper part of the diagram, as expected because of absorption by the DLA. Conversely the quasar qB lies in the lower left part of the diagram. The filter is too narrow to contain all of the Lyα emission line for the quasar qB, but even so the $n(AB) - u(AB)$ implies that the mean flux level over the narrow–band filter is at a level three times greater than the average over the U band. Therefore the DLA seen in the spectrum of the quasar qA cannot be present in the spectrum of qB. If the quasar qB also lies behind the cloud responsible for the DLA, then the column density is much lower at the position of qB.

There is another candidate Lyα emitter seen in Fig. 4.5, marked S5. The location of this candidate is shown in Fig 4.1. The object is detected at a S/N of 4.8, 14, and 13 in

Table 4.4: Measured Lyα luminosities in high-redshift DLAs

quasar	z_{em}	z_{abs}	luminosity	reference
Q0151+048	1.92	1.93	1.2 x 10^{43} h^{-2}	this paper
PKS0528–250	2.79	2.81	1.1 x 10^{42} h^{-2}	Møller & Warren (1993b)
Q2059-360	3.10	3.08	3.7 x 10^{42} h^{-2}	Pettini et al. (1995), Leibundgut & Robertson (1998)
Q2233+131	3.30	3.15	1.2 x 10^{42} h^{-2}	Djorgovski et al. (1996)

the narrow, U, and I band images respectively. The corresponding flux of the candidate Lyα line is $6.6 \pm 1.3 \times 10^{-17}$ erg cm^{-2} s^{-1} and the restframe equivalent width of the line is 9Å±2Å. The angular separation of S5 from the line of sight to the quasar is 40.9 arcsec, which corresponds to 169 h^{-1} kpc (q_0=0.5) and 263 h^{-1} kpc (q_0=0.0) at $z = 1.93$.

4.4 Discussion

4.4.1 The origin of the large Lyα luminosity

The Lyα luminosity of S4 is 1.2 x 10^{43} h^{-2} erg s^{-1}. Other high redshift DLAs for which the Lyα flux has been measured are the DLA at $z = 2.81$ towards PKS0528–250 (Møller & Warren 1993b), the DLA at $z_{abs} = 3.150$ towards Q2233+131 (Djorgovski et al. 1996), and the DLA at $z_{abs} = 3.083$ towards Q2059–360 (Pettini et al. 1995, Robertson & Leibundgut 1997, Leibundgut & Robertson 1998). The last is a spectroscopic detection of spatially resolved excess emission in the DLA absorption trough. The Lyα luminosities for these DLAs are collected in Table 4.4 and we have assumed a flux of 2 x 10^{-16} erg s^{-1} cm^{-2} for Q2059–360 based on details in Leibundgut & Robertson (1998). The measured luminosity for Q0151+048 stands out, being several times larger than the other values. In this section we consider possible explanations for this anomaly.

In the light of the dearth of successful detections of emission from DLAs it is noticeable that of the four high-redshift DLAs listed in Table 4.4, three have redshifts close to the quasar emission redshift. This point was noted by Møller et al. (1998) who suggested that photoionisation by the quasar was a plausible explanation for the Lyα emission for Q0151+048 and Q2059–360, although not for PKS0528–250 where the continuum emission detected from the DLA is sufficient to account for the Lyα emission (Møller & Warren, 1998), and where recent spectroscopic observations (Ge et al. 1997) has ruled out that the quasar could be the source of the ionisation. In the case of Q0151+048 there are two quasars potentially close to the DLA galaxy. Q0151+048B is not only close to the line of sight to the DLA galaxy, it also has a redshift (1.937 ± 0.005, Møller et al. 1998) consistent with

being identical to that of the DLA galaxy. For this reason, one may slightly favour qB as the source of ionization. Q0151+048A, on the other hand, has a redshift which (if interpreted as due to peculiar motion) indicates that it is moving towards qB and the DLA galaxy with a velocity of about 1200 km s^{-1}. We now consider the possibility of photoionisation for the Q0151+048 DLA galaxy in more detail.

The relative distances of qA, qB, and the DLA cannot be determined from the redshifts because of peculiar velocities. The DLA lies in front of qA, since it absorbs it, but qB could lie either at larger or smaller distance than the DLA. If qB is beyond the DLA then the region of high-column density of the absorber does not extend across it. This is because the $n(AB) - u(AB)$ colour of qB corresponds to an average flux level in the n band of three times the continuum level (Fig. 4.5), so the Lyα emission line of qB is not strongly absorbed. One possible explanation for the extended Lyα emission is that qB lies nearer than the DLA and lights up the near face of the absorber (Fynbo et al. 1998). However it is also possible that qA is the source of photoionisation. Since qA under this assumption illuminates the backside of the absorber, in the simplest picture one would expect to see a hole in the Lyα emission, containing the line of sight to the quasar, over the area where the optical depth is high since over this region the Lyα photons escape out of the back of the absorber. Lyα photons would only be detectable from an annulus around the DLA where the optical depth is approximately unity. However if DLA clouds are sufficiently inhomogeneous on scales much smaller in extent than the seeing disk, the hole may not be seen as Lyα photons could travel between the densest regions.

The velocity offset of the emission line relative to the DLA for Q0151+048 provides an additional clue to the spatial arrangement of the three objects qA, qB, and S4. The emission line detected for S4 is offset by $\sim$ 300 km s^{-1} to the blue of the DLA redshift (Møller et al. 1998). In the case of Q2059–360 the emission line lies 490 km s^{-1} to the red of the DLA redshift (Leibundgut & Robertson 1998). One possible explanation of those velocity differences is that they are a consequence of photoionisation by the quasar. The radiation pressure of the resonantly scattered Lyα photons would cause the HII skin of the DLA to expand away from the HI in the direction of the quasar (Williams 1972, Urbaniak & Wolfe 1981). This would provide an explanation of why the emission line for Q2059–360 is redshifted relative to the DLA. In this case some of the Lyα photons, produced on the far side, are able to penetrate the cloud because of the reduced optical depth in the red wing of the damped absorption line. Those photons would be observed as a redshifted emission line. For Q0151+048 the blueshift of the emission line would imply that qB is the source of ionising photons and must lie on the near side of the DLA.

The above arguments are far from conclusive, but the picture that qB is the source of ionising photons is at least plausible. We can make this statement more quantitative by computing how near qB must lie in order to explain the flux observed. To do this we follow

the analysis presented by Warren & Møller (1996, their equations nos 1 and 2). Consider a disk of HI of large optical depth, at distance d from a quasar of absolute magnitude M_B, and with normal inclined at angle ϕ to the line from the quasar to the cloud. The surface brightness of the cloud over the region of high optical depth is given by:

$$\Sigma_{Ly\alpha} = 3.66 \times 10^{-22} \frac{10^{-0.4M_B}}{d^2} \frac{cos\phi}{\alpha} (\frac{912}{4400})^{\alpha}$$
$$\mathrm{erg\,s^{-1}cm^{-2}arcsec^{-2}}$$

where α is the quasar continuum slope in the power-law representation $f_\nu \propto \nu^{-\alpha}$, and d is in kpc. Therefore the distance of the quasar is given by

$$d = \sqrt{3.66 \times 10^{-22} \frac{10^{-0.4M_B}}{\Sigma_{Ly\alpha}} \frac{cos\phi}{\alpha} (\frac{912}{4400})^{\alpha} \quad \mathrm{kpc}}$$

We set $\Sigma_{Ly\alpha}$ equal to the peak surface brightness for the model fit to S4 (Sect. 4.3) $\Sigma_{Ly\alpha} = 3.3 \times 10^{-16}$ erg s^{-1} cm^{-2} arcsec^{-2} i.e. where the surface brightness peaks the optical depth of HI visible to the quasar is assumed to be very high, and the drop off in surface brightness from the peak corresponds to a decline in column density. The absolute magnitude for the quasar is computed from the apparent magnitude $I(AB) = 20.87$, Table 3. The upper limit to the distance of qB from the cloud is then obtained by setting $cos\phi = 1.0$. For values of $\alpha = 0.7$ and 1.0 we find $d < 20\mathrm{h}^{-1}$ kpc and $< 14\mathrm{h}^{-1}$ kpc, respectively, for $q_0 = 0.5$. For $q_0 = 0.0$ the values are $d < 32\mathrm{h}^{-1}$ kpc and $< 23\mathrm{h}^{-1}$ kpc. These values are all the more plausible since they are larger than, but similar to, the projected distance from qB to the DLA, 12h^{-1}kpc and 19h^{-1}kpc, for $q_0 = 0.5$ and $q_0 = 0.0$ respectively. This means that the Lyα emission can be explained by photoionisation by qB without having to invoke an unlikely geometry. For example for $q_0 = 0.5$, setting $cos\phi = 0.7$, $\alpha = 1.0$, leads to $d = 14.5\mathrm{h}^{-1}$ kpc, which corresponds to an angle $\theta = 30°$ between the line joining qB to the DLA and the plane of the sky. The boundary of detectable Lyα emission corresponds to the point where the optical depth in HI becomes small. In other words the quasar is highlighting a Lyman-limit system. The size of the DLA contained would be smaller.

For completeness we consider the possibility that the photoionisation model is not correct and that the Lyα emission is due to star formation. Using the Kennicutt (1983) prescription SFR = L(Hα)/1.12 x 10^{41} erg s^{-1} and assuming L(Lyα)/L(Hα)=10 and negligible dust extinction leads to

$$SFR = 11(26)h^{-2}M_{\odot}\ yr^{-1}\ q_0 = 0.5(0.0)$$

However, with this SFR we would expect S4 to have a U-band magnitude of the order u(AB)=21 from the continuum (assuming SFR = $L_{1500}/(1.6 \times 10^{40} erg\ s^{-1}\text{Å}^{-1})$), which is not seen. Hence, star formation within S4 is very unlikely to be the source of the ioninising photons.

4.4.2 The relation between DLAs and Lyman-break galaxies

At high redshift $z \sim 3$ the comoving mass density in neutral gas in the DLAs is similar to the mass density in stars today. In addition the global star formation rate in the DLAs at high redshift predicted from the rate of decline of the cosmic density of HI (Pei and Fall 1995) is in reasonable agreement with the measured global SFR in the Lyman break galaxies (Madau et al. 1996), given the uncertainties in the two estimates. It is natural therefore to consider the connection between the two populations, DLAs and LBGs. To address this issue we will make the assumption that every LBG is surrounded by a DLA disk and ask whether it is then possible to reproduce the measured properties of the high-z DLA population.

A summary of the status of the search for LBGs was given by Dickinson (1999). Fig. 9 in Dickinson (1999) provides the current best estimate of the luminosity function (LF) of galaxies at $z \approx 3$, for $q_0 = 0.5$. This estimate is quite uncertain for two reasons. Firstly it not yet clear how complete the LBG samples are, i.e. how many high-redshift galaxies fall outside their colour selection criteria. Secondly the faint-end slope of the LF, i.e. α in the Schechter parameterisation, is not well determined, relying as it does on the relatively small number of faint LBGs found in the Hubble Deep Field. Because of the small field of view of the HDF, and the possibility of normalisation errors due to clustering, Dickinson (1999) rescaled the HDF numbers to tie smoothly on to the (well-determined) numbers at brighter magnitudes. For the present we will assume that the Schechter fit to the LF present by Dickinson (1999) is an adequate representation of the LF of LBGs.

Imagine now that every LBG lies at the centre of a DLA disk. To relate the LBG LF to observables of the DLA population we will suppose that the size of the DLA disk R_{gas} (i.e. the radius beyond which the column density falls below 2 x 10^{20} cm^{-2}) is related to the galaxy luminosity by a power-law relation of Holmberg form $R_{gas}/R^*_{gas} = (L/L^*)^t$. The value of R^*_{gas} is fixed so as to reproduce the observed line density of DLAs dn/dz, i.e. the average number of DLAs per unit redshift along a line of sight to a quasar. For randomly inclined disks the relation between dn/dz and R^*_{gas} is (Wolfe et al. 1986, eqn nos 7, 8):

$$\frac{dn}{dz} = \frac{\pi}{2}\frac{c}{H}\Gamma(1+2t+\alpha)\phi^*(1+z)^{1/2}R^{*2}_{gas} \quad (q_0 = 0.5)$$

where Γ is the gamma function. For randomly inclined disks of radius R the average impact parameter is $\bar{b} = 0.524R$. Therefore

$$\bar{b}^* = 0.524\sqrt{\frac{dn}{dz}\frac{2H}{\pi c\Gamma(1+2t+\alpha)\phi^*(1+z)^{1/2}}} \quad (q_0 = 0.5)$$

At $z = 3$ $dn/dz = 0.27$ (Wolfe et al. 1995). Together with the Holmberg relation this provides the expected average impact parameter as a function of apparent magnitude, at $z = 3$, and the expected apparent magnitude distribution of a sample of DLAs selected by

gas cross section. Using Dickinson's LF these results are plotted in Fig. 4.6, for different values of the parameter t.

When using the predictions presented in Fig. 4.6 it is important to remember that both the normalization and faint end extrapolation of the LBG LF are at present poorly known. Also dn/dz for DLAs could be wrong by a significant factor, in case systematic effects due to lensing and/or dust obscuration by the DLAs are biasing the number counts. Nevertheless it is instructive to compare the predicted curves in Fig. 4.6 to the few detections currently available and in Fig. 4.6 we therefore also show the apparent magnitudes and impact parameters of the three confirmed DLA galaxies, and a single DLA galaxy candidate, from which continuum emission has been detected. Apparent magnitudes of the four objects have been transformed to $z = 3$ to enable comparison with the $z = 3$ LBG luminosity function.

We now compare properties of the known DLA galaxies against the predictions, to draw preliminary conclusions about the parameter t. It should be noted firstly that faint DLAs with small impact parameters would be very difficult to detect, so that the region $m_R > 26$ and $\bar{b} < 4\mathrm{h}^{-1}$ is so far largely unexplored. On the other hand DLAs brighter than $m_R = 25$ at impact parameters $\bar{b} > 10\mathrm{h}^{-1}$ kpc would be detectable from the ground. If $t = 1.0$ most of the LBG counterparts to DLAs would lie in this region, but the few actual detections are fainter and have small impact parameters. Therefore large values of t are not compatible with the observations.

For nearby spirals a value of $t \sim 0.4$ is measured (Wolfe et al. 1986). However, if the measured impact parameters of the few high-redshift DLAs detected are representative of the fraction of DLAs brighter than $m_R = 26$, a lower value of $t \sim 0.25$ is indicated. Referring now to the lower diagram of Fig. 4.6, this would have the consequence that $\approx 70\%$ of the LBG galaxy counterparts to DLAs at $z \approx 3$ are fainter than $m_R = 28$. This conclusion is in fact relatively insensitive to the (poorly-determined) faint-end slope of the LBG LF. For example if the actual value is either flatter or steeper than Dickinson's measured value, the curves in the upper part of Fig. 4.6 are different, and the value of t that passes through the data points is different. Nevertheless the corresponding curve in the lower plot for that value of t is quite similar to the lower curve shown.

In the nearby universe a sample of galaxies selected by gas cross section has a luminosity distribution peaked near $L*$. The reason why this is probably not the case at high-redshift can be seen as follows. For a Schechter representation of the luminosity function the average luminosity of a sample of galaxies selected by gas cross section is $\bar{L} = L^*\Gamma(2+\alpha+2t)/\Gamma(1+\alpha+2t)$. Locally the canonical numbers for spirals are $\alpha = -1.25$ and $t = 0.4$ (Lanzetta et al. 1991), yielding $\bar{L}(0) = 0.55L^*(0)$. At high redshift taking $\alpha = -1.38$ and $t = 0.25$ gives a much fainter average luminosity $\bar{L}(z) = 0.1L^*(z)$. This is a consequence of the fact that at high redshift the faint end slope of the luminosity distribution $\alpha + 2t$ is closer to the critical value -1.0, which corresponds to zero average luminosity.

Acknowledgments

Nordic Optical Telescope is operated on the island of La Palma jointly by Denmark, Finland, Iceland, Norway, and Sweden, in the Spanish Observatorio del Roque de los Muchachos of the Instituto de Astrofisica de Canarias.

J.U.F. wishes to thank B. Thomsen for many helpful discussions during preparation for the observing run and is grateful to E. Bertin for guidance in the use of SExtractor. J.U.F. and S.J.W. gratefully acknowledge support from the STScI and ESO visitors programmes, respectively. We thank our referee, Bruno Leibundgut, for many valuable comments which helped us clarify several points in the manuscript.

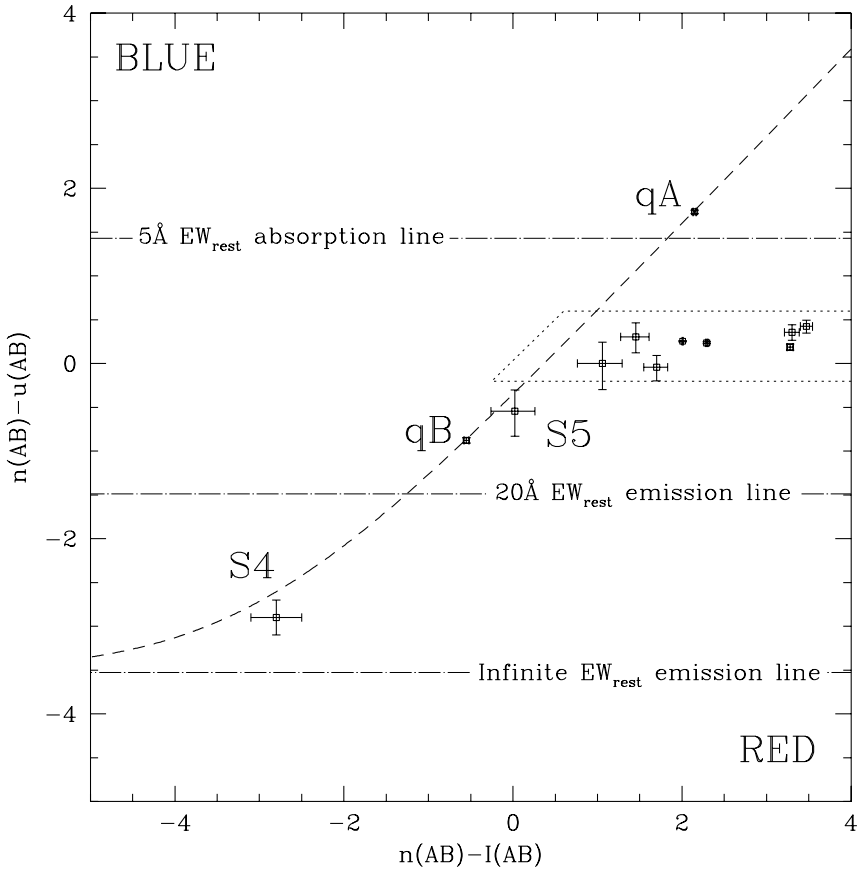

Figure 4.5: Two-colour diagram $n(AB) - u(AB)$ *versus* $n(AB) - I(AB)$ for the 11 detected objects with signal–to–noise ratio in the narrow–band frame > 4. The dashed line is a line of constant $u - I$ in the continuum indicating that the two quasars have very similar $u - I$ continuum colours but very different Lyα line equivalent widths (EWs). The dotted lines confine the expected region of objects with no special features in the narrow filter. The horizontal lines are lines of constant rest-frame EW=20Å for an emission line at $z = 1.93$ (lower) and rest-frame EW=5Å for an absorption line (upper) that lies in the narrow–band filter.

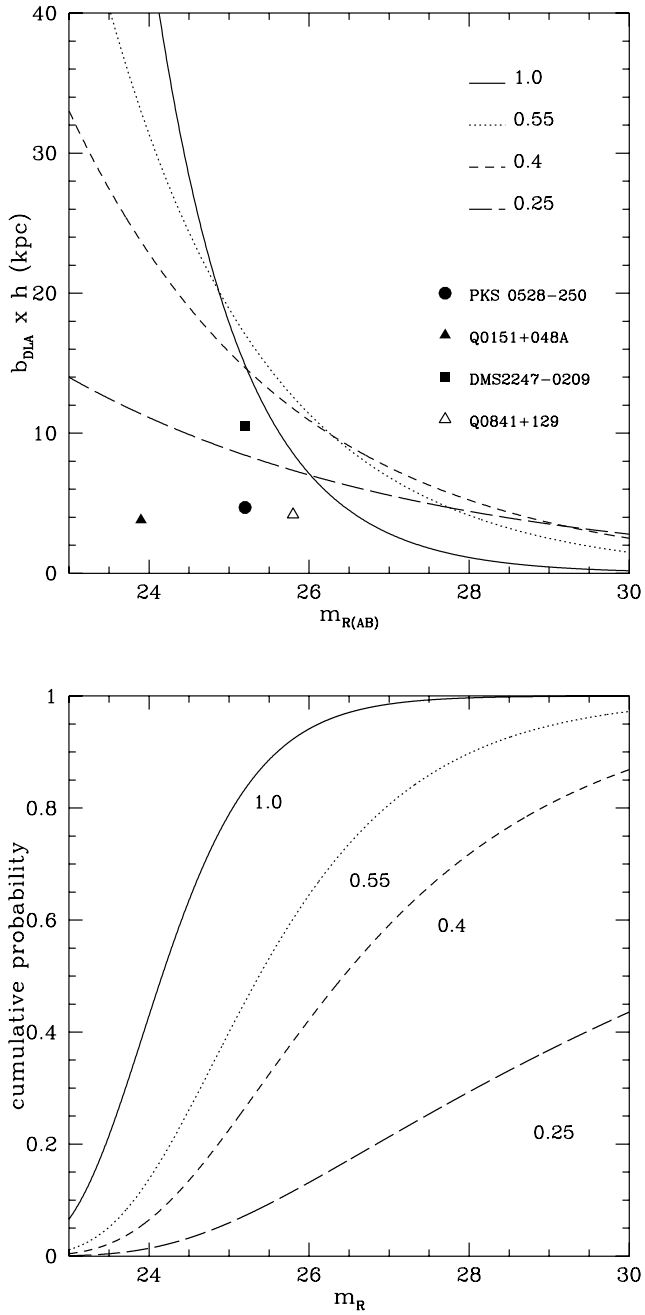

Figure 4.6: Predicted properties of the DLA population at $z = 3$ if DLAs are gaseous disks surrounding Lyman-break galaxies. *Upper:* the curves show predicted values of the mean impact parameter from the LBG to the line of sight to the quasar for different values of the Holmberg parameter t, as a function of apparent magnitude. The points are measured impact parameters for the three known DLA galaxies (and one likely candidate) for which the continuum magnitude of the galaxy has been measured. *Lower:* the curves show the predicted cumulative probability distribution for the apparent magnitudes of the LBG counterparts to the DLAs

Chapter 5

The sources of extended continuum emission towards Q0151+048A : The host galaxy and the Damped Lyα Absorber

Fynbo J.U., Ingunn B., Møller P., 1999, A&A, submitted

5.1 Introduction

The study of the galaxy population at high redshifts has progressed rapidly during the last decade. Through the Lyman-break technique hundreds of normal (i.e. not dominated by active galactic nuclei), star forming galaxies at z=2–4 have been detected and studied with imaging as well as spectroscopy (Steidel et al. 1996b). These so called Lyman-Break Galaxies (LBGs) have star formation rates (SFRs) in the range 4–55h^{-2} M$_\odot$ yr^{-1} for Ω=1.0 or 20 – 270 M$_\odot$ yr^{-1} for Ω=0.2 (Pettini et al. 1998). Also, via the study of the class of high column density QSO absorption lines systems known as Damped Lyα Absorbers (DLAs) a wealth of information on the early chemical evolution of galaxies at z=2–4 has been obtained (e.g. Lu et al. 1996). The DLAs are in general forming stars at a significantly lower rate than the LBGs (Møller & Warren 1998, Fynbo et al. 1999a).

Independent information about the formation of the brightest galaxies comes from detailed studies of the stellar populations of present day bright cluster ellipticals. These populations seems to have formed early (z>2) in strong burst of star formation (Bower et al. 1992). Studies of the fundamental plane for elliptical and lenticular galaxies in rich clusters at intermediate redshifts also indicate early formation times (z>5 for Ω=1, Jørgensen et al. 1999), and the fundamental plane for field ellipticals at similar redshifts is consistent with being the same as in clusters (Treu et al. 1999a). Studies of the globular cluster populations of faint elliptical galaxies also indicate rather early formation times (z>1), whereas for bright cluster ellipticals the globular cluster populations do not strongly constrain the possible formation scenarios (Kissler-Patig et al. 1998). Furthermore, the presence of seemingly old stellar populations in elliptical galaxies at z>1 proves that at least some elliptical galaxies formed very early in strong bursts of star formation (Spinrad et al. 1997, Treu et al. 1999b, see also Jimenez et al. 1999). For first-rank ellipticals star formation rates as high as SFR$\sim$10^3 M$_\odot$ yr^{-1} would then be possible. A reason why such high star formation rates have not been detected in galaxies at high redshift may be that these galaxies are the hosts of powerful QSOs and hence are hidden by the light from the QSOs (e.g. Terlevich & Boyle 1993). Support for a connection between QSOs and bright elliptical galaxies comes from the fact that radio quiet QSOs as well as radio loud QSOs and radio galaxies at z=0.1-0.3 are hosted by galaxies for which the light profiles are best fit by de Vaucouleurs profiles indicating that they are early stages of massive ellipticals (McLure et al. 1999). There is increasing evidence that QSOs at redshifts z$\approx$2 are embedded in extended emission that is consistent with the presence of a stellar population in the QSO host galaxies. In the case of radio loud QSOs host galaxies have been detected in the optical and infrared by Lehnert et al. (1992) and Carballo et al. (1998), and in the case of radio quiet QSOs host galaxies have been detected in the optical and near infrared by Aretxaga et al. (1998a, 1998b). There does not seem to be any systematic differences between the host galaxies of radio loud and radio quiet QSOs. Both populations of host galaxies are extremely bright, R$\approx$21–22, and have optical-

Table 5.1: Observations of Q0151+048, Sept 17 – 20 and Oct 17 – 18, 1998

Filter	Combined seeing (arcsec)	Total integration (sec)
U	0.96	12500
B	0.84	24300
I	0.67	11750

to-infrared colours in the range R-K≈3–5. However, measured polarisation of the light from some radio galaxies show that scattered QSO light can also contribute significantly to the observed extended emission (e.g. Cimatti et al. 1998).

In 1996 we performed a narrow band study of the $z_{abs} \approx z_{em}$ Damped Lyα Absorber (DLA, Wolfe et al. 1986) towards Q0151+048A using the 2.56-m Nordic Optical Telescope (NOT) (Fynbo et al. 1999a). The main result of this study was the detection of extended Lyα emission from the DLA. The Lyα emission line had prior to this been detected in a spectroscopic study of Q0151+048A (Møller et al. 1998), but the large extended nature of the DLA absorber was quite unexpected. U band data, also from the 1996 run, hinted at the existence of an extended broad band object, but the signal–to–noise ratio of the object was low. We have therefore obtained deeper imaging of Q0151+048 in broad band U, B and I filters in order to confirm or reject our tentative detection, and to measure the extend and luminosity of the broad band source if real.

In Section 2 below we describe our new observations. In Section 3 we describe in detail the two independent methods we have used to search for extended objects close to the quasar. First we describe the image-deconvolution, where we used the Magain, Courbin & Sohy (1998, hereafter MCS) algorithm, secondly we describe the direct PSF subtraction, and Section 4 we discuss our results.

In this paper we adopt H=100 h km s^{-1} Mpc^{-1}, Ω_m=1.0 and Ω_Λ=0 unless otherwise stated.

5.2 Observations and Data Reduction

The observations were performed during two observing runs in September and October 1998 with HiRAC (High Resolution Adaptive Camera) on the 2.56 m Nordic Optical Telescope. The CCD used was a 2048^2 back-side illuminated thinned Loral with a pixel size of 0.1082 arcsec.

All 6 nights during which the observations were performed were photometric and with good seeing (median 0.7 arcsec FWHM in the I–band). Integration times in U were 1000-

1500 sec in order to avoid the total noise to be dominated by readout noise. In I and B the integration times were 250-300 sec and 300-500 sec respectively. Between exposures the telescope was moved 2-4 arcsec to minimize the effects of bad pixels and fringing. The total integration times in each filter are given in Table 5.1.

Also observed were several standard star sequences from Landolt (1992) and photometric solutions were obtained for each filter. For counts given as electrons per second we derive zero-points in the Landolt system of 22.77, 25.13 and 24.48 for u, B and I respectively. All magnitudes subsequently quoted in this paper are on the AB system. For the U–band we determined the colour equation $u = U + 0.17(U - B)$ relating the instrumental magnitude u to the standard Johnson U. There was substantial scatter around the fit near $U - B = 0$ of ~ 0.05 mag., which is typical for this band (e.g. Bessell 1990). The instrumental magnitudes u were converted to AB magnitudes using the equation $u(AB) = u + 0.58$, determined by integrating the spectrum of the star GD71 over the passband. Here we have retained the lower case u for the AB magnitude indicating that the effective wavelength of the filter lies significantly away from the standard value. The colour term for the I and B filters are consistent with zero i.e. $i = I$ and $b = B$, and we used the equations $I(AB) = I + 0.43$ and $B(AB) = B - 0.14$ (Fukugita et al. 1995) to put the I and B magnitudes onto the AB system.

The data were bias-subtracted, and twilight sky frames were used to flatten the frames in the standard way.

For the deconvolution, the individual bias subtracted and flattened I–band images were divided into six groups (chronologically) and the frames of each group were then combined using the optimal combination code described by Møller & Warren (1993), which maximizes the signal–to–noise ratio for faint sources. These six combined images were used in the simultaneous deconvolution process (see sect. 5.3.1 below). Furthermore, all the individual I–band images were combined into one combined image, which was used in the PSF subtraction described in sect. 5.3.2. In the same way we divided the individual bias subtracted and flattened B–band frames in four groups and calculated combined images for each group and for all images. Finally we combined the ten individual bias subtracted and flattened U–band frames into one combined image. The details of the sky noise in the combined images are provided in Table 5.2.

Table 5.2: Measured sky level and rms of sky surface brightness.

passband	sky level	rms SB
	mag. arcsec^{-2}	mag. arcsec^{-2}
I(AB)	19.4	27.3
B(AB)	22.1	28.8
u(AB)	22.2	27.6

5.3 Analysis

5.3.1 Deconvolution

The deconvolution method

The images were deconvolved using the MCS algorithm. This method is based on the principle that the resolution of a deconvolved image must be compatible with its sampling, which is limited by the Nyquist frequency. The deconvolved image is decomposed into a sum of deconvolved point–sources plus a background smoothed on the length scale of the final resolution. The intensities and positions of the point–sources as well as an image of the more extended objects are given as output of the deconvolution procedure. Image decomposition allows objects blended with or even superposed on point–sources to be studied in some detail.

In order to check if the deconvolved model is compatible with the data, a residual map is computed. The residual map contains in each pixel the χ^2 of the fit of the model image (re–convolved with the PSF) to the original data of that pixel. The χ^2 image is used to determine the appropriate weight attributed to the smoothing of the image of extended sources in order to avoid under- or over-fitting of the data (see MCS for further details). A deconvolution compatible with the data should show a flat residual map with a mean value of 1 all over the image.

The MCS algorithm makes it possible to simultaneously deconvolve several frames. The advantage of this process is to derive the optimally constrained deconvolved frame which is simultaneously compatible with several different images of a given object. This results in a more accurate decomposition of the data than the deconvolution of one single combined frame. Moreover, applying the algorithm to many dithered frames leads to a deconvolved image with an improved sampling.

Application to the data

Simultaneous deconvolution of the U–band data from 1996 had already strongly indicated extended broad band emission in the direction of Q0151+048A (see Fig. 5.1). However, although the shape of the extended emission was similar to the one found in narrow-band

(Fynbo et al. 1999a), it was unclear to which extent systematic errors in the determination of the PSF influenced the detection and hence the signal-to-noise ratio of the object was too uncertain to constrain its morphology and luminosity.

There are two bright stars in the field of Q0151+048, referred to as psfA and psfB (see Fynbo et al. 1999a). However, our new deep I–band data revealed that psfB has a faint red companion star at a projected distance of $0\farcs7$. In the I–band it is 4.3 magnitude fainter than psfB, in the B–band it is 6.3 magnitudes fainter than psfB, and in the U–band it remains undetected. In the following we only use psfA for the determination of the PSF.

We adopted for the deconvolved image a pixel size of $0\farcs0541$ (half of the original one), and a final resolution of 3 pixels FWHM, or $0\farcs16$ (the Nyquist limit is 2 pixels FWHM).

Results

Fig. 5.2 shows the deconvolved images in all three bands I, B and U. The images show the five sources already known to be in the field, namely the three point–sources qA, qB and the star s, and the two faint galaxies gA and gB south west of qA (see Fynbo et al. 1999a for details). However, there is also significant extended emission under the point–source emission from qA in all three bands. This emission have nearly identical morphology in the I and B bands with contours centred on the position of qA and with a slight elongation with position angle $\sim 20^o$ east of north. The shape and intensity of the extended U–band emission under qA (Fig. 5.2 right panel) is consistent with the shape and intensity derived from the 1996 U–band data (Fig. 5.1). Since the two sets of U–band data have been obtained with two different instruments, the consistency between the two measurements makes strong systematic errors unlikely. The morphology of the U–band emission is significantly more extended than the B and I morphology, about 4.5×2.2 arcsec^2, and has a position angle of about 100° east of north. This is very similar to that of the Lyα source S4, which extends over 6×3 arcsec^2 with position angle 98° east of north.

The extended emission towards qA is $\sim$4 magnitudes fainter than that of the point–source emission. This high contrast makes it difficult to determine the exact ratio between the luminosity of the extended source ($L_{\rm Ext}$) and that of qA ($L_{\rm QSO}$). Several deconvolution solutions with different luminosity $L_{\rm QSO}/L_{\rm Ext}$ ratios are compatible with the residual map constructed as described above. Thus, there is some degeneracy between the plausible solutions found by the algorithm.

In order to demarcate the range of plausible solutions, a grid of 15 deconvolved images in each band was calculated, representing 5 different luminosity ratios $L_{\rm QSO}/L_{\rm Ext}$ and with 3 different values of the Lagrangian smoothing parameter applied during the deconvolution (see MCS for a description of the Lagrangian smoothing parameter). The solutions with the highest $L_{\rm QSO}/L_{\rm Ext}$ ratios were unphysical since they have a ring-shaped morphology, i.e. a hole at the position of the QSO. The lowest values of $L_{\rm QSO}/L_{\rm Ext}$ were rejected by

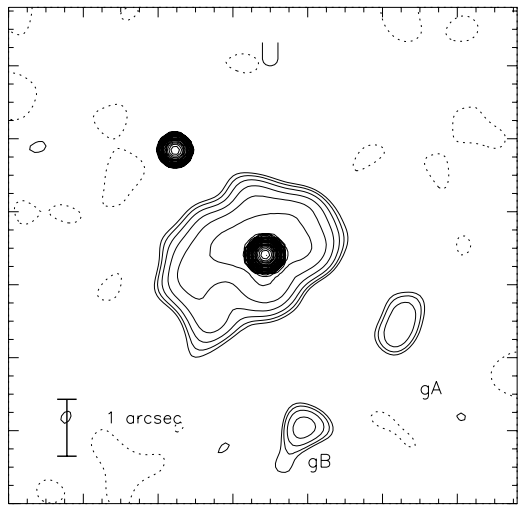

Figure 5.1: Contours of the deconvolved U–band from 1996. The resolution is 0.″35 and the axis are in units of arcsec. The contour levels are -9, -6, -3, 3 × 1σ of the sky noise and thereafter spaced logarithmically in factors of 1.5, with the dotted contours being negative. The field is 12×12 arcsec^2, North is up and East to the left.

inspection of the residual map mentioned above. The resulting range of magnitudes for the extended emission is given in Table 5.3. The solutions shown in Fig.2 are those with the highest acceptable values of $L_{\rm QSO}/L_{\rm Ext}$. Our conclusions concerning the morphology of the extended emission in the three bands are, however, unchanged for all solutions within the acceptable range.

In the B-band there is also significant extended emission under the PSF of the fainter neighbour quasar qB.

5.3.2 Object based image decomposition

In conclusion of the previous section: *i)* There is clear evidence for extended broad band (U, B and I) emission in the vicinity of the quasars Q0151+048A,B; *ii)* the morphology of the extended object(s) is identical in B and I but significantly different in U; *iii)* the U–band morphology is more extended and similar to the morphology of the Lyα emission from the DLA absorbing galaxy (S4).

Those conclusions would suggest that the extended emission in this field is made up of three individual components: The DLA absorbing galaxy, the host galaxy of qA and the host galaxy of qB. The different morphology in the four different bands would then indicate that the objects have different spectral energy distributions (SEDs).

In order to investigate this further we decomposed the superimposed images into individual objects with different SEDs. For this image decomposition we applied the same

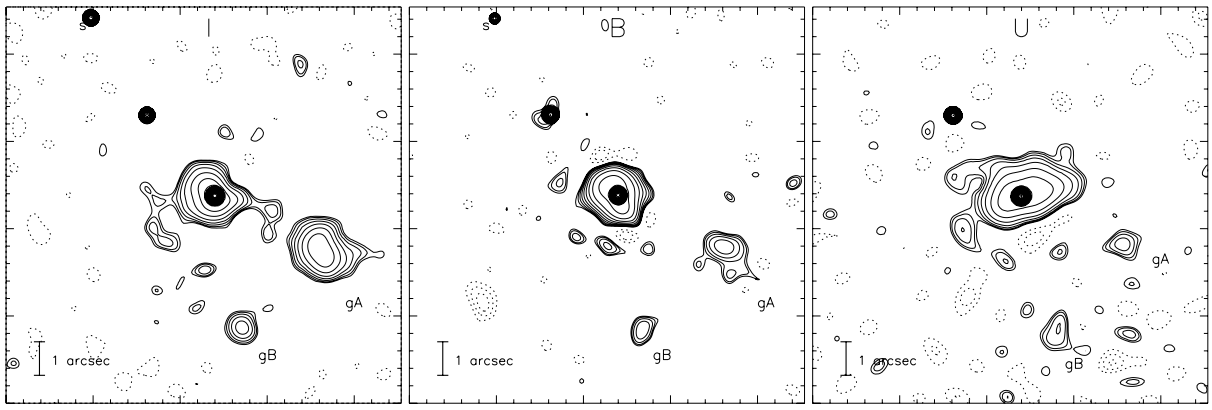

Figure 5.2: Contour plots of 12×12 arcsec^2 surrounding the two QSOs from the deconvolved I–band frame (*left)*, B–band frame *(middle)* and U–band frame *(right)*. The three point–sources s, qB and qA are seen on the diagonal from the upper left corner (s) to the centre (qA). The resolution is 0.″16. North is up and east to the left. Seen is the extended emission under qA and the two galaxies gA and gB south of qA.

procedure we used for the narrow band image analysis (Fynbo et al. 1999a), but here we add more components. We consider point–sources, de Vaucouleurs profiles and exponential profiles. The best decomposition is determined as the minimum χ^2 fit following an iterative procedure as described below.

B–band data

The B–band image is more than a magnitude deeper than the I and U–band images in terms of the background rms surface brightness. Our first step was therefore to produce optimized models of the galaxies from the B–band data. For the decomposition we considered the following 8 components: Three point–sources (qA, qB, s), four galaxies to be fitted (gA, gB and the host galaxies of qA and qB, in what follows named HGa and HGb), and one galaxy of "frozen" morphology (the DLA absorbing galaxy S4). For S4 we adopted the model determined from the narrow–band data (Fynbo et al. 1999a). Note that most of the objects do not overlap significantly, thus allowing us to fit them independently.

The bright star psfA was used with DAOPHOT II (Stetson 1997) to define the PSF. We then employed the iterative χ^2 minimization procedure deatiled in Fynbo et al. 1999a, to decompose the image of qA into a point–source and a de Vaucouleurs galaxy model (convolved with the PSF). For the calculation of the χ^2 we excluded a circular region of radius 0.65 arcsec centred on qA due to the large PSF-subtraction residuals. After ten iterations a stable solution was found. The same procedure repeated with an exponential-disc profile instead of the de Vaucouleurs profile resulted in a much poorer fit. A significant positive residual, centred about 1 arcsec east of qA, was left after this procedure. The most

Table 5.3: Photometry of qA, qB and the extended sources under qA and qB (listed as ExtA and ExtB). The magnitudes given for ExtA are measured in a circular aperture with diameter 3.5 arcsec. The magnitudes for S4 and HGa under PSF-subtraction are determined by model fits as described in the text. The upper limits to the magnitudes of HGb are 2σ. The magnitudes of gA and gB are measured in a circular aperture with diameter 1.35 arcsec.)

	u(AB)	B(AB)	I(AB)
Deconvolution			
qA	17.81±0.02	17.83±0.02	17.46±0.02
qB	21.00±0.02	21.18±0.02	20.69±0.02
gA	23.85±0.09	23.15±0.02	21.77±0.02
gB	24.02±0.09	24.06±0.02	23.18±0.03
ExtA	21.8 – 21.3	21.3 – 20.7	21.8 – 21.2
NOT96			
ExtA	21.8±0.2	-	-
gA	24.08±0.06	-	21.87±0.03
gB	24.18±0.07	-	23.33±0.05
PSF-subtraction			
HGa	21.7±0.2	20.8±0.2	21.5±0.2
HGb	>26.0	25.00±0.10	>25.7
S4	23.9±0.3	24.1±0.3	23.7±0.3
gA	24.27±0.12	23.51±0.03	22.10±0.03
gB	24.28±0.12	24.53±0.06	23.82±0.09

plausible interpretation of the residual is that it originates from the DLA absorbing galaxy S4. As S4 is known to extend across the position of the bright quasar, measuring its flux from a direct aperture measurement is impossible because of the large PSF subtraction residuals. Instead we made a grid of models to determine the flux of S4 via minimum χ^2 fitting. For a given assumed B magnitude of S4 we first subtracted the correctly scaled exponential–disc model as determined from the original Lyα image (Fynbo et al. 1999a). For that given B magnitude of S4 we then repeated the iterative fitting of a de Vaucouleurs profile to the remaining flux. The final model was chosen to be the model with the smallest χ^2 measured in an area excluding pixels less than 0.65 arcsec from qA. The improvement in the fit due to the inclusion of the S4 model was significant ($\Delta\chi^2$ = -21). We also fitted the profiles of the two galaxies gA and gB. For gA the best fit was obtained with an exponential-disc profile, whereas the best fit for gB was obtained with a de Vaucouleurs profile.

Fig. 5.3b shows a 14x14 arcsec^2 field of the area after subtraction of the qA and qB PSFs

as determined from the minimum χ^2 fit. The residuals, after the additional subtraction of the final models for HGa, gA and gB can be seen directly below (Fig. 5.3e). The magnitude of HGb was measured on this final subtracted image.

U and I band data

The well constrained galaxy models determined from the high signal–to–noise B image were subsequently used to decompose the U and I–band data. Since the combined seeing of the U–band data was poorer than that of the B image, we first smoothed the galaxy models to the seeing of the U–band data. For a large grid of U–band magnitudes of S4 and HGa we then subtracted scaled versions of the smoothed S4 and HGa galaxy models, fitted and subtracted the quasar point source component using DAOPHOT II, and finally calculated the χ^2 in an area excluding pixels less than 0.8 arcsec from qA. The final model was selected to be that which had the smallest χ^2. The U magnitudes of the galaxies gA and gB were determined in the same way. For the decomposition of the combined I–band data, which have a better seeing than the B–band data, we first smoothed the I–band image to the seeing of the B image and then proceeded as for the U–band data.

Results of this procedure can be seen in Fig. 5.3a,d and Fig. 5.3c,f for the I and U–bands respectively. As for the B–band data the upper frames show the fields after subtraction of final fits of qA and qB only, while in the lower frames the fitted models of galaxies HGa, gA and gB have also been subtracted. The magnitudes (and estimated associated errors) of objects resulting from the fitting procedure are listed in Table 3.

5.4 Summary and discussion

Our original interest in the field of Q0151+048A was to identify the DLA galaxy in front of it. This identification was accomplished via imaging in Lyα (Fynbo et al. 1999a), but our broad band images left some questions open. The purpose of the deeper broad–band data presented in this paper was to clarify this situation. We shall here first summarise our findings, then briefly consider their implications.

5.4.1 Results summary

Our new data have unambiguously confirmed the presence of extended emission in the field in all three bands I, B and U. The different morphology seen in the three bands strongly suggest that we see three objects superimposed: The quasar, the DLA absorbing galaxy and the quasar host galaxy.

The superposition of three close objects of widely differing brightnesses causes considerable degeneracy for any attempt to determine the brightness of the faintest sources, and it

is therefore impossible to find a unique solution for the flux of the faintest object (the DLA galaxy S4). Nevertheless, we find that S4 is clearly detected in the U image. The U–band magnitude of S4 determined via our minimum χ^2 procedure is fully consistent (to within 1 σ) with being caused by the known Lyα flux at 3565Å alone. The data are therefore consistent with a zero contribution from any continuum source in the U–band.

It is difficult to determine the exact errors on the I and B magnitudes of S4, but for both images we found a very significant improvement in the reduced χ^2 of the fit when we included S4. It is therefore likely that S4 is indeed a low surface brightness continuum source, but this question is going to be extremely hard to settle.

The existence of a separate extended continuum source centred on qA is, however, clearly demonstrated independently in all bands. This result was arrived at independently via image deconvolution, and via our iterative object fitting technique.

5.4.2 Discussion: Starburst Galaxy or Dust scattering

The distance modulus (for z=1.93) in the assumed cosmology with h=0.5 is 45.8. Assuming instead Ω=0.3 and Ω_Λ =0.7 the corresponding distance modulus becomes 46.6. Hence, the absolute AB magnitudes of the host galaxy HGa is <-24.0(-24.8) in U (rest frame 1100–1300Å), <-24.5(-25.3) in B (rest frame 1300–1500Å) and <-24.0(-24.8) in I (rest frame 2300–3400Å). Such extremly bright magnitudes are in the local universe only connected with brightest cluster galaxies (for comparison M87 and Centaurus A both have absolute magnitudes of roughly -23 in the V–band). Brightest cluster members can be as bright as -26 (Oemler 1976). Interestingly we find that the absolute magnitude of HGa is similar to those of the extended 'fuzz' that have been detected around other high redshift QSOs by Lehnert et al. (1992), Carballo et al. (1998) and Aretxaga et al. (1998a, 1998b).

The morphology of the host galaxy HGa is best fit by a de Vaucouleurs profile. The fit to an exponential-disc leads to a much poorer fit. A plausible interpretation of the data is therefore that we see the early stage of a massive elliptical galaxy in the process of forming the bulk of its stars. Assuming that all the light is coming from stars, and not e.g. scattered quasar light (see below), we can estimate the star formation rate (SFR) needed to explain the observed fluxes. In the case of continuous star formation we can adopt the relation between the SFR and the luminosity at 1500Å SFR = $L_{1500}/(1.3 \times 10^{40} erg\, s^{-1} Å^{-1})$ commonly used for LBGs (Pettini et al. 1998) and we hence infer a star formation rate of order 100(200) $M_\odot$ yr^{-1} for Ω=1(0.3) and Ω_Λ=0(0.7). For instantaneous bursts we can use the Starburst99 package (Leitherer et al. 1999) to infer the colours of models calculated with solar metallicity and ages 1, 10, 20 and 100 million years. The colours for these three models are given in Table 5.4.

The colours of the host, 0<u-B<1.1, -1.1<B-I<0.1, are roughly consistent with an instantaneous burst with an age in the range 10–100 Myr. The number of stars formed in the

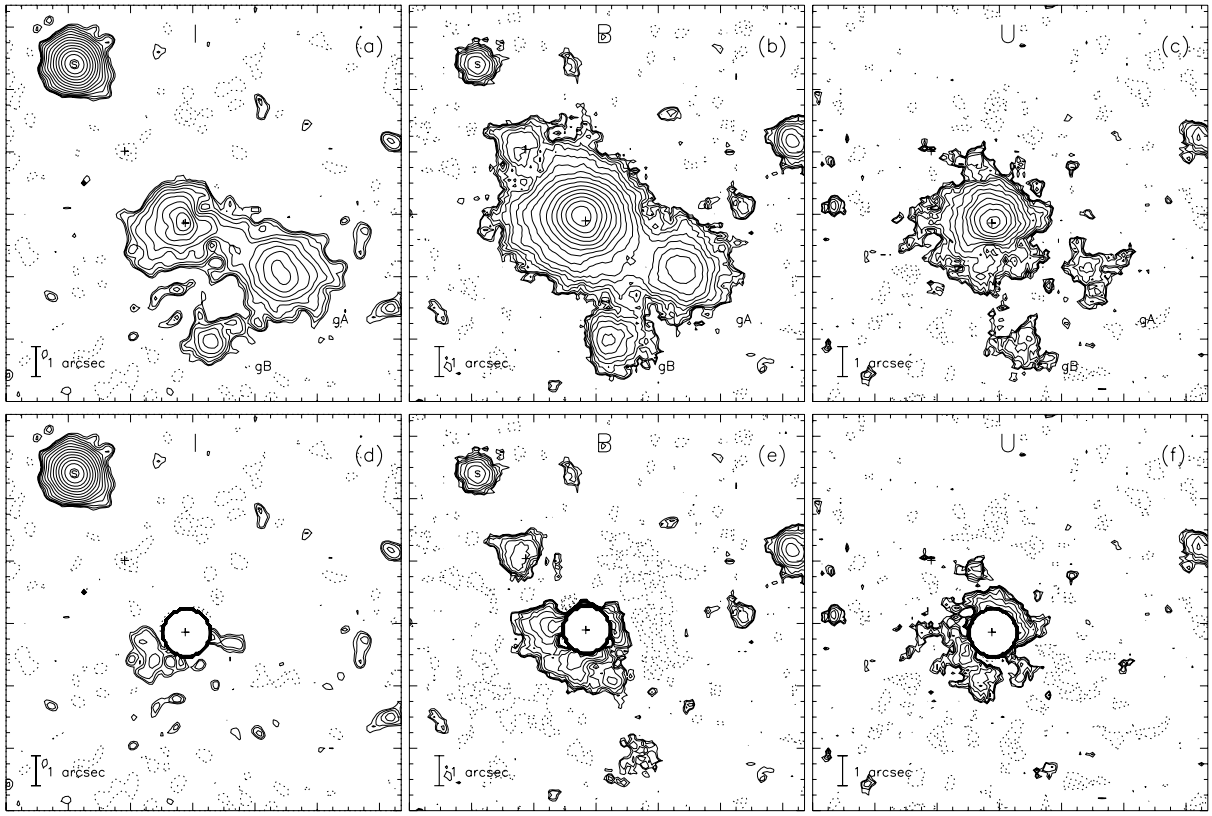

Figure 5.3: Contour plots of 14x14 arcsec^2 surrounding the two QSOs from the final combined and PSF subtracted frames in a) I–band, b) B–band and c) U–band. North is up and east to the left. Seen is residual extended emission under qA. Also seen are the two galaxies gA and gB south of qA. The contour levels are -9, -6, -3, 3 $\times$ 1σ of the sky noise and thereafter spaced logarithmically in factors of 1.5, with the dotted contours being negative. d) – f) show the same region after subtraction of the galaxy fits of HGa, gA and gB as described in the text.

The most plausible explanation for the residual east of the position of qA is the absorber galaxy S4.

Table 5.4: The colours of instantaneous starbursts with four different ages. The colours of HGa are listed for comparison.

Age (Myr)	u-B	B-I
1	-0.2	-0.7
10	-0.1	-0.3
20	0.1	-0.1
100	0.7	0.3
HGa	0.0–1.1	-1.1–0.1

burst would be in the range from 10^8 to a few times 10^9 stars depending on the age of the burst and on the assumed cosmology.

An equally plausible interpretation of the extended fuzz frequently seen around quasars, is light from the quasar itself scattered by dust. This mechanism is well known from radio galaxies at high reshifts where scattering off dust grains has revealed the existence of "hidden" quasars in the galaxy cores. It is likely that radio quiet QSOs have similar non–isotropic radiation fields (see e.g. the discussion in Møller & Kjærgaard 1992), and in that case our line of sight is such that we look straight down the emission cone inside of which the scattering is taking place. In this case we therefore expect to see the quasar emission cone "end on" via forward scattered quasar light. The scattering process is expected to be essentially grey and recent calculations predict that as much as 10% of the quasar light could be scattered in this way (Witt and Gordon, 1999; Városi and Dwek, 1999; Vernet et al. 1999). If considering a clumpy medium, we would expect dust scattered light to be emitted from inside a very large volume in front of the quasar. When taking the cone geometry into account one would expect its total flux to be roughly a few % of the quasar flux at any given wavelength (Fosbury, private communication). From Table 3 we find that the flux from HGa is 3, 6 and 2% of the flux from Q0151+048A in U, B and I respectively. Similar, but less significant, results are found for HGb. It is not yet knownn if the light profile of scattered light from a cone will reproduce a de Vaucouleurs profile, but since this seems to be a universally preferred profile it is not unlikely. One thing worth noting in Fig. 5.3e are the negative residuals surrounding the position of qA at a distance of 2-3 arcsec after subtraction of the fitted de Vaucouleurs profile. This indicates that the true profile of HGa in reality falls off steeper than a de Vaucouleurs profile. If model calculations were to show such a steep profile for forward scattered light in a radiation cone, that would be a strong hint towards the nature of the quasar fuzz.

Acknowledgments

We wish to thank Pierre Magain and Peter Stetson for making available the MCS-code and DAOHPOT-II respectively. We have benefitted from stimulating discussions with R. Fosbury and J. Vernet on the subject of dust scattering. JUF thanks the European Southern Observatory for support from the ESO studentship programme. IB thanks the European Southern Observatory for support from the ESO visitor programme.

Chapter 6

The Gas Reservoir for present day Galaxies : Damped Lyα Absorption Systems

Fynbo J.U., Thomsen B., Møller P., In : "Astrophysical Research and Science Education", Vatican Observatory Press, in press

6.1 Introduction

Damped Lyα Absorbers are the objects with highest HI column density of QSO absorption line systems. QSO absorption line systems are intergalactic material or in rare cases even galaxies that lie along the line of sight to background QSOs. In the spectrum of the background QSOs QSO absorption line systems manifest themselves primarily in thousands of Lyα absorption lines on the blue side of the QSO Lyα emission line - the so called Lyα forest. In a simplified picture each Lyα absorption line represents an intersecting intergalactic cloud. Lyα absorption lines at a wavelength close to the QSO Lyα emission line are caused by clouds near the QSO in physical space whereas Lyα absorption lines further towards the blue are less redshifted and hence caused by clouds closer to us along the line of sight (for a recent review see Rauch 1998).

Damped Lyα Absorbers (DLAs) are QSO absorption line systems causing damped Lyα absorption. To do that DLAs have neutral hydrogen column densities larger than $2 \times 10^{20} cm^{-2}$, which is comparable to the column density of baryons in normal disk galaxies at the present epoch. A very important result recently found is that most of the baryons that reside in stars in galaxies today, at high redshift were in cold gas in DLAs (Wolfe et al. 1995). In other words, DLAs constitute the gas reservoir out of which present day galaxies formed.

Since DLAs are objects found by the absorption they cause, much information has been collected about metallicity and dust content through the study of line strengths of metal lines associated with the DLAs allthough the interpretation of the data is still subject to debate (Lu et al. 1996, Kulkarni et al. 1997). Little, however, is known about the sizes and morphologies of the objects. One way to obtain this information is to detect emission from them.

From an observational point of view the main problems in studying emission from DLAs are *(i)* that they are very faint and *(ii)* the presence of a much brighter QSO at a distance of only 0-3 arcsec on the sky. At a redshift of $z = 2$ DLAs produce regions of 15-25Å (the width depending on the HI column density) of saturated absorption in the spectrum of the background QSOs. Hence imaging in a narrow filter with a width corresponding to the width of the damped absorption line will circumvent problem *(ii)*. If the DLA is a Lyα *emitter* it will be relatively easy to detect against the modest sky background in the narrow band filter which circumvents problem *(i)*. Narrow band imaging of DLAs have been pursued in more than a decade (e.g. Lowenthal et al. 1995), but only recently with success. The DLA at $z = 2.81$ towards PKS0528-250 (Møller & Warren 1993a 1998, Warren & Møller 1996) and the DLA at $z = 1.934$ towards Q0151+048A (Møller et al. 1998, Fynbo et al. 1998, 1999a) have been detected using the narrow filter technique. In the case of the DLA towards Q0151+048A we detected extended Lyα emission, which allowed us to obtain the rotation curve of the galaxy (Møller 2000).

In this paper we report on results from a new narrow band project aimed at the DLA at $z = 1.943$ towards PKS1157+014, and compare results for the DLAs with a sample of high redshift galaxies that are selected in a completely independent way - the Lyman-break galaxies.

6.2 Observations

PKS1157+014 was observed with the 2.56m Nordic Optical Telescope (NOT) March 28 - 31 1998. Two of the nights were lost to bad weather. We obtained a total integration time of 10 hours in narrow band, and 4000 sec in both I and U. The seeing ranged from 0.6 arcsec in I to 0.9 arcsec in the narrow band. Due to the two nights lost to bad weather we didn't reach the flux-limits we aimed at. With the data obtained we reach a 5σ flux limit of 7.5×10^{-17} erg s^{-1} cm^{-2} in the narrow band and 5σ limiting magnitudes of 25.9 and 25.3 in I(AB) and U(AB) respectively.

6.3 The field of PKS1157+014

Fig. 6.1 shows 96×24 arcsec^2 surrounding PKS1157+014 from the combined I-band, U-band and narrow filter frames. As seen the quasar is not present in the narrow band frame due to the strong absorption line. We do not see any significant Lyα emission at or near the position of the quasar from the DLA. We have obtained two more nights on NOT in March 1999, which will allow us to reach a 5σ detection limit of $5 \times 10^{-17} ergs^{-1}$ cm^{-2}, which is sufficiently deep to detect the DLAs we have seen in earlier projects. However, we do detect two candidate emission line galaxies marked by 'S' at signal-to-noise levels between 4 and 5 in the combined narrow-band frame. These very blue and compact emission line galaxies are very similar to the emission line galaxies associated to the DLAs seen in the fields of PKS0528-250 and Q0151+048. In both DLA-fields we have studied so far with narrow band imaging we have found one or more galaxy at the redshift of the DLA, indicating that also at high redshift galaxies were members of groups. It is interesting to note how the galaxies seem to be aligned. This is seen in most high redshift groups of Lyα emitting galaxies (see Fig. 6 in Møller & Warren 1998). This trend is in agreement with N-body simulations of hierarchical structure formation were galaxies predominantly form along filaments (e.g. Evrard et al. 1994).

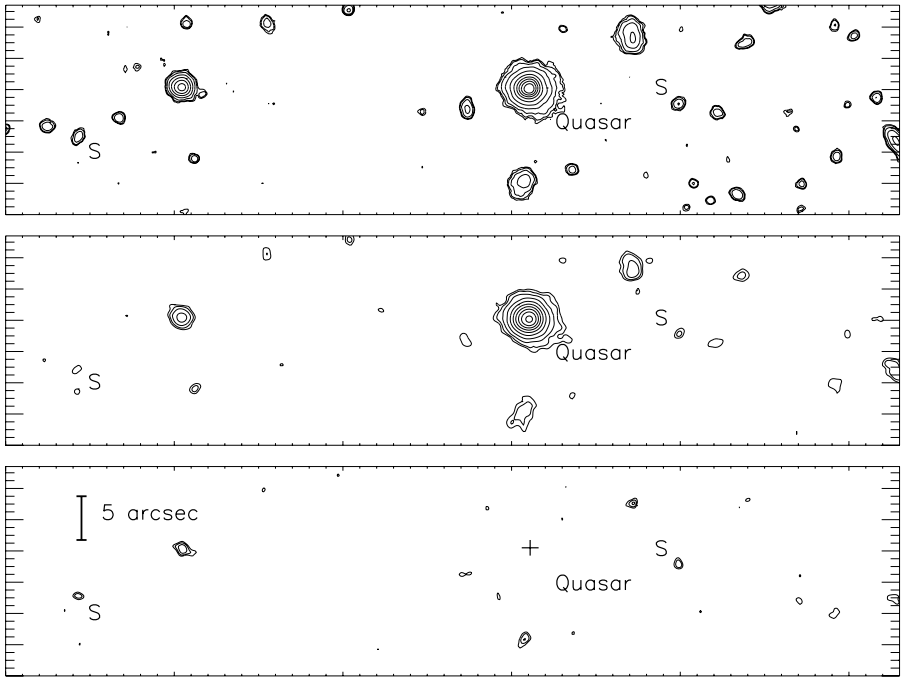

Figure 6.1: *Top panel :* 96×24 arcsec^2 surrounding PKS1157+014 from 4000sec of integration in the I-band. Marked are the quasar and two candidate emission line galaxies (S). North is to the left and east is down. *Middle and lower panels :* The same field as above, but from 4000sec of integration in the U-band and 10 hours of integration in the narrow filter.

6.4 Are Lyman-break galaxies and DLAs the same objects?

In the last few years hundreds of high redshift galaxies have been found using a technique completely independent of QSO absorption lines. This technique is based on the fact that young, starforming galaxies will have a strong spectral break at the lyman limit, which at high redshift is redshifted into the optical window (see Dickinson 1999, for a recent review). Galaxies found using this method are refered to as Lyman-break galaxies (LBGs). LBGs need to be bright enough for spectroscopical confirmation of their high redshift so they are typically brighter than R(AB)=26. Since DLAs and LBGs are selected completely independently from the population of progenitor galaxies it is very interesting to compare the recent results for the LBGs with results from studies of DLAs. Assuming that DLAs arise in gaseous discs associated with LBGs one way to perform this comparison is to calculate how faint we need to integrate down the extrapolation of the luminosity function of LBGs in order to explain the observed probability for a QSO line of sight to cross a DLA.

Results of this calculation are presented in Fynbo et al. 1999a, and summarised here. At

$z = 3$ we find that 70-90% of DLA galaxy counterparts are fainter than R(AB)=26, which is the current limit for spectroscopic confirmation of LBG candidates. Since DLAs contain close to all the gas that make up present day galaxies we conclude that the progenitors of a typical present day galaxy at $z = 3$ were small and faint and that the LBGs only constitute the tip of the iceberg of high redshift galaxies in terms of locating the reservoir of cold gas out of which present day galaxies formed. This is also consistent with the results from semi-analytical modeling of galaxy formation in which LBGs form in very rare high overdensity regions and are the progenitors of present day bright cluster galaxies (e.g. Baugh et al. 1998). Hence when we wish to study properties such as metallicity, dust content and star formation for the population of progenitor galaxies as a whole, the DLAs are more likely representative than LBGs.

Chapter 7

Lyα Emission from a Lyman Limit Absorber at z=3.036

Fynbo, J.U., Thomsen B., Møller P., 2000, A&A, 353, 457

7.1 Introduction

The amount of information about the galaxy population at high redshift ($z = 2 - 4$) has increased tremendously in the last few years. Using the Lyman-break technique several hundred high redshift star forming galaxies, Lyman-break galaxies (LBGs), have been detected and studied with imaging and spectroscopy (Steidel et al. 1996b). It is, however, not yet known how complete the Lyman-break technique is in detecting high redshift galaxies.

An independent route along which to study the galaxy population at high redshift is via the high column density QSO absorption lines systems. The advantage of high column density QSO absorption lines systems is that a wealth of information on the chemical evolution can be and has been obtained by studying the metallicity and dust content of the absorbers from high resolution spectroscopic studies of the background QSOs (e.g. Lu et al. 1996). However, the spectroscopic studies will not tell us anything about the emission properties of the absorbing galaxies.

Only when combining the information obtained from the LBG-studies (e.g. the luminosity function of LBGs), the absorption line statistics for QSO absorption lines systems and the properties of galaxy counterparts of QSO absorption lines systems can we hope to disentangle the observational selection biases which each of the different studies suffer from and obtain a more complete insight into the nature of the high redshift galaxy population.

The absorption line systems with the highest HI column density, $N(HI) > 2 \times 10^{20}$ cm^{-2}, are the Damped Lyα Absorbers (DLAs, Wolfe et al. 1986)[1]. Such high HI column densities are at low redshift only found in the disks of spiral galaxies. It it also interesting to note, that active star formation in spiral galaxies only occurs when the HI column density of the disk exceeds $2 \times 10^{20} cm^{-2}$ (Kennicutt 1989). For these reasons, DLAs are widely believed to trace the central parts of forming galaxies. Much telescope time has been dedicated to the narrow band imaging of DLAs over the past decade (e.g. Lowenthal et al. 1995 and references therein), but so far resulting in only two confirmed detections for the DLAs towards PKS0528-250 (Møller & Warren 1993a,b; Warren & Møller 1996), and Q0151+048A (Møller et al. 1998; Fynbo et al. 1999a) In addition a spectroscopically confirmed broad band detection of the DLA towards DMS2247-0209 (Djorgovski 1998) and a purely spectroscopic detection of Lyα emission from the DLA towards Q2059-360 have been reported (Pettini et al. 1995, Leibundgut & Robertson 1998), as well as a number of DLA candidates, which have not yet been confirmed by spectroscopy (Steidel et al. 1994, 1995b, Aragón-Salamanca et al. 1996, LeBrun et al. 1997).

QSO absorption line systems with N(HI) larger than a few times 10^{17} cm^{-2} are optically thick at the Lyman limit and refered to as Lyman Limit Systems (LLSs). Lyman limit

[1]When comparing absorbers to statistical samples of DLA absorbers, it is important that they meet this N(HI) criterion. However, some authors also refer to absorbers with $N(HI) < 2 \times 10^{20}$ cm^{-2} as DLAs, e.g. Lanzetta et al. 1997.

absorption is believed to occur in extended gaseous haloes of galaxies, because the neutral hydrogen column density is much larger than in the intergalactic medium and the gas is not predominantly neutral as in DLAs. At low redshifts, where the Lyman limit cannot be observed from the ground, LLS are thought to be traced by MgII absorption, because MgII absorption only occurs in optically thick clouds (Schaeffer 1983). The extensive study of the galaxy counterparts of MgII absorbers presented in Guillemin & Bergeron (1997) shows that MgII absorption predominantly occurs in Sbc or Scd galaxies, but that the objects range from ellipticals to irregular galaxies. At high redshifts the Lyman Break technique were originally used to look for galaxies responsible for Lyman limit absorption in QSO spectra (Steidel & Hamilton 1992). Two candidates were found in six fields (Steidel et al. 1995a), but for only one of these, the LLS towards Q2233+131, has confirming spectroscopy been published (Djorgovski et al. 1996).

Three out of the four confirmed high redshift DLAs that have been detected in emission at present are at approximately the same redshift as the background QSO. In order to examine whether $z_{abs} \approx z_{em}$ systems indeed are more active emitters (e.g. due to induced star formation or to photoionisation by the QSO; for the suggested mechanisms see Møller & Warren 1993b and Fynbo et al. 1998) we have initiated a programme aimed at studying the galaxy counterparts of this special subgroup of high column density QSO absorption line systems. As part of this programme we chose to study the quasar Q1205-30 of which a spectrum published by Lanzetta et al. (1991) shows the presence of a strong LLS close to the emission redshift of the QSO. The redshift of the quasar is $z_{em} = 3.036$.

In Sect. 7.2 of this paper we describe the observations obtained with the ESO New Technology Telescope (NTT) and the basic data reduction. In Sect. 7.3 we discuss the photometry, the selection of Lyα emission line candidates, and the correction for the quasar point spread function. In Sect. 7.4 we discuss our results. We adopt a Hubble constant of $100\mathrm{h}^{-1}$ km s^{-1} Mpc^{-1} and assume Ω_m=1 and Ω_Λ=0 unless otherwise stated.

7.2 Observations and Data Reduction

A spectrum of the quasar Q1205-30 can be found in Lanzetta et al. (1991), but its celestial coordinates were never made publicly available. To obtain an image we therefore had to "rediscover" Q1205-30 on a copy of the prism plate UJ9085P kindly made available to us from the UK Schmidt Telescope Objective Prism Survey (for details of the procedure see Fynbo et al. 1999b). Celestial coordinates of Q1205-30 are RA 12 05 35.72, Dec -30 14 25.8 (1950).

Deep imaging of the field was subsequently carried out in NTT service mode (Silva & Quinn 1997, Silva 1998, Woudt & Silva 1999). The field was imaged through standard B and Bessel I filters, as well as through a special 20Å (fwhm) narrow band filter manufactured

Filter	Combined fwhm (arcsec)	Exposure Time (sec)	Pixel scale (arcsec/pixel)
CS 4906/20	1.4	64000	0.35
B	1.3	3600	0.35
I	0.96	5600	0.27

Table 7.1: Journal of observations, NTT, January through March 1998.

by Custom Scientific. The narrow band filter (CS 4906/20) is centred at 4906Å, which is the wavelength of redshifted Lyα at $z = 3.036$. The service mode data were obtained with the ESO Multi-Mode Instrument (EMMI) on the NTT during several nights of January, February and March, 1998. The CCD used in the red arm of EMMI was a SITe TK2048 with a pixel scale of 0.27 arcsec. The blue arm CCD was a SITe TK1024 with a pixel scale of 0.35 arcsec. The total integration times in each filter and the seeing in each of the combined frames are given in Table 7.1.

Landolt (1992) photometric standards and three spectrophotometric standard stars Eggr99, Feige 56 and L970 were used for the photometric calibrations.

I–band imaging was obtained with the red arm of EMMI. The CCD in the red arm of EMMI can be read in either single port (D only) or dual port (A + D) read–out mode. Unfortunately it showed up that for our programme a mix of single and dual port read–out had been employed, and we had to follow a somewhat complex reduction procedure to make up for this.

The disadvantage of the single port read–out is the longer read time required (which is particularly a problem while obtaining twilight flats). The disadvantage of the dual port read–out is that the bias level, the gain (and drift of the gain), and the readout noise are different for the two image sections. Also the locations of traps (bad columns) depend on the direction of charge transfer along the columns. In particular the section read through port A has more bad columns than the same section read through port D. The I–band science exposures of Q1205-30 were read out using dual port read–out, whereas the exposures of standard stars were read out using single port mode only. This mixed mode operation requires 2 sets of biases, as well as two sets of flat fields, and two different ways of reducing the images. Twilight flats were only obtained for single port mode (appropriate for the standard star exposures), while dome flat were taken with dual port read–out (appropriate for the science frames). The dual read exposures were treated as if the A and D subsections were two individual frames. Finally, bias frames, flat field exposures, and science exposures were pasted together to form 2048x2046 frames. The subsequent flat-fielding was done in the usual way.

Table 7.2: Measured level and rms of sky surface brightness.

passband	sky	rms SB
	mag_{AB}. arcsec^{-2}	mag_{AB}. arcsec^{-2}
n(AB)	21.9–22.4	27.9
B(AB)	22.5	28.5
I(AB)	19.7	27.5

The CCD in the blue arm of EMMI can be read in single port mode only. All science frames obtained with the blue arm of EMMI (all B–band and narrow band data) were bias–subtracted and flat–fielded using standard routines.

Following the basic reduction the images in each of the three filters were combined employing the code described in Møller & Warren (1993a). This code optimizes the signal–to–noise for faint objects in the field, for which the noise is well understood via propagation of read–out–noise and photon shot noise.

All magnitudes quoted in this paper are on the AB system. The narrow band data were calibrated directly onto the AB system using the spectrophotometric standard stars, and these magnitudes are denoted $n(AB)$. We found that the colour terms for both the I and B filters were consistent with zero, hence we use the equations $I(AB) = I + 0.43$ and $B(AB) = B - 0.14$ (Fukugita et al. 1995) to put the broad band magnitudes onto the AB system. Details of the sky brightness and sky noise in the combined images are provided in Table 7.2.

We reach limiting magnitudes (5σ) of n(AB)=25.0, B(AB)=25.8 and I(AB)=25.1. A narrow band AB magnitude of 25.0 corresponds to a Lyα flux of 1.1×10^{-17} erg s^{-1} cm^{-2}.

7.3 Results

A contour plot of the combined I–band image of the 315x315 arcsec^2 field surrounding Q1205-30 is shown in Fig. 7.1. Q1205-30 itself is here marked by a 'q' and an arrow. The star from which the central core of the Point Spread Function was defined (see Sect. 7.3.1) is marked 'PSF'. Six candidate Lyα emitting galaxies (see Sect. 7.3.3) are marked "+".

7.3.1 Objects near the line of sight towards Q1205-30

Q1205-30 was selected for observation because of the high column density absorber seen along the line–of–sight towards it. Previous detections of high column density absorbers (for a recent summary see Møller & Warren 1998) suggest that their absorption cross–section is very small, and that emission from the object therefore likely will be hidden under the quasar

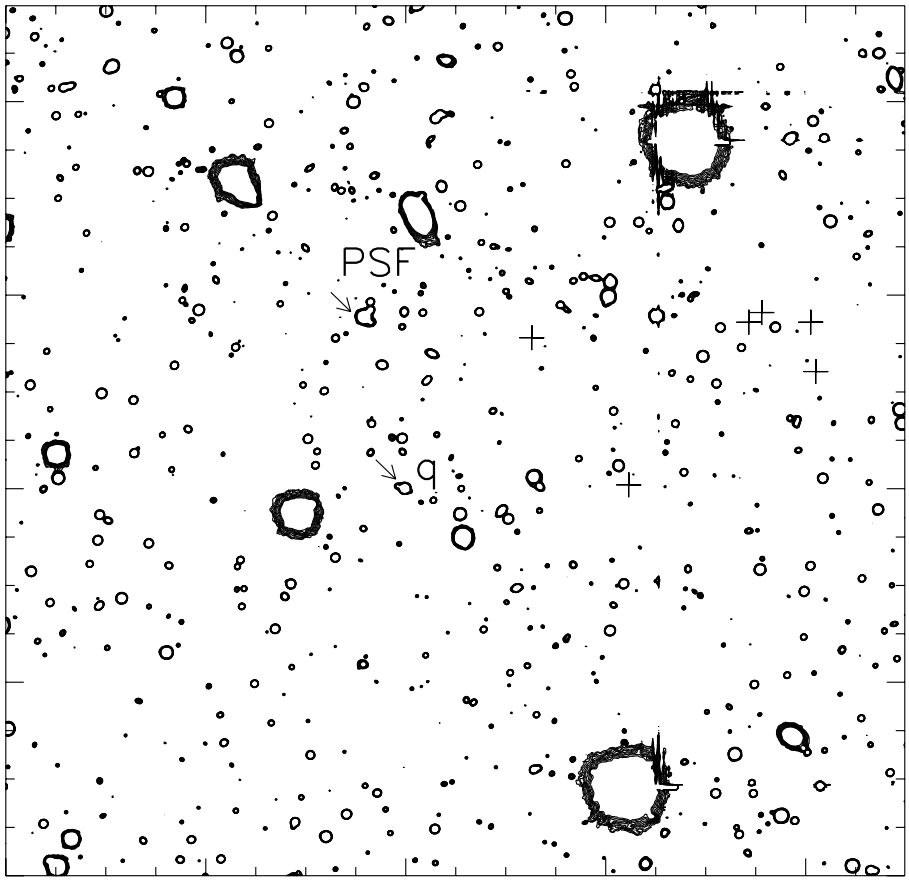

Figure 7.1: Contour plot of the I–band frame showing the 315x315 arcsec^2 field surrounding Q1205-30. North is up and east to the left. Q1205-30 is shown by the arrow next to the "q". The star used to define the PSF is marked 'PSF' (see Sect. 7.3.1). The positions of six candidate Lyα emitting galaxies are marked with a "+" (see Sect. 7.3.3).

PSF. To search for emission from the absorbing object we therefore performed a careful PSF subtraction as detailed in this section.

The basic principles of the PSF subtraction are as described in Møller & Warren (1993a), and Fynbo et al. (1999a). For a first approximation to the PSF we used the star marked 'PSF' in Fig. 7.1. This is the nearest unsaturated point source significantly brighter than Q1205-30, but as is evident from Fig. 7.1 it has four nearby neighbour objects (projected distances in the range 4–9 arcsec). The signature of those four objects does not affect the core of the PSF. Their effect on the halo of the PSF was masked out and removed via substitution of the masked regions by areas selected from scaled high S/N halos from isolated point–sources brighter than the PSF–star (and hence saturated in the central core). The comparatively large projected distances (4 arcsec and larger) means that the presence of

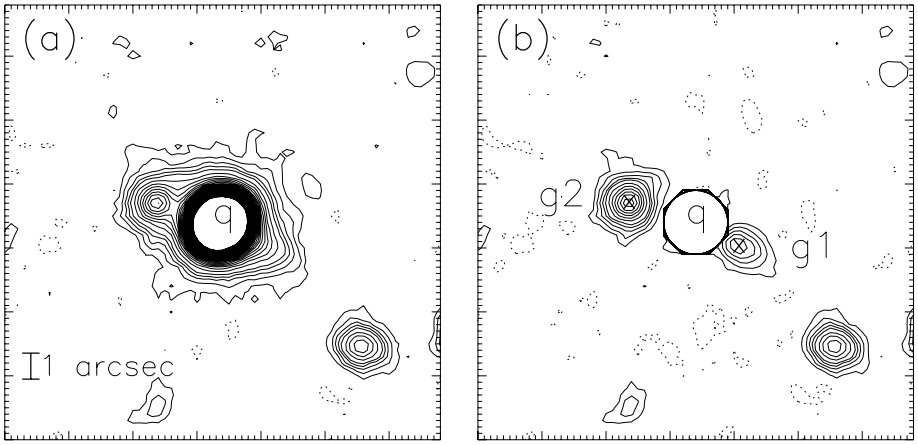

Figure 7.2: Contour plot of the I–band frame showing an 18x18 arcsec^2 field surrounding Q1205-30. North is up and east to the left. The frame has been smoothed by a 3x3 pixel boxcar filter. *Left:* final combined frame (QSO is marked q). The contour levels are at -9, -6, -3, 3, 6, 9... in units of the background noise, with the dotted contours being negative. *Right:* same as left but here after subtraction of the quasar PSF, revealing two galaxies marked g1 and g2 at separations 2.2 and 2.8 arcsec (from the QSO) respectively. Their centroids are marked "×". A circle of radius 1.3 arcsec has been drawn around the centre of the subtracted PSF (see text for details).

those objects, even if not corrected for, would not in any case have had any effect for the results reported below.

The DAOPHOT-II (Stetson 1997) extension ALLSTAR was used to perform the final PSF model fit and subtraction. Identical procedures were followed for the PSF subtraction in all combined images: Narrow band, B and I.

In Fig. 7.2 we show a 18x18 arcsec^2 cut–out of the I–band image centred on Q1205-30 before (a) and after (b) subtraction of the quasar PSF. The quasar is marked "q", and it is clearly seen that two faint galaxies (named g1 and g2) were blended with the quasar PSF. In Fig. 7.2(b) we have drawn a circle of radius 1.3 arcsec around the centre of the subtracted PSF. Inside this circle the large residuals (not shown) from the PSF subtraction make it impossible to search for objects. The galaxy g2 is well separated from the PSF–subtraction residuals so its projected distance from Q1205-30 (2.8 arcsec) is well determined. In contrast, g1 is partly embedded in the residuals. The galaxy g1 could therefore in reality be an elongated object extending across the quasar, and the *measured* projected distance (2.2 arcsec) is hence an upper limit to the *true* projected distance. The measured I–band centroids of the galaxies g1 and g2 are marked by an "×" in Fig. 7.2(b).

In Fig. 7.3(a,b) we show the same 18x18 arcsec^2 cut–out of the B–band image. Here we

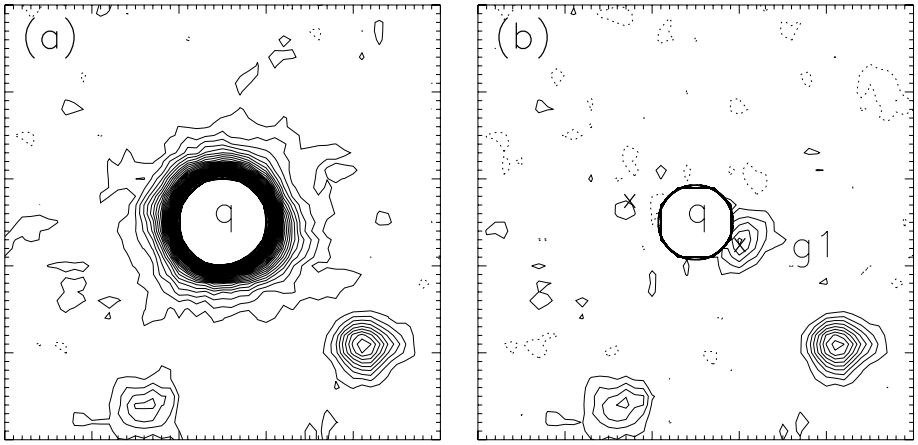

Figure 7.3: Same as Fig.2 but here for the B–band image. The contour levels are at -6, -4, -2, 2, 4, 6... in units of the background noise with dotted contours being negative. *Right:* Here a circle of radius 1.5 arcsec has been drawn around the centre of the subtracted PSF. The "×"s mark the centroids of the galaxies g1 and g2 as measured on the I–band image.

have drawn a circle of radius 1.5 arcsec, again to mask out the area where PSF subtraction makes it impossible to search for objects. The "×"s here again mark the centroids of the galaxies g1 and g2 as measured on the I–band image. In the B–band image g1 is found at the same projected distance as in the I–band image while the extremely red object g2 is not detected.

In Fig. 7.4(a,b) we again show the same 18x18 arcsec^2 cut–out as above, but here from the combined narrow band frame. The "×"s here again mark the centroids of the galaxies g1 and g2 as measured on the I–band image. In this image we clearly see an extended object (named S6) to the north of the quasar, possibly extending all the way to the east of the quasar. Note that g1 here is found at a slightly larger projected distance from the quasar than in the I–band and B–band images. This illustrates the point we made above that the PSF subtraction will tend to "push" the object out at a larger distance, because part of the object is embedded in the non–recoverable central part of the PSF. This will then also impact the photometry, as the total flux of the object will be underestimated. The position of g2 (marked by '×' and a dotted circle) corresponds to a faint protrusion on the extended object. Since the narrow band is within the B passband, we would indeed expect to see only very weak emission from the extremely red object g2.

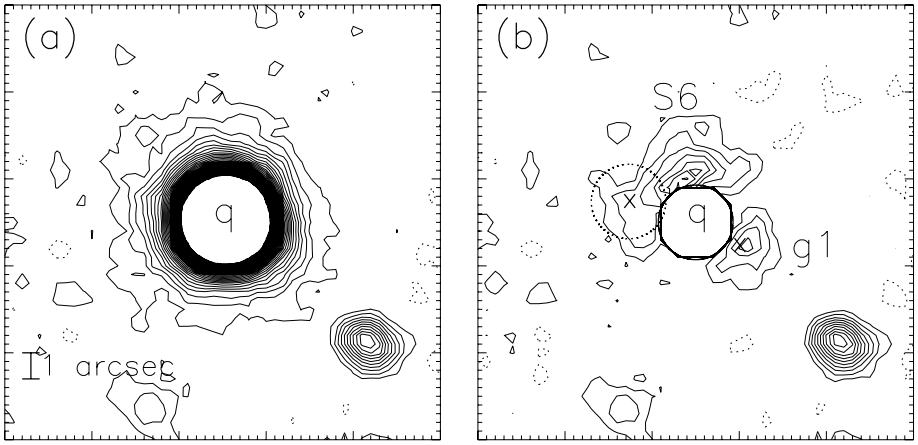

Figure 7.4: *Left:* Same as Fig.2 but here for the narrow band image. The contour levels are at -6, -4, -2, 2, 4, 6..., in units of the background noise, with the dotted contours being negative. *Right:* Here the PSF of the quasar has been subtracted, revealing a large extended object (named S6) to the north, possibly extending to the east, of Q1205-30. A circle of radius 1.5 arcsec has been drawn around the centre of the subtracted PSF. The dotted circle marks the extend of g2 in the I–band image, and the "×"s mark the centroids of the galaxies g1 and g2 as measured on the I–band image.

7.3.2 Photometry of objects near the QSO line of sight.

In this subsection we describe the photometry on Q1205-30, g1, g2 and S6 in the three filters B, I and narrow band. For g1 we measured the flux inside a circular aperture of diameter 3.5 arcsec. The resulting magnitudes presented in Table 7.3 will be somewhat underestimated since we miss the flux closer than 1.5 arcsec from the QSO. For g2 we also measured fluxes in circular apertures of diameter 3.5 arcsec. We did not detect g2 in B, and hence provide the 2σ detection limit. The galaxy g2 is very red, consistent with being an old stellar population at a redshift of about 0.5 or more. In Sect. 7.4.1 we discuss the possible effects of g2 on the line of sight due to gravitational lensing. In the narrow band image we can not in an objective way determine whether the flux detected at the position of g2 originates from g2 or from S6. Hence we chose to consider two extreme cases for the photometry of S6 and g2 in the narrow filter.

In model A (minimum Lyα flux model; Fig 7.4a) we subtracted the maximum flux we can possibly ascribe to g2 in the narrow band. We used a model of g2 obtained by smoothing the I band image of g2 to the seeing of the narrow band image, and then determined the maximal scaling of this model which after subtraction left residuals consistent with the noise. The remaining flux, making no correction for flux from S6 within the central core of the subtracted quasar PSF, was assigned to S6. In model B (maximum Lyα flux model;

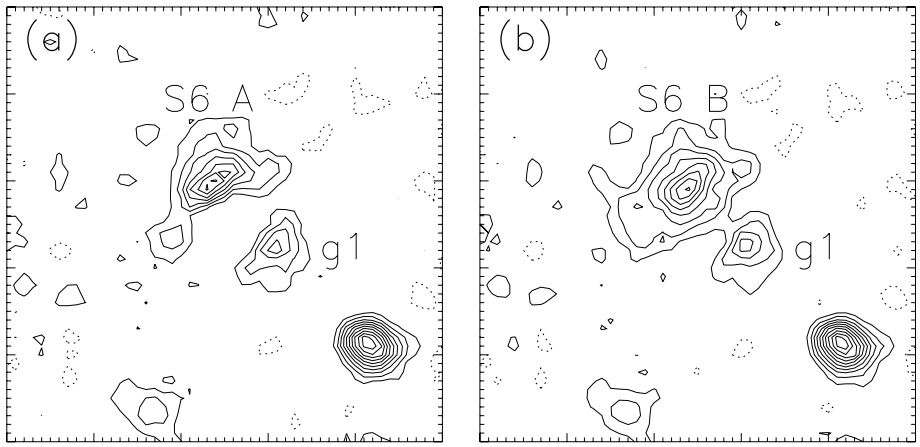

Figure 7.5: Two "extreme" models of S6. *Left:* in model A we assume that all the flux seen at the position of g2 is indeed from g2, and we make no allowance for flux from S6 within the central core of the quasar PSF. *Right:* in model B we assume that no significant flux is seen from g2, and we model S6 within the central core of the quasar PSF assuming that S6 is symmetric about its major axis with position angle 120° east of north.

Fig 7.4b) we assumed that all the flux seen north and east of Q1205-30 originates from S6 and not from g2. In order to estimate the flux within the central core of the quasar PSF we assumed that S6 is symmetric about its major axis (PA 120° east of north). A model of S6 was made as follows. First we flipped the image of S6 around its major axis. In the PSF subtracted image we then replaced the region inside radius 1.5 arcsec from the quasar PSF with the flipped image. The flux of the model was measured using a circular aperture of diameter 4.9 arcsec.

The impact parameter of S6 was found to be 1.8 arcsec in model A and 1.5 arcsec in model B. The Lyα flux of S6 is $6.6\pm0.6\times10^{-17}$ erg s^{-1} cm^{-2} (model A) and $7.9\pm0.7\times10^{-17}$ erg s^{-1} cm^{-2} (model B).

7.3.3 Candidate Lyα emitting galaxies in the field

The "narrow minus on–band–broad" versus "narrow minus off–band–broad" colour/colour plot technique (Møller & Warren, 1993a; Fynbo et al. 1999a) has proven a powerful tool to identify galaxies in the faintest end of the high redshift galaxy luminosity function (LF). We here describe the search procedure and the photometric measurements carried out with the aim to produce the plot shown in Fig. 7.6.

Identification and photometric measurements of objects in the field was done with the photometry package SExtractor (Bertin & Arnouts 1996). We used a minimum object

Table 7.3: Photometric properties of the QSO, of the faint galaxies g1 and g2 and of the Lyα emitter S6. Upper limits to magnitudes are 2σ except for g1, where the limit is determined from model A mentioned below.

Object	B(AB)	I(AB)	n(AB)	Apert. (arcsec^2)
q	18.92	18.13	18.28	60
S6 A	> 26.2	> 25.2	22.90±0.10	19
S6 B	> 26.2	> 25.2	23.10±0.10	19
g1	24.8 ± 0.1	23.3 ± 0.1	24.1 ± 0.2	9.6
g2	> 26.5	22.22 ± 0.05	$\geq 24.8 \pm 0.3$	9.6

extraction area of 8 pixels and a detection threshold of 1.3σ above the background. As our detection image we selected to use a weighted average of the three combined frames. The weights were chosen to be the inverse of the variance in each of the combined frames. As a detection filter we used a Gaussian filter with a full-width-at-half-maximum (fwhm) of 4 pixels similar to the fwhm of point sources in the detection image, which is 3.4 pixels.

In total we detected 473 objects with a signal–to–noise ratio (S/N) > 5 in the narrow band. In Fig. 7.6 we show the colour–colour diagram $n(AB)-B(AB)$ *versus* $n(AB)-I(AB)$ for the entire sample. In this diagram objects with Lyα emission in the narrow band filter will be located in the lower left corner while objects with absorption in the narrow filter will be located in the upper right hand corner. Since our narrow filter is centred at 4906Å, which is in the red wing of the B filter, the $n(AB)-B(AB)$ colour of an object will depend on the slope of the objects spectral energy distribution. Very red objects will, therefore, appear to have a slight excess emission in the narrow band, causing the locus of continuum sources to be slightly tilted towards the lower right of the diagram.

We determined the expected region for objects with no special feature in the narrow band by calculating the position in this diagram for a wide range of galaxy spectral energy distributions taken from the models of Bruzual & Charlot (1993) The galaxy models were calculated for several redshifts in the range $z = 0$ to $z = 3.5$, and were corrected for Lyα line blanketing due to intervening absorbers (Møller & Jakobsen 1990). The resulting region is indicated by the dotted line in Fig. 7.6.

Inspection of Fig. 7.6 clearly shows that the vast majority of the detected objects indeed conform to the predicted colours. Three objects to the lower left are, however, found to lie significantly outside the locus of continuum objects. All three are found in the region expected for blue objects with an emission line in the narrow filter.

The detection limit in the combined image used for object detection is dominated by the deeper broad band images. Faint objects with large equivalent width Lyα emission

Table 7.4: Photometric properties of the six candidate Lyα emitting galaxies. Upper limits to magnitudes and lower limits to equivalent widths (EWs) are 2σ. SFRs are calculated assuming a Ω_m=1 and Ω_Λ=0 universe, and using the prescription SFR=L(Lyα)/1.12 $\times$ 10^{42} erg s^{-1}.

Object	n(AB)	B(AB)	I(AB)	Lyα flux	EW_{rest}	SFR
Isophote				10^{-17} erg s^{-1} cm^{-2}	Å	h^{-2} $M_\odot$
S7	24.13±0.14	25.8±0.3	25.0±0.3	2.56±0.33	20±7	0.40±0.05
S8	24.46±0.15	>26.9	>26.0	1.89±0.26	>45	0.30±0.04
S9	23.43±0.09	25.3±0.2	24.9±0.3	4.88±0.40	25±6	0.77±0.06
S10	24.78±0.18	>27.0	>26.1	1.41±0.23	>36	0.22±0.04
S11	24.83±0.18	>27.0	>26.2	1.34±0.22	>34	0.21±0.04
S12	24.96±0.19	>27.1	>26.3	1.19±0.21	>33	0.19±0.03
Aperture (3.5 ″ diameter)						
S7	23.90±0.13	25.5±0.3	25.0±0.3	3.17±0.39	18±6	0.50±0.06
S8	23.90±0.13	>26.1	>25.6	3.16±0.39	>35	0.50±0.06
S9	23.32±0.07	25.2±0.2	24.6±0.2	5.40±0.37	25±6	0.85±0.06
S10	24.33±0.19	>26.1	>25.6	2.13±0.42	>22	0.34±0.07
S11	24.42±0.21	>26.1	>25.6	1.96±0.42	>20	0.31±0.07
S12	24.45±0.22	>26.1	>25.6	1.90±0.42	>19	0.30±0.07

might therefore be missed by the detection algorithm. To make up for this we repeated the detection procedure, but this time using the narrow band image for detection. SExtractor found six emission line objects with S/N> 5. Three of those were the ones reported already from the combined image detection, while the other three remain undetected in broad band.

In addition to S6 we hence detect a total of six emission line objects at S/N> 5. The positions of the six objects are marked by crosses in Fig. 7.1. Image cut–outs showing the 6 objects in each of the three bands are reproduced in Fig. 7.7. Photometric properties of the emission line objects are reported in Table 7.4. Magnitudes were measured using both SExtractor isophote apertures and large circular apertures. Emission line fluxes corresponding to the measured n(AB) aperture magnitudes range from 1.9 $\times$ 10^{-17} erg s^{-1} cm^{-2} to 5.4 $\times$ 10^{-17} erg s^{-1} cm^{-2}.

As seen in the insert in the upper left corner of Fig. 7.6, Q1205-30 has only a slight excess emission in the narrow band filter which covers Lyα of the quasar also. The weakness of this excess emission is the result of the blue wing of the Lyα emission line of the QSO being absorbed partly by the Lyman limit absorber.

7.4 Discussion and Conclusions

7.4.1 The Lyman Limit Absorber

We have detected an object, S6, with extended line emission north and east of the quasar Q1205-30. The emission line of S6 is detected in a narrow band tuned to Lyα of a Lyman Limit absorber in front of Q1205-30, and the most likely interpretation is, that we see the Lyman Limit absorber in Lyα emission. Spectroscopic follow–up is required to confirm this tentative conclusion. The large residuals from the PSF subtraction of the quasar introduce errors in both the total line luminosity observed, and the impact parameter. We have therefore considered two extreme cases described in Sect. 7.3.2; the minimal Lyα flux case (model A) and the maximal Lyα flux case (model B). For the Lyα luminosity and the impact parameter in the two models we find L=11.6$\pm$1.1 $\times$ 10^{41} h^{-2} erg s^{-1}(14.1$\pm$1.3 $\times$ 10^{41} h^{-2} erg s^{-1}) and d=6.5 h^{-1} kpc (5.4 h^{-1} kpc) for model A (model B). In the following we will assume the more likely model B to be correct. Fynbo et al. (1999a, their Table 4) lists the Lyα line luminosities of the known galaxy counterparts of high redshifts DLAs and LLSs, namely the DLAs towards PKS0528-250 (named S1), Q0151+048A (named S4) and Q2059-360, and the LLS towards Q2233+131. The observed Lyα line luminosity of S6 is within the range 1.1–12 $\times$ 10^{42} h^{-2} erg s^{-1} of these other systems.

The size of the line emission region is 6$\times$4 arcsec^2 corresponding to 22$\times$14 h^{-2} kpc^2 at z=3.036. This size and the morphology of S6 are both near–identical to those of the emission line object S4, which has been shown in a spectroscopic study (Møller et al. 1998) to be a DLA galaxy unrelated to the underlying quasar. Before the precise systemic redshifts of both the QSO and S6 have been measured we cannot exclude that S6 is related to Q1205-30.

From neither S4, nor S6, do we detect what is obviously continuum emission from a high redshift galaxy. This, however, is not surprising as continuum emission from the high redshift DLA galaxy S1 was not detected in the deep ground based images of S1 (Møller & Warren, 1993a), but a compact galaxy was subsequently found in the HST images (Møller & Warren 1998). Since the impact parameters of S1, S4, and S6 are similar, clearly HST imaging is required to resolve the question of their continuum morphology.

Both the comparatively large luminosity and the extended morphology of S6 is in contrast to six faint and compact emission line galaxies (S7–S12) found at much larger distances from the quasar. We hence consider it likely, as in the case of Q2059-360 (Leibundgut & Robertson 1998, Fynbo et al. 1999a), that the emission from S6 is significantly influenced by the proximity of the active nucleus. It is, however, possible that gravitational lensing by the red galaxy g2, if it is a foreground elliptical galaxy, makes S6 appear more extended and increases its observed flux. Here we estimate the likely strength of this effect.

Assuming that g2 is at z=0.5 and has an isothermal mass profile with a velocity dispersion

of 300 km s^{-1}, the radius of its Einstein ring is given by

$$\theta_E = 4\pi(\frac{\sigma}{c})^2 \frac{d_{LS}}{d_S} = 1\farcs6,$$

where d_{LS} and d_S are the proper angular diameter distances between g2 (Lens) and S6 (Source) and between the earth and S6 respectively, in the assumed cosmology. Gravitational lensing in this simple model moves S6 and Q1205-30 by an angle θ_E in the radial direction away from g2 causing a tangential stretching of S6 as well as an increase of the observed impact parameter of S6 relative to Q1205-30 by a factor of $\approx \theta_{g2}/(\theta_{g2} - \theta_E)$=2.3 (where θ_{g2}=2.8 arcsec is the observed impact parameter of g2 relative to the QSO). The magnification of the flux of S6 would be in the range 2–10 depending on the unknown size and orientation of the diamond caustic of g2. A possible counter image on the eastern side of g2 would make S6 look more extended in the relatively low resolution of the narrow band image, in the direction of the observed elongation which would be of order $2\theta_E$.

7.4.2 The field population of Lyα emitting galaxies

The presence of the six emission line galaxies S7–S12 in the field of Q1205-30 is interesting for several reasons. The faintness of the broad band magnitudes of the objects makes it unlikely that they are low redshift (z $\approx$ 0.31) galaxies with Oxygen emission lines in the narrow filter. The most likely identification of the emission lines is Lyα at the same redshift as the Q1205-30 LLS absorber, and in what follows we shall assume this to be the case.

Only one of the six emission line galaxies (S9) would have been selected as an LBG in current ground based programmes. The remaining five are too faint in the broad bands (see Table 7.4). The number of LBGs brighter than R(AB)=25.5 with redshifts between 3.0 and 3.5 selected from ground based surveys is 0.4±0.07 galaxies arcmin^{-2} (Steidel et al. 1996), and we hence expect 11 in our 27.6 arcmin^2 field. Assuming that LBGs have redshifts uniformly distributed between 3.0 and 3.5 we would expect on average 0.4 LBGs within the redshift range $dz = 0.016$ corresponding to the width of the narrow filter. In the Hubble Deep Field North the LF of LBGs has been extended to R(AB)=27 (Steidel et al. 1999). Integrating this LF leads to an expected number of LBGs of about 0.3 galaxies arcmin^{-2} within the redshift range $dz = 0.016$ or on average 9 in our 27.6 arcmin^2 field (see Sect. 4.2 in Fynbo et al. (1999a) for a discussion on the relation between the redshift density $\frac{dN}{dz}$ of DLAs and the LF of LBGs). Hu et al. (1998), have reported on detections of Lyα emitting galaxies by means of narrow band imaging and long slit spectroscopy in random fields with densities about 4 arcmin^{-2} per unit redshift down to similar depths in observed flux as in our sample, but at somewhat higher redshifts.

Hence, narrow/broad band Lyα imaging indicate the existence of a significant population of high redshift galaxies that is not included in current ground based LBG samples and which

is possibly identical to the faint LBGs detected by HST. Those galaxies, which make up the faint end of the high redshift galaxy LF, have large Lyα equivalent widths and are about a factor of 10 more numerous than the bright LBGs of current ground based samples. This result is in good agreement with our earlier conclusion based on searches for DLA galaxies (Møller & Warren 1998; Fynbo et al. 1999a) that there is a significant population of faint high redshift galaxies which, despite their very small HI absorption cross–section, make up most of the high redshift DLA absorbers.

Total Lyα luminosities for S7–S12 are in the range 3.3–9.5 $\times$ 10^{41} h^{-2} erg s^{-1} for Ω_m=1.0 and 12–34 $\times$ 10^{41} h^{-2} erg s^{-1} for Ω_m=0. Using the Kennicutt (1983) prescription SFR = L(Hα)/1.12 $\times$ 10^{41} erg s^{-1} and assuming L(Lyα)/L(Hα)=10 and negligible dust extinction, we find star formation rates in the range 0.2 – 0.8 h^{-2} $M_\odot$ yr^{-1} for Ω_m=1.0 and 1.1–3.0 h^{-2} $M_\odot$ yr^{-1} for Ω_m=0. The large equivalent widths of the emission lines make strong dust obscuration unlikely. The star formation rates for R(AB)<25.5 LBGs as estimated from Balmer and OII emission line strengths by Pettini et al. (1998), fall in the range 20 – 270 $M_\odot$ yr^{-1} for Ω_m=0.2 and h=0.7. For Ω_m=1.0 this corresponds to 4–55h^{-2} $M_\odot$ yr^{-1}. Hence, the Lyα emitting galaxies have star formation rates about an order of magnitude lower than what is measured for the bright LBG population. Nevertheless, since the population of Lyα emission line galaxies is much more common than the brighter LBG population, it is still an open question if the *integrated* SFR is dominated by the faint or the bright end of the high redshift galaxy LF.

As seen in Fig. 7.1 the faint galaxies are all located in a region north west of the QSO. Their projected impact parameters from Q1205-30 range from 156 to 444 h^{-1} kpc, and four of the six galaxies are found in a small region of projected size 100 $\times$ 100 h^{-2} kpc^2. As for the compact group S1–S2–S3 associated with a z=2.81 DLA absorber, this compact group of faint galaxies associated with a z=3.036 LLS absorber is destined to merge on a short timescale (Navarro et al. 1995; Haehnelt et al. 1998). This, then, supports the suggestion (Warren & Møller 1996; Møller & Warren 1998) that high redshift, high column density absorbers predominantly are proto–galactic sub–clumps in the process of early galaxy assembly, rather than fully formed large rotating disks.

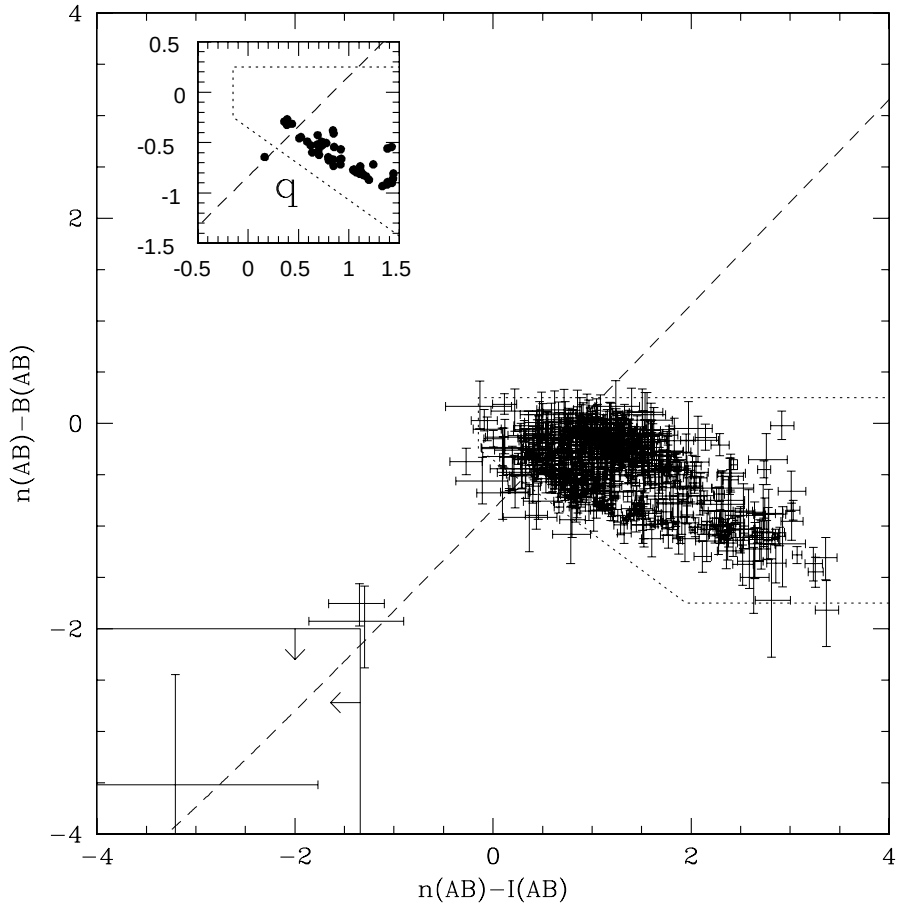

Figure 7.6: Two-colour diagram $n(AB)-B(AB)$ *versus* $n(AB)-I(AB)$ for objects detected at a S/N > 5 in the narrow band frame. The dashed line is a line of constant $B-I$ in the continuum (chosen to be that of Q1205-30), but with a spectral feature in the narrow filter ranging from a strong absorption line in the upper right hand corner to a strong emission line in the lower left hand corner. Three of the six candidate emission line galaxies are seen in the lower left corner. The remaining three are detected in neither B nor I. For these galaxies the lines with arrows indicate the 2σ allowed region in the diagram. The dotted lines confine the expected region of objects with no special features in the narrow filter. The inserted diagram shows the region of the plot containing Q1205-30 (marked q) and objects with S/N$>$ 30.

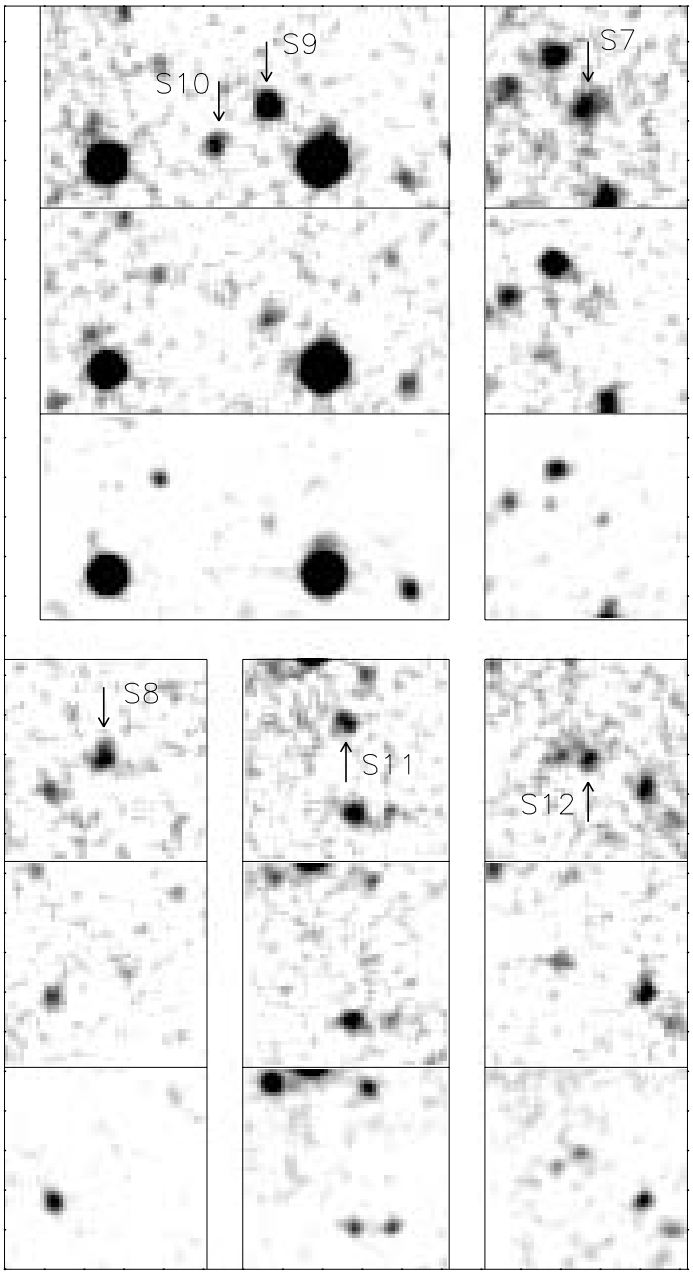

Figure 7.7: Extractions from the combined narrow band (top), B band (middle) and I band (bottom) for each of the six candidate emission line galaxies detected with S/N> 5 (see Sect. 7.3.3). In each field emission line galaxies have been marked with an arrow. The size of the square fields is 18x18 arcsec^2.

Chapter 8

STIS and NICMOS imaging of two z=3 Damped Lyα Absorbers

Møller P., Warren S.J., Fall S.M., Jakobsen P., Fynbo J.U., ApJ, in preparation

8.1 Introduction

At the present there are basically two ways to identify normal galaxies (i.e. galaxies that are not dominated by Active Galactic Nuclei) at high redshifts, namely either via the absorption they cause in the spectra of background QSOs (Damped Lyα Absorbers and Lyman Limit Systems), or via the break at the lyman limit in their spectral energy distributions (Lyman Break Galaxies). Whereas the sample of spectroscopically confirmed Lyman Break Galaxies (LBGs) now counts several hundred galaxies there are only a few high redshift Damped Lyα Absorbers (DLAs) for which a galaxy counterpart has been detected and spectroscopically confirmed to be at the redshift of the absorber. In this paper we present new results from Hubble Space Telescope STIS[1] and NICMOS[2] imaging for two of these, namely the z_{abs}=2.81 DLA towards PKS0528-250 and the z_{abs}=3.15 DLA towards Q2233+13.

The $z_{abs} \approx z_{em}$[3] DLA towards PKS0528-250 was detected with imaging in a narrow filter tuned to the redshifted Lyα line (Møller & Warren 1993; Warren & Møller 1996). With WFPC2 it was subsequently detected in continuum emission (Møller & Warren 1998). The DLA towards Q2233+13 was detected in continuum emission with the Lyman Break technique (Steidel et al. 1995) and subsequently spectroscopically confirmed to be at the redshift of the absorber by Djorgovski et al. (1996). In the following we will refer to these two DLA galaxy counterparts by the names, S1 and N1 respectively, given to them by the authors reporting on their detection. In this paper we in Sect. 8.3 determine the light profiles of S1 and N1 from the STIS and NICMOS imaging, and constrain the ages of their stellar population by comparison with spectral synthesis models. In Sect. 8.4 we compare our results with the current knowledge of morphologies and spectral energy distribution of LBGs and galaxies in the more local universe and present our conclusions. We adopt a Hubble constant of 100h km s^{-1} Mpc^{-1} and assume Ω_m=1(0.3) and Ω_Λ=0(0.7) through out.

[1]Space Telescope Imaging Spectrograph.

[2]Near Infrared Camera and Multi-Object Spectrometer.

[3]The absorption redshift z_{abs} only differs from the redshift of the quasar (z_{em}) by a few thousand km s^{-1} (Møller et al. 1998.)

Table 8.1: The observing log.

Field	date	setup	Exposure time (sec)
PKS0528-250	1999 Jun 17	STIS clear	2574
PKS0528-250	1998 Jul 20	NICMOS F160W	3840
Q2233+13	1999 Jun 9	STIS clear	2544
Q2233+13	1998 Aug 7	NICMOS F160W	3840

8.2 Observations

Table 8.1 gives the journal of HST-observations.

8.3 Analysis

8.3.1 Morphology

Contour plots of N1 and S1 from the STIS images, which trace the rest frame UV morphologies of $z = 3$ objects, are shown in the top plots of Fig. 8.1 and Fig. 8.2 respectively. As seen, the continuum emission from both S1 and N1 is emitted from extremely small and compact regions. Whereas S1 only consist of one core, consistent with the results obtained from deep WFPC2 imaging by Møller & Warren (1998), N1 consists of three sub-cores separated by 0.22±0.01 arcsec.

We fitted the light profile of S1 and of the sub-cores of N1 to profiles of the form $exp(-(r/r_s)^n)$ with a fitting programme developed by S.J. Warren. A value of $n = 1$ corresponds to an exponential-disc profile, whereas $n = \frac{1}{4}$ corresponds to a de Vaucouleurs profile. The fitting programme convolves trial model galaxy profiles with the PSF and minimizes the χ^2 of the fit to derive the optimal values of the half-light radius $r_{0.5}$ corresponding to r_s, n, and furthermore x, y, ellipticity, position angle and surface brightness at r_s. In the fit, regions near the QSO and hot pixels were excluded by a mask. For the three sub-cores of N1 we first fitted the brightest, central component with the two other components masked out, subtracted the fit from the original image, fitted the second brightest component and subtracting that fit from the original image, and re-fitted the central component. We then iterated 5-6 times until a stable solution was reached. Finally, we also fitted the faint third component. Since this component only contains about 14% of the total light, it was not necessary to fit this component iteratively.

The best fitting values of $r_{0.5}$, ellipticity and n derived in this fitting procedure are given in Table 8.2. Only for S1 and the brightest central component B of N1 was the signal-to-noise

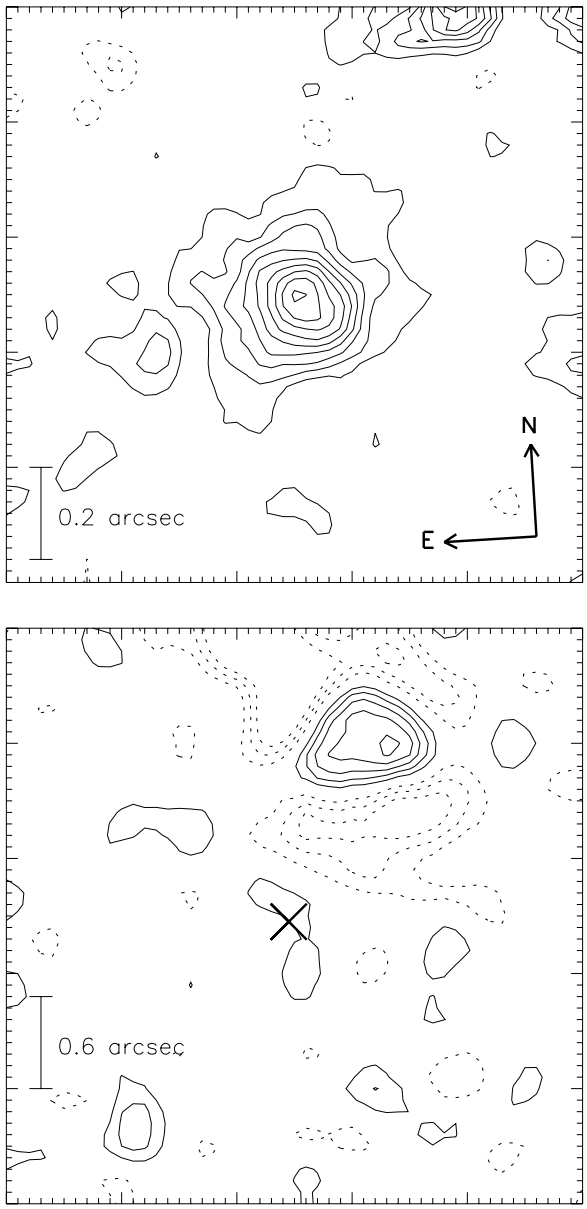

Figure 8.1: (Top) Contour plot of the galaxy counterpart of the DLA towards PKS0528-25 (called S1) from the STIS image. The size of the field is 1.3×1.3 arcsec. The contour levels are linear in flux. The orientation of the field is shown in the lower right corner. (Bottom) Contour plot from the NICMOS image. The orientation of the field is the same as in the STIS plot, but the field size is 3×3 times larger. The cross marks the centre of S1 in the STIS image. As seen, S1 is not detected in the NICMOS image. The residuals from the PSF subtraction can be seen in the upper right part of the plot.

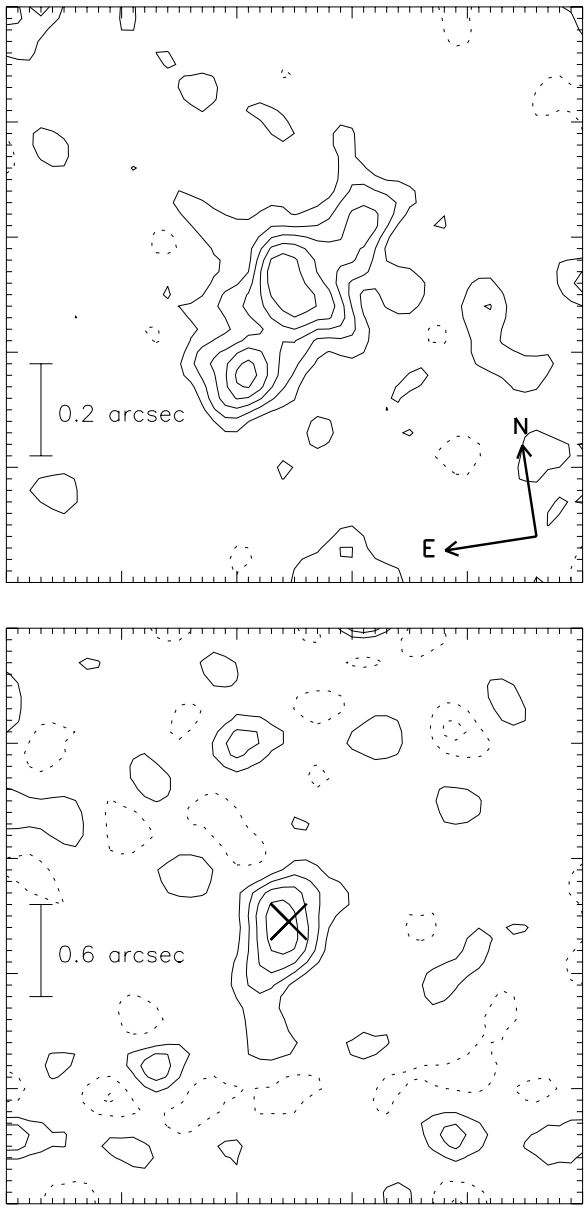

Figure 8.2: (Top) Contour plot of the galaxy counterpart of the DLA towards Q2233+13 (called N1) from the STIS image. The size of the field is 1.3×1.3 arcsec. As seen, the light profile of N1 consists of three components. The contour levels are linear in flux. The orientation of the field is shown in the lower right corner. (Bottom) Contour plot of N1 from the NICMOS image. The orientation of the field is the same as in the STIS plot, but the field size is 3×3 times larger. The cross marks the centre of the brightest central component in the STIS image.

Table 8.2: Measured profile parameters and impact parameter.

Object	$r_{0.5}$	ellipticity	n	impact par.
	arcsec			arcsec
S1	0.099±0.004	0.12±0.06	1.1±0.2	1.14±0.03
N1 A	∼0.04	-	-	2.55±0.03
N1 B	0.078±0.005	0.31±0.10	0.8±0.3	2.55±0.03
N1 C	∼0.03	-	-	2.55±0.03

high enough to get a well-constrained fit. Both of these are consistent with $n = 1$, .i.e. the profiles are best fit by exponential light distribution. For S1, the measured half-light radius is in good agreement with the measurement of Møller & Warren (1998), $r_{0.5} = 0.13 \pm 0.06$ for S1. To get an independent test of whether components A and C of N1 are extended we tried to model them as point sources with DAOPHOT II (Stetson, 1997). This process clearly showed that all three components are extended. The half-light radii are all around or smaller than than 0.1 arcsec, which at $z = 3$ corresponds to $0.34(0.54)\mathrm{h}^{-1}$ kpc.

The lower contour plots of Fig. 8.1 and Fig. 8.2 show extractions from the NICMOS images, that trace the rest frame optical morphologies of the objects. The images have the same centres and orientations as the upper plots, but the field sizes are nine (3×3) times larger. As seen, S1 is not detected in the NICMOS image, whereas N1 is detected at the 4σ level. We check whether the NICMOS profile of N1 is consistent with being the same as the STIS profile by smoothing and re-binning the model fit of N1 obtained from the fitting procedure described above to the resolution of the NICMOS data and then subtracting the scaled version that give the lowest χ^2. The residuals after this procedure were fully consistent with being sky noise.

8.3.2 Photometry and Spectral energy distributions

We measure the count rates in the NICMOS images in a circular aperture with diameter 1.13 arcsec. We calculate AB magnitudes or 2σ lower limits to the magnitudes (upper limit to the fluxes) by using the appropriate photometry keywords in the image headers as described in the HST data handbook. The results are given in Table 8.3. In Table 8.3 we have also collected measurements from the literature; in the case of S1 from Møller & Warren (1998) and in the case of N1 from Steidel et al. (1996b) and Djorgovski et al. (1996).

In Fig. 8.3 we compare measured AB magnitudes from Table 8.3 with spectral synthesis models from the Starburst99 package (Leitherer et al. 1999) reddened assuming a relation between the observed flux, f_{obs}, and the un-reddened flux, f_*, of the form $f_{obs} = 10^{-A_\lambda} f_*$,

Table 8.3: AB magnitudes for S1 and N1 in different filters. The references are 1) Møller & Warren 1998; 2) this work; 3) Steidel et al. 1996b; 4) Djorgovski et al. 1996.

Object	filter	λ_{cen} (μm)	AB magnitude	ref
S1	F450W[a]	0.450	25.7±0.3	(1)
	F814W[a]	0.837	25.2±0.3	(1)
	F160W	1.610	>25.1	(2)
N1	U_n	0.35	>27.55	(3)
	G	0.48	25.17	(3)
	$\mathcal{R}$	0.68	25.02	(3)
	F160W	1.610	24.5±0.3	(2)
	K[b]	2.2	24.00±0.3	(3,4)

[a] The F450W and F814W magnitudes from (4) have been changed to the AB system by using transformations given in the HST data handbook. Furthermore, we have applied an aperture correction of 0.15 mag.
[b] The K band magnitude has been transformed to the AB system by adding 1.95 (cf. the NICMOS ETC).

with an "extinction" A_λ on power-law form :

$$A_\lambda = A_V(\lambda/5500\mathring{A})^{-1}$$

Fig. 8.3a is for S1 and Fig. 8.3b is for N1. We derive the range of plausible models in the following way. First, we derive an estimate of the youngest stellar population that is consistent with the data. For S1 this is a 5Myr old single burst population reddened by $A_V \approx 0.15$. For N1, a 60Myr un-reddened single burst is the youngest population consistent with the data. These models are shown with full drawn lines in Fig. 8.3a and b. An estimate of the upper limit on the ages was obtained from models with continuous star formation. For S1, models of continuously star forming galaxies with age ~1Gyr reddened by $A_V \approx 0.10 - 0.15$ are consistent with the data. For N1, the numbers are ~3Gyr (which is more than the age of the universe at z=3.15) with $A_V \approx 0.2$. These models are shown with dashed lines in Fig. 8.3. In conclusion, it is not possible to strongly constrain the underlying the stellar populations with only broad band photometry. In conclusion, the ages of S1 and N1 are very poorly constrained.

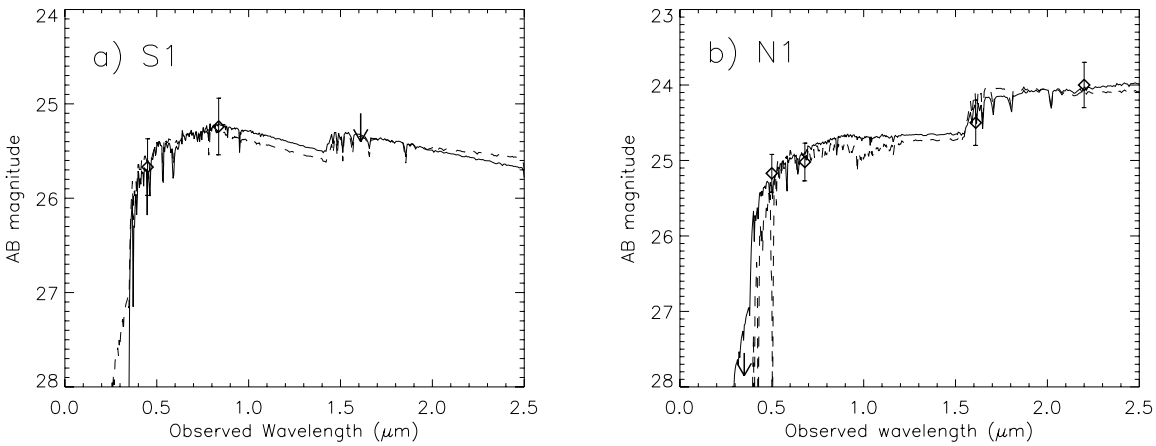

Figure 8.3: The spectral energy distributions of a) S1, and b) N1. Overplotted are spectral energy distributions of starburst models from Leitherer et al. (see text).

8.4 Discussion

The half-light radii of S1 and N1 are very similar to those derived for LBGs. Giavalisco et al. (1996a) and Steidel et al. (1996a) find from WFPC2 imaging that the LBGs generally consist of a few high surface brightness cores with half-light radii in the range 0.2-0.3 arcsec, sometimes surrounded by fainter more extended nebulosity. These measurements were not corrected for the effect of the WFPC2 PSF, and in several cases (17% in Steidel et al. 1996a) were their profiles best fit by point sources. In a WFPC2 study of compact galaxies in the Hubble Deep Field Phillips et al. (1997) derived a rough correction to the measured half-light radii, which simply consists in subtracting 0.15 arcsec in quadrature. This correction decreases the half-light radii by 20-50%. Hence, the somewhat smaller half-light radii we determine for S1 and the three components of N1 are most likely very similar to the "true" half-light radii of LBGs.

Concerning the spectral energy distributions, for the LBGs in the HDF-North the F450W-F814W AB colours range from -0.37 to 1.15 with a mean value of 0.35. The F450W-F814W AB colour of S1 of $0.43^{+0.30}_{-0.21}$ (derived by transforming the measurement in Møller & Warren (1998) to the AB system) falls well within the range of LBGs. F814W-F160W colours of LBGs are unfortunately not yet available in the literature. N1, being selected as a LBG, obviously has rest frame ultraviolet colours consistent with other LBGs. Moreover, its K-$\mathcal{R}$ colour is also similar to that of the other LBGs detected in the K by Steidel et al. (1996b). The brightnesses of both N1 and S1 is also within the range of the bright LBGs from ground based surveys.

8.4.1 Surface brightness effects

The ratio between the HI gas scale length of the DLAs, as measured by their impact parameters, and the light scale length, as measured by their half-light radii, is of the order 10–20. This is very different from the situation in local galaxies, where the gas only extends up to a few times the extension of the light. Whereas our data are deep, the $(1+z)^4$ dimming of surface brightness with redshift is a very strong effect. Hence, an important question is whether the compact STIS and NICMOS morphologies only reveals central high surface brightness regions embedded in lower surface brightness regions with extension more similar to the HI gas, but below the surface brightness detection limit of our data. Such central high surface brightness regions are also seen in local spiral galaxies (Carollo et al., 1997). A similar question was addressed by Giavalisco et al. (1996b) and Keel (1998), for rest-frame UV observations of high redshift galaxies, and here the conclusion was that due to surface brightness detection limits we do not expect to see the extended morphologies of present day galaxies. With our NICMOS data we can now address the same question for the rest-frame optical emission of S1 and N1. The 2σ surface brightness detection limit in our NICMOS observations are F160W(AB) = 22.9 mag.arcsec^{-2}. The corresponding surface brightness at z=3 is 16.9 mag.arcsec^{-2} at rest-frame 4000Å, corresponding to B. We compare this detection limit to present day galaxies in two ways. First, we (unphysically) assume that galaxies at $z = 3$ are identical to the present day galaxies. We compare to the V-band surface brightness profiles given in Carollo et al. (1997, their Fig. 2), and adopt B-V colours for spiral galaxies in the range 0.50–0.85 from Fukugita et al. (1995, their Table 3a). The conclusion is here that we would only have detected the central compact components of about half of that sample. Second, we allow for evolution in the following way. We calculate the brightness as a function redshift of a galaxy with a star formation history equal to the average over all galaxies as determined recently by Pei et al. (1999). We normalise the magnitudes to match the standard Freeman central surface brightness of 21.7 mag.arcsec^{-2} in the B-band. In this model the maximum rest-frame central surface brightness is about 20.0 mag.arcsec^{-2} and occurs at $z \approx 1$. At $z = 3$ it is about 21.6 mag.arcsec^{-2}, i.e. only 0.1 mag brighter than the present value. When comparing to the profiles given in Carollo et al. (1997) mentioned above and allowing for even ∼1 mag evolution, we would still only have detected the central compact components of those spiral galaxies.

Hence, we need deeper imaging in the infrared to test if high redshift galaxies also display more extended rest-frame optical, lower surface brightness emission.

Chapter 9

Clustering of galaxies at faint magnitudes

Fynbo J.U., Freudling W., Møller P., 1999, A&A, accepted

9.1 Introduction

The angular correlation function of galaxies $w(\theta)$ is still the most commonly used tool for investigating the evolution of clustering at high redshift . While a more direct measurement of the two point correlation is significantly more powerful (see e.g. Le Fèvre et al. 1996), its computation requires deep magnitude limited redshift surveys, which currently are not feasable at the faintest reachable magnitude limits. By contrast, the angular correlation function can easily be computed from photometric galaxy catalogs alone. With the availability of the Northern Hubble Deep Fields (HDF-N, Williams et al. 1996), the angular correlation function has been computed to an R magnitude of 29 (Villumsen et al. 1996, hereafter VFC, Colley et al. 1996). These studies suggest that the amplitude of the correlation function continuously decreases with the magnitude limit of the sample over a magnitude range of more than 10 magnitudes down to the faintest magnitude limits probed so far. The amplitude at an angular separation of one arcsec, $w(1'')$, seems to follow closely a power law $w(1'') \propto 10^{-0.27R}$(e.g. Brainerd et al. 1995).

Despite the apparent simplicity of computing the angular correlation function, a significant controversy has arisen about the magnitude limits at which the correlation function flattens. Measuring the correlation amplitude at a separation of 1 arcmin, Brainerd & Smail (1998) found that the correlation amplitude reaches a minimum for samples with limiting I magnitude of about 23 and stays flat for even deeper magnitude limited samples. On the other hand, the deeper HDF-N measurements at a separation of 1 arcsec found a continuously decreasing clustering amplitude down to the faintest magnitude limits. This discrepancy could be due to a number of different reasons such as biased field selection, different redshift selection through differences in the bandpasses, systematic errors in the determination of the clustering amplitude (e.g. due to gradients in the sensitivity of the detector), or simply random fluctuations in the correlation amplitudes. However, it could also mean a true discontinuity of the shape and/or amplitude of the correlation function at a magnitude of $I \approx 26$ or $R \approx 27$.

Before suggesting the existence of a discontinuity of the correlation amplitudes, several tests of the results should be carried out. First of all, both the ground based results and the HDF-N results should be verified by independent samples. Secondly, any apparent discontinuity should be tested with a single sample which covers the relevant magnitude range. Up to now, available ground based data have not been deep enough to overlap with the HDF results, which are only available for magnitudes fainter than $R \approx 26$. The current work addresses both of these points. We have used the southern HDF field to obtain an independent verification of the previous HDF-N results. In addition, we have used the "flanking fields" of the Northern and Southern HDFs (Williams et al. 1998) to derive a catalog over a larger area and thus allowing us to compute the $w(\theta)$ at brighter magnitudes from an HDF-like sample. Finally, we have used a sample of galaxies detected in a deep

ground based image, the so-called ESO NTT deep field (Arnouts et al. 1999) to compute $w(\theta)$ from ground-based data at faint magnitudes. The combined data sets allow us to derive correlation amplitudes from both HST and ground based data at identical magnitude bins, and thereby search for discontinuities in the correlation amplitudes as a function of magnitude.

In Sect. 9.2, we present the results from the HDF fields which include the Northern HDF, the Southern HDF and the flanking fields. In Sect. 9.3, we present new results from the ESO NTT deep field. In Sect. 9.4, we investigate the correlation amplitude as a function of magnitude by combining the new data with previous estimates in the literature. Finally, in Sect. 9.5, we discuss the results and present our conclusions.

9.2 HDF samples

9.2.1 HDF South : The galaxy catalog

We used the "drizzled" HDF-S images distributed by the *Space Telescope – European Coordinating Facility* archive. The galaxy catalog was generated using the SExtractor program (Bertin & Arnouts 1996). The catalog of Clements & Couch (1996) was used by VFC to compute $w(\theta)$ from the HDF-N images. In order to be able to compare our results with the results obtained from the HDF-N we use the exact same extraction parameters as input to SExtractor as those described in Clements & Couch. We use a minimum object extraction area of 30 pixels and a detection threshold of 1.3σ above the background. As a detection image we use a master frame calculated as the sum of the combined images taken with the F606W and F814W filters, which are similar to the R and I passbands respectively. As a detection filter we use a top-hat filter of 30 connected pixels. We checked the reliability of the extraction parameters by comparing the master frame with the output object image, which SExtractor optionally provides. We could not detect any tendency to find spurious objects in the vicinity of bright objects. The useful part of the combined mosaic frames are different between the HDF-N and HDF-S because the WFPC2 fields of view are slightly rotated relative to the mosaiced image which is aligned with the north/south direction. Therefore, we re-defined for each of the WF2, WF3 and WF4 CCDs useful areas from visual inspection of the master frame. Fig.9.1 shows the chosen areas. Only objects detected within the shown boundaries were used in the analysis. In order to exclude stars from the galaxy catalog we set an upper limit to the neural network star parameter in the output SExtractor catalog of 0.98, which excluded 20 objects. This is consistent with the number of stars expected for a field with the galactic latitude and depth as the HDF-S. Also we exclude saturated stars found by visual inspection from the galaxy catalog. There are not very bright stars in the HDF-S so we did not mask out any regions within the area shown in Fig. 9.1. We

Table 9.1: Survey data for the deep fields used in the determination of the twopoint correlation function

field	Area	I(complete)	R(complete)
	arcsec^2		
HDF-S	3.7	28.0	28.5
HDF-S FF	33.2	25.5	-
HDF-N	4.2	28.0	28.5
HDF-N FF	8.7	25.5	-
NTT	4.4	25.5	25.5

chose to use the Automatic Aperture Magnitudes (AAM) instead of the Corrected Isophotal Magnitudes (CIM), since the latter proved unstable. As well AAM as CIM are intended to give an estimate of the total flux of an object. The AAM is measured using an elliptical aperture with minor axis $b = 2.5r_1\epsilon$ and major axis $a = 2.5\frac{r_1}{\epsilon}$, where r_1 is the first moment of the light distribution and ϵ is the ellipticity.

The resulting number of galaxies in the galaxy catalog is 1346 with 456 in the WF2 field, 530 in the WF3 field and 360 in the WF4 field.

As zero-points for the photometry we use those released by the STScI with the WFPC2 HDF-S data for the VEGAMAG system. In the following we shall refer to the F606W and F814W as R and I respectively. Fig. 9.2 compares the galaxy counts for HDF-N and HDF-S. It is seen that the distributions are similar. In particular, the magnitude bins at which the number counts drop significantly due to incompleteness in the two samples are almost identical. The basic properties of the galaxy catalogs from the two fields as well as from other fields to be discussed below, are listed in Table 9.1.

9.2.2 Correlation function from the HDF south catalog

We extract from the galaxy catalog eight R-magnitude-limited samples with limiting magnitudes from R=25.5 to R=29.0 in 0.5 mag steps. As for the HDF-N, galaxies brighter than R=23 are excluded.

The angular correlation function $w(\theta)$ is estimated using the optimal estimator described by Landy & Szalay (1993) :

$$w(\theta) = \frac{DD - 2DR + RR}{RR}, \tag{9.1}$$

where DD is the number of galaxy-galaxy pairs, DR the number of galaxy-random pairs and RR the number of random-random pairs at the separation θ. We generate a set of 32000 random points distributed according to the Poisson distribution. The number of

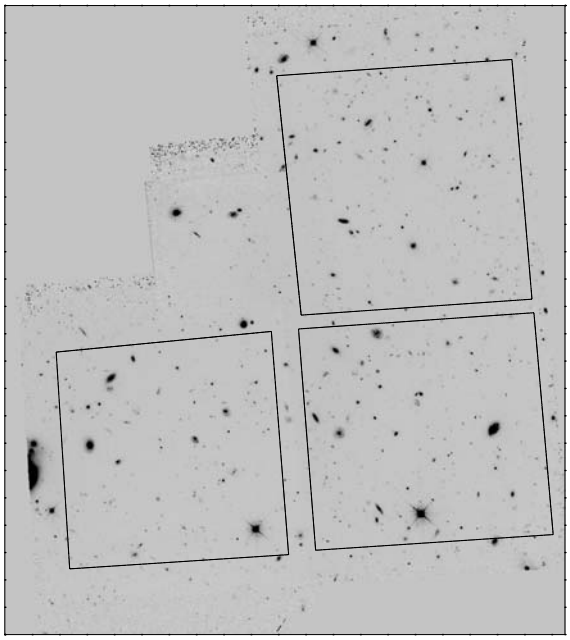

Figure 9.1: The WFPC2 HDF-S field showing the the used areas of each of the three Wide Field camera CCDs.

galaxy-random pairs and random-random pairs at a given magnitude limit are normalized to the total number of galaxy-random and random-random pairs respectively. The errors are calculated from Poisson statistics.

Since the mean density of galaxies has to be estimated from the sample itself, the integral of the correlation function over the survey area is forced to zero. This reduces the correlation $w(\theta)$ function by an amount C given by the integral :

$$C = \frac{1}{\Omega^2} \iint d\Omega_1 \, d\Omega_2 \, w(\theta), \tag{9.2}$$

where Ω is the solid angle of the survey area. C is commonly referred to as the 'integral constraint'. Assuming that $w(\theta)$ is a power law,

$$w(\theta) = A\theta^{-\gamma+1}, \quad \gamma = 1.8 \, , \tag{9.3}$$

then $C = 0.078(0.077, 0.080)A$ for the used parts of the WF2(WF3,WF4) area shown in Fig.9.1.

Fig.9.3 shows the observed $w(\theta)$ for the eight magnitude limits. The error bars represent 1 σ Poisson errors. The amplitude of $w(\theta)$ is determined by fitting

$$w(\theta) = A\theta^{-\gamma+1} \, - \, C, \quad \gamma = 1.8 \, , \tag{9.4}$$

which takes into account the integral constraint.

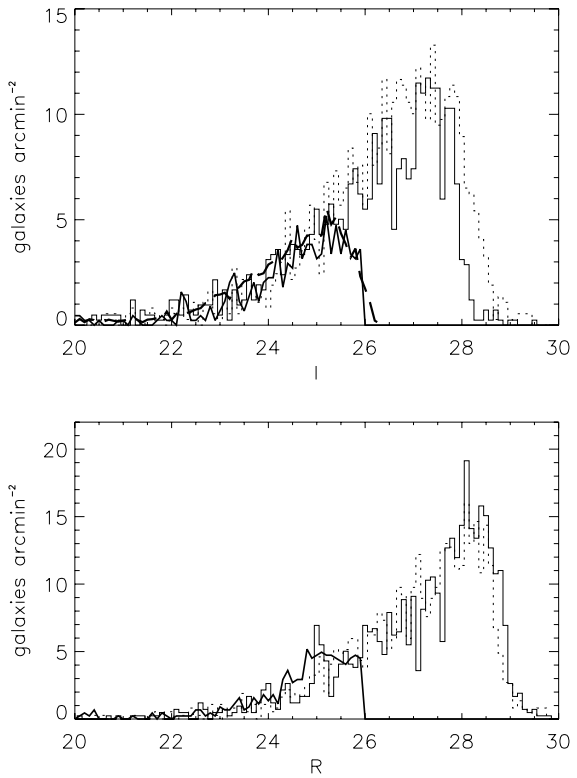

Figure 9.2: Comparison of the galaxy counts in 0.1mag bins in the HDF-N and HDF-S fields in the I and R bands. The solid histogram shows the counts for HDF-N and the dashed histogram shows the counts in HDF-S. In the top plot the fat long dashed line shows the galaxy counts in the HDF flanking fields and the fat solid line the counts in NTT SUSI Deep Field. The fat solid line in the lower plot shows the galaxy counts for the NTT SUSI Deep Field.

9.2.3 Flanking fields

The high resolution deep images of HDF fields are uniquely suited to investigate the correlation function at the faintest magnitudes. However, their small field of view includes too few brighter galaxies to provide useful overlap with ground based measurements of the correlation function. This situation can be improved by taking advantage of the HDF "flanking fields". These fields are contiguous to the HDF fields proper and have been taken during the HDF observing campaigns. We use the two deepest of the HDF-N flanking fields and the nine HDF-S flanking fields.

The HDF proper fields were chosen to avoid bright galaxies. It could be argued that this choice biases the measured correlation amplitude (Brainerd & Smail 1998). As the flanking fields have been chosen with proximity to the HDF fields as the only criterion, no bias related to the HDF proper field is present.

The flanking fields were only imaged with the F814W filter. There is a total of 14 fields. Three of the southern fields contained very bright stars. Rather than masking out these stars we decided not to use these frames in the analysis. Catalogs from the remaining 11 fields were generated in the same manner as for the HDF-S field. The average number counts as a function of magnitude are shown in the upper plot in Fig. 9.2. For magnitudes up to an I magnitude of about 25 the number per area is consistent with the one in the deep fields. The larger area therefore increases the sample in the brighter magnitude bins by almost an order of magnitude. The relevant parameters are again summarized in Table 9.1.

Finally, we measure the two point correlation function in the three bins 23 <I< 24.5, 23 <I< 25.0, and 23 <I< 25.5 in the same way as described in Sect. 9.2.2.

9.2.4 The correlation function from the combined Hubble Deep Fields

In Fig.9.4 we compare the HDF-S R band results with the results derived by VFC for the HDF-N. The triangles with 1σ error bars show the results for the HDF-S and the squares with 1σ error bars show the results from the HDF-N. For all magnitude bins the measurements from the two fields agree within 1σ. We conclude that any differences are due to random fluctuations, and therefore combine all the available data from the HDF-N and HDF-S projects to obtain our final estimate of the correlation amplitudes from the HDF fields. In Fig.9.5 we perform the same comparison for the I band, this time also including the measurements from the flanking fields. The measurements are in all bins consistent within 1σ, and we again combine all the available data from the HDF-N and HDF-S projects including the Flanking fields to obtain our final estimate of the I band correlation amplitudes from the HDF fields.

For the R band we determine $w(\theta)$ in the 8 magnitude bins R<25.5, R<26 ..., R<29. In these bins the number counts are not significantly influenced by incompleteness. For the I band we determine $w(\theta)$ in the 8 magnitude bins I<24.5, I<25,...,I<28. The flanking fields are here included in the measurement of $w(\theta)$ in the first three bins.

The determination of $w(\theta)$ and the power law fit is done as described in Sect. 9.2.2. We detect a positive correlation amplitude in all 8 bins in both R and I.

9.3 The ESO-NTT deep field

In order to verify that the correlation amplitudes we measured in the HST WFPC2 frames are not in some way due to properties of the WFPC2 instrument or HDF observing or reduction procedure, it is desirable to compare to a catalog of galaxies derived from deep high-resolution ground based observations. The ESO-NTT field (Arnouts et al. 1999), for

which the images are publicly available, is suitable for this purpose. A catalog of galaxies for this field has been provided by S. D'Odorico at the ESO website at http://www.eso.org/ndf. The field provides deep multi-colour imaging taken with good sampling of the PSF. The depth of the images is about 26.7 in R and 26.3 in I. The effective seeings of the co-added images are about 0.7-0.8 arcsec.

We determine the amplitude of $w(\theta)$ in the magnitude intervals 22–24.5, 22–25.0 and 22–25.5 for both the I and R filters. We use an area of 4.4 arcmin^2 confined by the pixel values 40 <x,y< 1020 (chosen to avoid edge-effects). For this area we derive an integral constraint of $C = 0.0468A$. Due to the small size of the NTT SUSI Deep Field we cannot determine the amplitude of $w(\theta)$ very precisely. Nevertheless, we do detect a positive correlation signal in all but one of the magnitude bins. The measured amplitudes of $w(\theta)$ are in all bins consistent with the measurements in the two HDFs within 1σ (see Fig. 9.6 and Fig. 9.7).

Stellar contamination of the sample can reduce the measured correlation amplitude. For a sample with a fraction $f_{\rm star}$ of galaxies, the measured correlation amplitude is reduced by a factor $\propto (1 - f_{\rm star})^{-2}$. Fortunately, the excellent seeing allows a firm galaxy/star discrimination. We follow Arnouts et al. in classifying as stars all objects with SExtractor classifier larger than 0.9 in the I band. This procedure removes about 5% of the objects in the field. For objects fainter than 24 the SExtractor classifier is not efficient, so we assume conservatively that about 5% of the objects used to measure the correlation amplitude are stars. In fact, the star counts are shallower at faint magnitudes than that of galaxies (Reid et al. 1996, their Fig. 1), which means that the star fraction at $I > 24$ must be smaller than for $I < 24$. Therefore, a conservative upper limit of the error introduced by stellar contamination of the catalog is 10%, which is significantly smaller than the random uncertainties.

9.4 The correlation amplitude as a function of magnitudes

The correlation amplitudes presented above overlap neither in magnitude nor scale with most such measurements from ground based data. Investigations of the correlation amplitude as a function of magnitudes which use these data therefore require knowledge of the power law index δ in order to compare amplitudes measured at different separations. The HST data presented here are consistent with the usual $\delta = 0.8$ power law for angular separations between 1 arcsec and 1 arcmin, but do not rule out steeper of flatter slopes. On the other hand, ground based data have been used to derive the shape of the correlations function at separations between 0.5 and 5 arcminutes (e.g. Postman et al. 1998), but it is not clear whether the slopes can be extrapolated to smaller separations. In the following investigation, we have adopted a slope of 0.8 in most cases. The uncertainty in the slope is probably the largest source of uncertainty in the comparison of measurements from different surveys.

Fig. 9.6 shows the measured amplitudes of $w(\theta)$ at 1 arcsec as a function of the limiting magnitudes of surveys in the R band from measurements by Brainerd et al. (1995), Roche et al. (1993), Couch et al. (1993) and Woods & Fahlman (1997). Where necessary (data from Roche et al. and Couch et al.), we have scaled original correlation amplitudes quoted in each paper to the amplitude at 1 arcsec by assuming a power law for the correlation function with $\delta = 0.8$. Similarly, Fig. 9.7 shows the measured amplitudes of $w(\theta)$ at 1 arcsec as a function of the limiting magnitudes of the surveys in the I band. The measurements of Postman et al. (1998), Brainerd & Smail (1998), Woods & Fahlman (1997), Benoist et al. (1999), Benoist et al. (in prep.) and Lidman & Peterson (1996) are included. Here, all the amplitudes except those from Woods & Fahlman (1997) and Postman et al. (1998) were extrapolated to a separation of 1 arcsec with $\delta = 0.8$. For the Postman et al. (1998) measurements, the data at 1 arcmin and 0.5 arcmin were extrapolated using the slope measured by the authors in the range 0.5 arcmin – 5 arcmin.

Both in Fig. 9.6 and Fig. 9.7, we show theoretical predictions of the expected correlation amplitudes. The models are identical to those shown by VFC, but with the assumed redshift distribution in the faint magnitude bins derived from the photometric redshift distribution of HDF-N galaxies by Fernández-Soto et al. (1999). The median redshifts adopted at magnitudes brighter than 26 in the R band are the same as those used by VFC. The models are specified by a present clustering length r_0 and and evolution parameter ϵ (see VFC for details). The models shown have a present clustering length of $r_0 = 4.0h^{-1}$ Mpc and assume no evolution of clustering (dotted line, ϵ=0), linear evolution of clustering (solid line, ϵ=0.8) or non-linear evolution of clustering (dashed line, ϵ=1.6).

Several data sets shown in Fig. 9.6 and Fig. 9.7 are in conflict with each other at the 5-7σ level. This reflects the fact that the main source of errors are systematic errors, while the error bars in most cases only include statistical errors. In particular at faint magnitudes, systematic uncertainties are hard to quantify. The disagreements appear to be larger in the I-band. This might be due to the fact that in the I band, variations in the effective filter bandpasses result in relatively large differences in the redshift distribution of extracted galaxy samples. Also, the limiting magnitude on the abscissa is somewhat depending on the limiting magnitudes at the *bright* end. However, as the galaxy counts (N) increases steeply with the limiting magnitude at the faint end (mag_{lim}, $\log N \propto 0.6\ \mathrm{mag}_{lim}$), the uncertainty due to different limiting magnitudes is small (the difference in the median magnitude of two galaxy samples with limiting magnitude 25 at the faint end and limiting magnitudes at the bright end of 20 and 24 is only about 0.5mag). More likely, however, the disagreement is related to the extrapolation from 1 arcmin scales to 1 arcsec scales. In Postman et al. (1998, their Table 3) it can be seen that the power δ seem to decline at $I > 21$ to smaller values than the canonical value 0.8 ($\delta = 0.7$ at $I = 22$ and $\delta = 0.5$ at $I = 23$), especially at the smallest scales 0.5 arcsec $< \theta <$ 5 arcmin. A similar trend was noted by Benoist et al.

(1999). Brainerd & Smail (1998) find at best fitting value of $\delta = 0.7$ at $I > 24.5$. A change in slope from $\delta = 0.8$ to $\delta = 0.5$ amounts to factor of 3.4 difference in the extrapolation from 1 arcmin scales to 1 arcsec scales. Due to these uncertainties, our current knowledge of the amplitude and shape of the correlation function in the range 1 arcmin $< \theta <$ 1 arcsec at the faintest magnitude limits reachable from the ground, I=23–25, is unfortunately still poor.

9.5 Summary and conclusions

From the data presented above we can draw the following conclusions.

- The clustering amplitudes measured in the HDF-N field have been confirmed with the independent sample from the Southern HDF. This rules out that the low amplitudes measured in the HDF-N field are due to some cosmological fluctuations. The HDF-N field seems to provide a fair sample of high-redshift galaxies.

- The clustering in the HDF flanking fields is consistent with the one measured from ground based samples at the bright end of the magnitude range, and with the ones measured in the HDFs at the faint end. This provides additional support to the view that the HDF fields represent indeed a fair view of the high-redshift universe.

- The measured correlation amplitudes in the ESO-NTT galaxy sample in magnitude bins which overlap those of the HDF sample are consistent with the HDF measurements. This observation verifies that correlations measured with WFPC2 are not due to some instrumental effects.

- The results plotted in Fig. 9.6 show a continuous decline of the amplitude of the correlation function in R. We do not confirm the Brainerd & Smail (1998) detection of a flattening in the I band at I=22–23.

- There is some indication of a flattening of the correlation amplitudes at the faintest levels ($R \approx 27$ or $I \approx 26$). Using models for the redshift distribution, VFC interpreted this flattening as evidence for linear evolution of the clustering of a galaxy population which at present has a correlation length of about $4h^{-1}$Mpc. The data presented in this paper are still in good agreement with this interpretation.

- Interpretation of Fig. 9.6 and 9.7 is difficult given the significant disagreement between data points from different studies. This disagreement could be caused by a change of δ as a function of magnitude and scale. To reach a final understanding of the two-point correlation function data compiled in this work, it therefore appears to be essential first to understand the detailed behavior of the *shape* of the correlation function.

Acknowledgments

We wish to thank C. Benoist and B. Thomsen for helpful discussions and C. Benoist for giving giving us access to some of his results from the EIS data prior to publication. We thank S. D'Odorico for making available the catalog from the NTT Deep Field. We thank the referee, T. Brainerd, for comments which significantly improved the manuscript. This work made use of the ESO/ST-ECF Science Archive Facility.

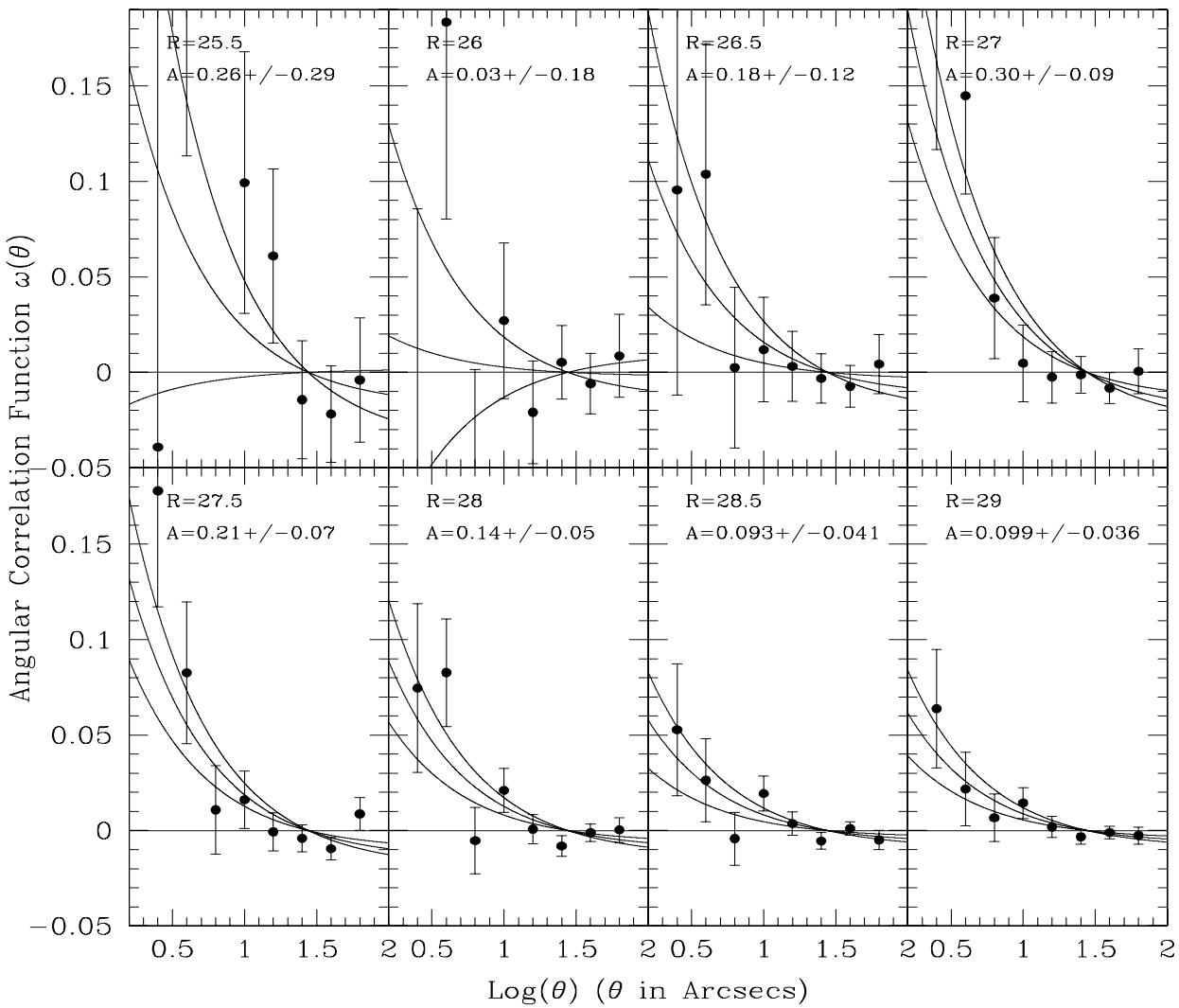

Figure 9.3: The measured angular correlation function for the eight magnitude bins. The limiting magnitude for each bin has been indicated on each plot. Also shown is the best fit to a function of the form given in Eq. (4) and the plus and minus 1σ fits.

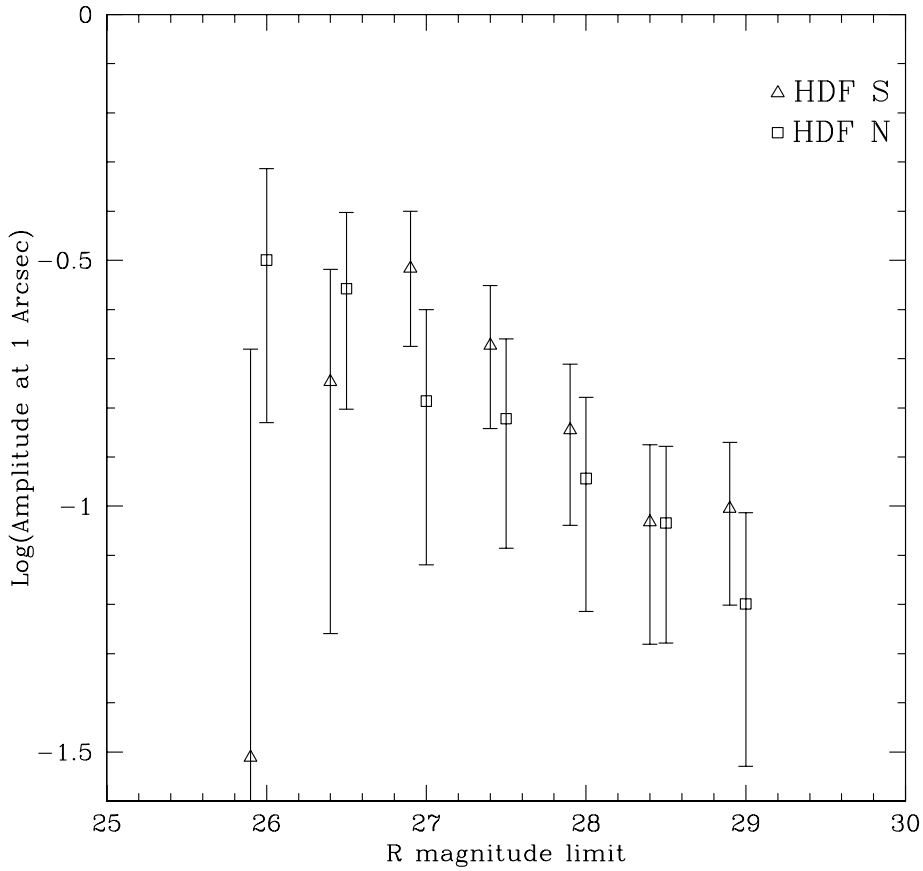

Figure 9.4: Comparison for the R band of the amplitude of the angular correlation function in seven magnitude bins for HDF-N (triangles) and HDF-S (squares). The data points for the HDF-S have been shifted 0.1 mag to the left to allow an easier comparison. In all bins do the measurements agree within 1σ.

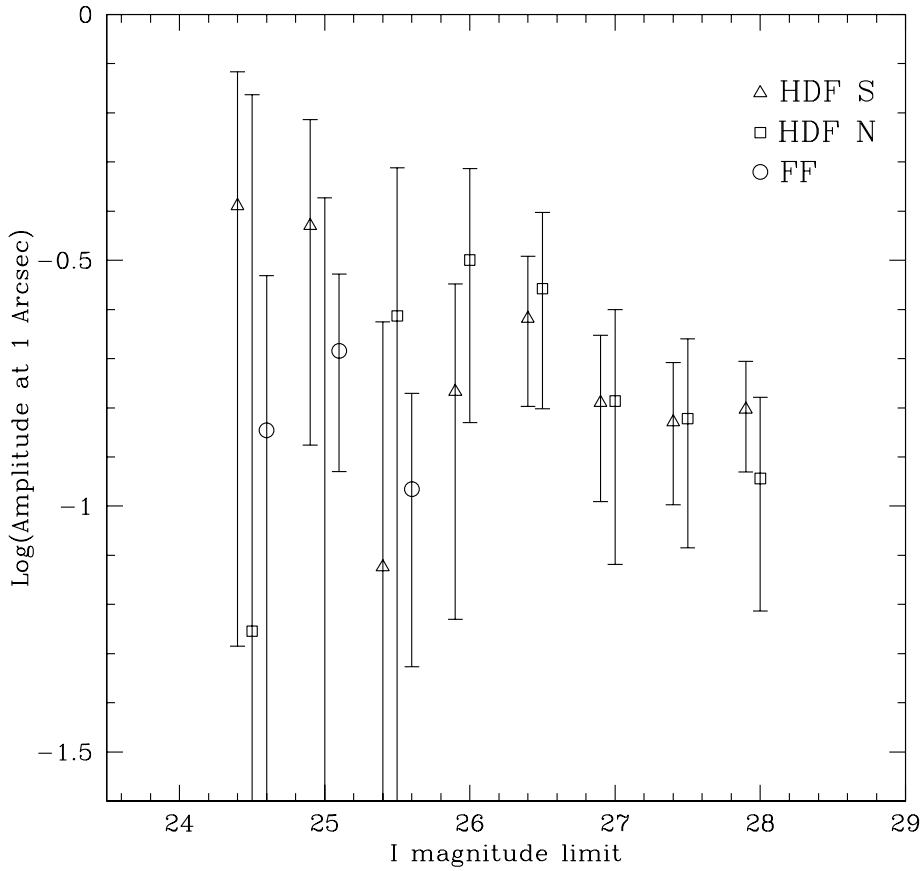

Figure 9.5: Comparison for the I band of the amplitude of the angular correlation function for seven magnitude bins for HDF-N (triangles), HDF-S (squares) and for the three first bins also the flanking fields (FF, circles). The data points for the HDF-S have been shifted 0.1 mag to the left and the points for the flanking fields 0.1 mag to the right to allow an easier comparison. In all bins do the measurements agree within 1σ.

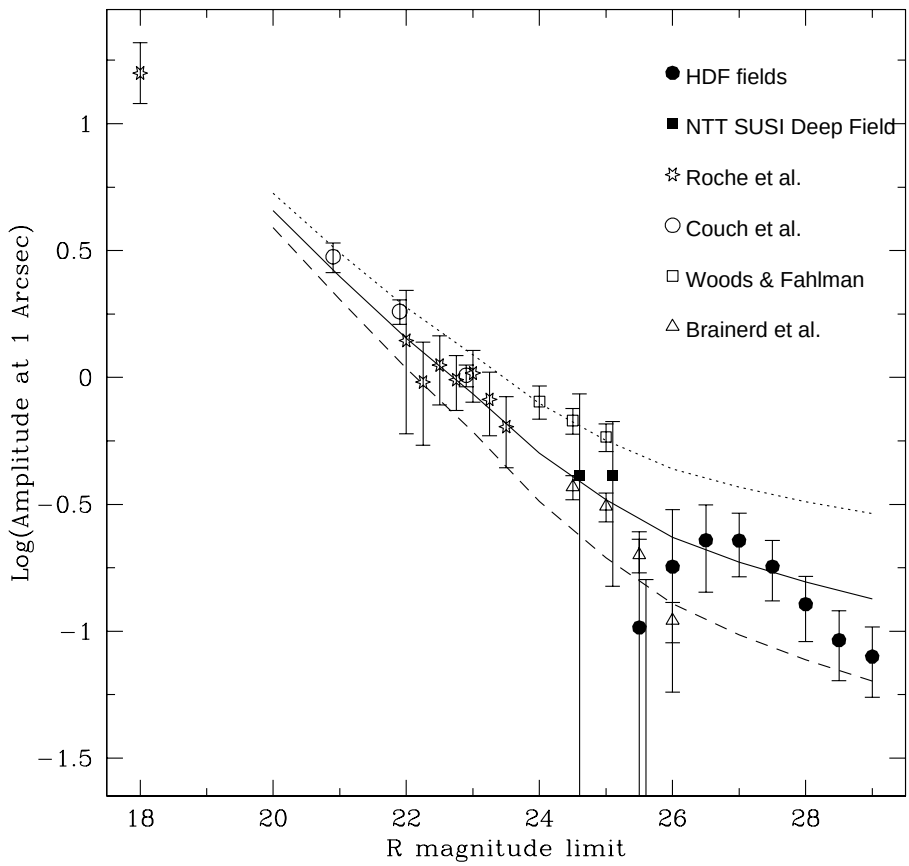

Figure 9.6: The amplitude of $w(\theta)$ at 1 arcsec as a function of the limiting R band magnitude for a number of ground based surveys and the measurements from the Hubble Deep fields presented in this paper. The superimposed curves are theoretical predictions for a population of galaxies with a present clustering length of $r_0 = 4.0h^{-1}$ Mpc and assuming no evolution of clustering (dotted line), linear evolution (solid line) as well as non-linear evolution of clustering (dashed line).

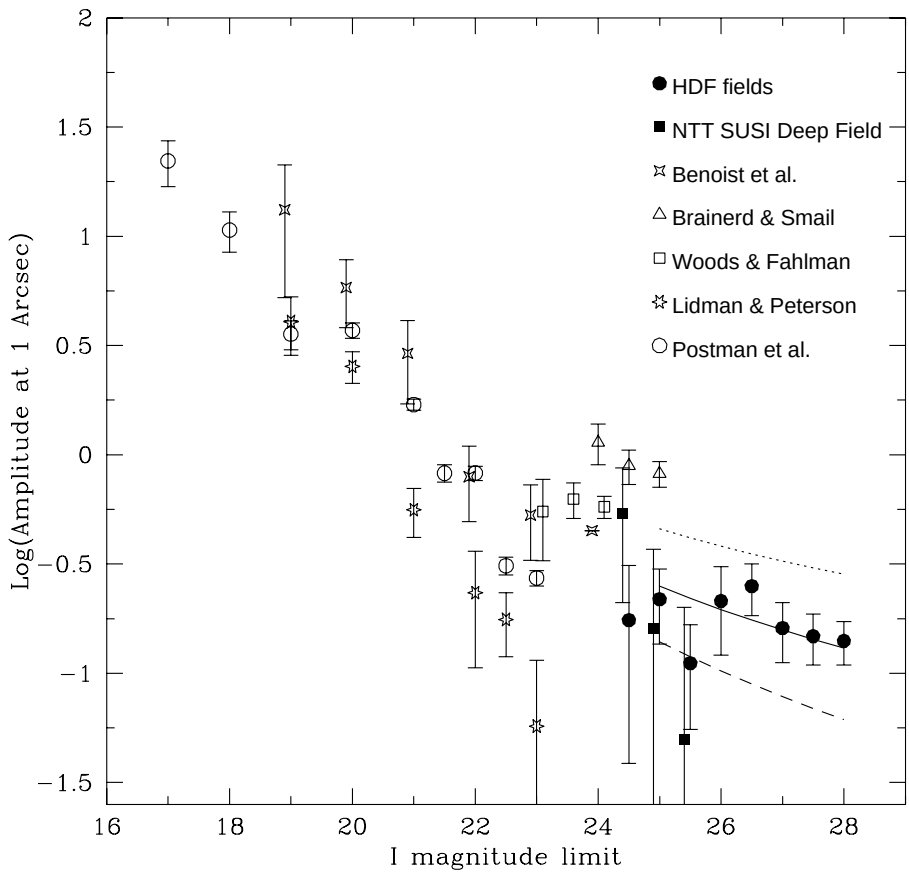

Figure 9.7: The amplitude of $w(\theta)$ at 1 arcsec as a function of the limiting I band magnitude for a number of ground based surveys and the measurements from the Hubble Deep fields presented in this paper. The superimposed curves are again the models with a present clustering length of $r_0 = 4.0h^{-1}$ Mpc and assuming no evolution of clustering (dotted line), linear evolution (solid line) as well as non-linear evolution of clustering (dashed line).

Chapter 10

Summary and Outlook

I now summarize the results of this thesis and briefly outline some of the perspectives for future work.

10.1 Summary

The main results of this thesis are the following

- The detection of extended Lyα emission from the $z_{abs} \approx z_{em}$ DLA towards Q0151+048A

The Lyα emission line from the DLA towards Q0151+048A (S4) was first detected spectroscopically with the NTT (Chapter 3). Subsequent deep narrow band imaging revealed that the Lyα emission region extends over an area of 25×12 kpc^2 (Chapter 4). This is an important discovery since it tells us that at least some DLAs are large and extended gas clouds with sizes similar to the size of our own Milky Way. It is difficult to asses to what degree the size and emission properties of S4 are affected by the proximity of the two QSOs. The extended morphology and large luminosity of S4 suggest that the proximity of the two QSOs is indeed important. In Chapter 4 we suggest that the neighbor QSO Q0151+048B is photoionising the side of S4 facing us. In this case the Lyα emission originates from regions where the optical depth for Lyα photons is 1, or in other words, Q0151+048 is highlighting a Lyman-limit system.

Chapter 5 describes our subsequent attempt to detect broad band emission from S4. The interpretation of the deep U, B and I–band imaging we obtained in the autumn of 1998 was complicated by the serendipitously detected very bright host galaxy of Q0151+048A. In itself the detection of the host galaxy is an interesting result, however, the presence of this extremely luminous and extended object makes the study of broad band emission from S4 almost impossible.

- The detection of extended Lyα emission from the $z_{abs} \approx z_{em}$ LLS towards Q1205-30

The candidate emission counterpart S6 of the Lyman Limit absorber towards Q1205-30 has size and morphology very similar to the size and morphology of S4. Furthermore, it is more luminous than the other candidate Lyα emitting galaxies in the field.

It is not possible from the NTT data to determine whether the source of Lyα photons in S6 is star formation within S6 or UV-photons from the background QSO.

- The detection of 6 Lyα galaxies in the field of Q1205-30

The deep narrow band image of the field of Q1205-30, probably one of the deepest narrow band images ever obtained, also allowed the detection of 6 other candidate Lyα emitting galaxies at projected distances of 156–444 h^{-1} kpc from the QSO. The 6 detections corresponds to a density of 14 arcmin^2 per unit redshift, which is significantly higher than that of LBGs in current ground based samples. We still do not know whether this high density of objects is due to an over-density of galaxies in the environments of QSOs or if the density of Lyα emitting galaxies is equally high in the field.

- Deep STIS and NICMOS imaging of two $z = 3$ DLAs

The deep STIS and NICMOS imaging of the DLAs towards PKS0528–250 and Q2233+13 revealed that the detected emission regions in the rest-frame UV of both DLAs are extremely compact. However, the surface brightness limit of the NICMOS data does not allow us to exclude that DLAs could also have the more extended emission regions known from low redshift galaxies.

- The measurement of the amplitude of the two point correlation function at very faint magnitudes

The measurement of the angular two-point correlation function $\omega(\theta)$ has been measured from the Hubble Deep Field North and South fields in the f606w and f814w filters down to magnitude levels 28–29. The interpretation of the resulting amplitudes is complicated by the large scatter in the measured amplitudes at brighter magnitudes and by the necessity to extrapolate ground based measurements to an angular scale of 1 arcsec. However, the measurements seem to be in rough agreement with a clustering length of 4–5 Mpc and with linear evolution.

10.2 Outlook

I end this thesis by discussing future studies.

- **Follow-up spectroscopy in the fields of Q0151+048 and Q1205-30**

Primarily we need to complete the study of the fields of Q0151+048 and Q1205-30 by performing follow–up spectroscopy.

We have already obtained a spectrum of S4, which shows a velocity gradient along the extent of the Lyα emitting region (Møller 2000). A higher resolution spectrum of S4 will show whether this gradient is due to rotation or perhaps due to more violent dynamical processes such as merging of several smaller galaxy subunits.

We also need to confirm whether the seven emission line objects S6–S12 in the field of Q1205-30 are indeed Lyα emitters at $z = 3.036$ or not and to measure the precise redshifts of both the QSO and S6. For this we have obtained two nights on the VLT for follow-up Multi-Object-Spectroscopy observations in March 2000.

There are generally a number of questions which, in my opinion, need to be addressed in order to improve our knowledge of the high–z galaxy population.

- **What do galaxy counterparts of high–z DLAs look like?**

We are currently addressing this question by obtaining deep images with STIS and NICMOS of 15 quasar fields showing 20 $z > 1.8$ DLAs in their spectra. The early results from this survey were presented in Chapter 8. 3 orbits of NICMOS imaging have been obtained in all 15 fields, and the STIS imaging with 2–8 orbits per field is 60% complete. The spectroscopic follow-up was initiated with the Very Large Telescope in August 1999. The early results from this observational run include the confirmation of at least one of our DLA candidates, namely the $z = 1.9205$ DLA towards Q2206-199. When all HST observations have been completed and when we have obtained follow-up spectroscopy for all candidates, this survey will in all likelihood have revealed the nature(s) of continuum-selected galaxy counterparts of high redshift DLAs.

We also plan to continue our narrow/broad band imaging searches for DLAs with the VLT. As narrow band filters for the VLT are very expensive (due to their size), we have proposed a multi-field efficient approach with several DLA-fields for the same filter. We have searched the literature and selected 4 groups with a total of 17 DLAs. Each of these groups can be covered by a single 25Å to 35Å narrow filter. Hence, instead of 17 we need only 4 narrow filters.

- **What are the properties of Lyα selected galaxies?**

We would like to know e.g. the number density, star formation rates, dynamical masses of the population of Lyα emitting galaxies discussed in the last section of Chapter 7.

We have proposed a deep large field survey with the Wide Field Imager (WFI) on the ESO 2.2m. Reaching a 5σ detection limit of 1×10^{-17} erg s^{-1} cm^{-2} for Lyα at $z = 3.134 \pm 0.012$ we expect to detect a few hundred Lyα emitting galaxies in two fields (one blank and one containing a $z = 3.13$ QSO).

The forthcoming VIMOS and NIRMOS instruments on VLT will allow spectroscopic follow–up observations of such a survey in both the optical (redshift confirmation) and in the infra-red (measurement of star formation rates and possibly dynamical masses from the widths of forbidden lines).

- **How biased is our understanding of the high–z galaxy population?**

The study of the high–z galaxy population has been revolutionized from a state about 5 years ago where we had less than a handful of detections of normal star forming galaxies till today where the Lyman-Break technique, narrow band Lyα imaging and also Gamma Ray Bursts (GRBs) and submm-imaging have allowed us to detect and study many hundreds of galaxies. However, although there is a lot of available information, our understanding still seems rather rough and "sketchy". One of the biggest problems is that we have great difficulty in connecting the measured light from galaxies to their mass, in particular at high redshifts. This is true both for observers and theoreticians, and reflects the fact that star formation and the feedback of star formation on the ISM are very poorly understood.

By comparing information from several independent surveys that select high–z galaxies with independent methods we can asses how complete each method is and hence obtain a better understanding. Hence, I think the way ahead will be to bring together information from the gas cross-section selected DLAs, the UV-flux selected LBGs, GRB-selected galaxies, dust-emission selected galaxies etc.; I certainly hope to be able to take part is this work in the future.

Acknowledgements

Many people have contributed to making my Ph.D. years a very fruitful and pleasant experience. First of all Palle Møller has not only been an excellent source of guidance, but also an invaluable friend since 1995 when I first went to STScI in Baltimore. My most sincere thanks goes to all in the Møller family : Liza, Shuala, Sharru and Palle, for their hospitality and friendship. Thanks also to Bjarne Thomsen for his constant support and his infinite knowledge of anything from Linux to the tides of the moon.

I would also like to thank all my officemates and friends at IFA over the years, Sarbani Basu, Uffe C. Bergmann, Henrik Bluhme, Hans Bruntt, Yuqin Chen, Thomas Dall, Steen Hannestad, Jakob Hansen, Michael Hyon-Hansen, Esben Nielsen, Ulrik Pedersen, Jakob H. Petersen, Lars Præstegaard, Thomas Tauris, Michael Viskum and many others, for a wonderful time. Thanks also to my officemates at ESO, Simona Mei and Joel Vernet. Also thanks to my friends from the Vatican summer school, especially Alok Kumar Durgapal, Thebe Medupe and Amina Helmi.

Next I wish to thank my collaborators, Steve Warren, Ingunn Burud, Kirsten Kraiberg Knudsen, Mike Fall and Wolfram Freudling from whom I have learned a lot.

Many thanks goes to my sister–in–law Claire and my twinbrother Hans for their support and for many corrections to my English.

During my undergraduate studies I received generous support from "Vennerne Hans Hansen og hustru og Bjarne Preetzmann-Aggerholm og hustrus legat til fordel for flittige og begavede studenter fra Kolding Gymnasium". My Ph.D. studies were funded in part by the Faculty of Natural Sciences, University of Århus and in part by "ESA følgeforskning" under the Danish Science Research Council (SNF). My sincere thanks to these funding agencies for their support.

Finally I would like extend my thanks to my family for their support throughout my education and to Charlotte for making every day a joy.

Appendix A

Some useful cosmological relations

In this appendix we setup a number of useful cosmological formulae, which are used in some of the chapters of this thesis. We wish to derive the dependency of angular distance, luminosity distance and the density of absorbers along lines of sight on cosmology for any standard $\Lambda = 0$ model and for Lemaître models. We follow the treatment given in Longair (1998), which uses the metric in the form :

$$ds^2 = c^2 dt^2 - R^2(t)[dr^2 + \mathcal{R}^2 \sin(r/\mathcal{R})^2 (d\theta^2 + \sin(\theta)^2 d\phi^2)],$$

where $\mathcal{R}$ is the radius of curvature of the universe, and R is the scale factor normalized to 1 at the present epoch. Hence, r will represent the metric distance at time t. Longair then introduces the distance measure D :

$$D = \begin{cases} \mathcal{R}\sin(r/\mathcal{R}) & \text{if } 1/\mathcal{R}^2 > 0 \\ r & \text{if } 1/\mathcal{R}^2 = 0 \\ \mathcal{R}\sinh(r/\mathcal{R}) & \text{if } 1/\mathcal{R}^2 < 0 \end{cases} .$$

The radial coordinate r can be derived as a function of z from the integral :

$$r = \frac{c}{H_0} \int_0^z \frac{dz}{\sqrt{(1+z)^2(\Omega_0 z + 1) - \Omega_\Lambda z(z+2)}},$$

where Ω_0 and Ω_Λ are given by the present mean density ρ_0 and the cosmological constant Λ respectively :

$$\Omega_0 = \frac{8\pi\rho_0 G c^2}{3H_0^2}, \quad \Omega_\Lambda = \frac{\Lambda c^2}{3H_0^2}.$$

$\mathcal{R}$ can be determined from the relation :

$$\frac{1}{\mathcal{R}^2} = \frac{\Omega_0 + \Omega_\Lambda - 1}{c^2/H_0^2}.$$

The luminosity distance D_L and the angular diameter distance D_A can now be derived as $D_L = D\,(1+z)$ and $D_A = D/(1+z)$. The volume element of a comoving slice of the universe

with solid angle $d\Omega$ at redshift z to $z + dz$ is given by :

$$\begin{aligned} dV &= d\Omega\, D^2 \frac{dr}{dz} dz \\ &= d\Omega\, D^2 \frac{dz}{\sqrt{(1+z)^2(\Omega_0 z + 1) - \Omega_\Lambda z(z+2)}}. \end{aligned} \tag{A.1}$$

Finally, the number density $\frac{dn}{dz}dz$ of absorbers with comoving space density $n_{abs}(z)$ and cross-section σ_{abs} along a line of sight in the redshift range from z to $z + dz$ is given by :

$$\begin{aligned} \frac{dn}{dz}(z) &= \sigma_{abs}\, n_{abs}(z)(1+z)^3 \frac{dr_{prop}}{dz} \\ &= \sigma_{abs}\, n_{abs}(z)(1+z)^2 \frac{dr}{dz} \\ &= \frac{\sigma_{abs}\, n_{abs}(z)\,(1+z)^2}{\sqrt{(1+z)^2(\Omega_0 z + 1) - \Omega_\Lambda z(z+2)}}. \end{aligned} \tag{A.2}$$

Bibliography

[1] Aragón-Salamanca A., Ellis R.S., O'Brien K., 1996, MNRAS 281, 945

[2] Aretxaga I., Terlevich R.J., Boyle B.J., 1998a, MNRAS 296, 643

[3] Aretxaga I., Le Mignant D., Melnick J., Terlevich R.J., Boyle B.J.,1998b, MNRAS L13

[4] Arnouts, S.; D'Odorico, S.; Cristiani, Fontana A., Giallongo E., 1999, A&A 341, 641

[5] Bahcall N.A., Fan X., 1998, ApJ 504, 1

[6] Bajtlik S., Duncan R.C., Ostriker J.P., 1988, ApJ 327, 570

[7] Barlow T.A., Sargent W.L.W., 1997, AJ 113, 136

[8] Baugh C.M., Cole S., Frenk C.S., Lacey C.G., 1998, ApJ 498, 504

[9] Benoist C., da Costa L.N., Olsen L.F., et al., 1999, A&A 346, 58

[10] Bertin E, Arnouts S, 1996, A&AS 117, 393

[11] Bessell M. S., 1990, PASP 281, 817

[12] Bower R.G., Lucey J.R., Ellis R.S., 1992, MNRAS 254, 601

[13] Braine J., Downes D., Guilloteau S., 1996, A&A 309L, 43

[14] Brainerd T.G., Smail I., 1998, ApJ 496, L137

[15] Brainerd T. G., Smail I. R., Mould J.R., 1995, MNRAS 275, 781

[16] Briggs F.H., Wolfe A.M., Liszt H.S., Davis M.M., Turner K.L., 1989, ApJ 341, 650

[17] Brown R.L., Vanden B.P.A., 1993, ApJ 412L, 21

[18] Bruzual G.A., Charlot S., 1993, ApJ 405, 538

[19] Bunker A.J., Warren S.J., Clements D.L., Williger G.M., Hewett P.C., 1999, MNRAS 309, 875

[20] Carballo R., Sánchez S.F., González-Serrano J.I., Benn C.R., Vigotti M., 1998, AJ 115, 1234

[21] Carollo C.M., Stivelli M., De Zeeuw P.T., Mack J., 1997, AJ 114, 2336

[22] Centurion M., Bonifacio P., Molaro P., Vladilo G., 2000, ApJ in press (astro-ph/0001109)

[23] Charlot S., Fall S.M., 1991, ApJ 378, 471

[24] Charlot S., Fall S.M., 1993, ApJ 415, 580

[25] Chen H.-W., Lanzetta K.M., Webb J.K., Barcons X., Fernández-Soto A., 1999, In the proceedings of the Xth Rencontres de Blois, "The Birth of Galaxies", in press

[26] Cimatti A., Di Serego Alighieri S., Vernet J., Marshall C., Fosbury R.A.E., 1998, ApJ 499, L21

[27] Clements D.L., Couch W.J., 1996, MNRAS 280, 43L

[28] Colina L, Bohlin R.C., 1994, AJ 108, 1931

[29] Colley W.N., Rhoads J.E., Ostriker J.P., Spergel, D.N., 1996, ApJ 473, L63

[30] Corbin M.R., 1990, ApJ 357, 346

[31] Courbin, F., Lidman, C., Magain, P. 1998, A&A 330, 57

[32] Couch W.J., Jurcevic J.S., Boyle B.J., 1993, MNRAS 260, 241

[33] Croft R.A.C., Weinberg D.H., Katz N., Hernquist L. 1998, ApJ 495, 44

[34] Croft R.A.C., Weinberg D.H., Pettini M., Hernquist L., Katz N., 1999, ApJ 520, 1

[35] Dickinson M, 1999, In: 'The Hubble Deep Field', ed. Livio M., Fall S.M. and Madau P., (May 1997 STScI Symposium), in press

[36] Djorgovski S.G., Pahre M.A., Bechtold J., Elston R., 1996, Nature, 382, 234

[37] Djorgovski S.G,, 1998, In: 'Structure and Evolution of the IGM from QSO Absorption Lines', ed. Petitjean P., Charlot S., (Editions Frontieres), p.303

[38] Ellison S.L., Lewis G.F., Pettini M., Chaffee F.H., Irwin M.J., 1999, ApJ 520, 456

[39] Espey B.R., 1997, Proceedings of IAU 159, Shanghai. Eds. Peterson and Chen.

[40] Espey B.R., Carswell R.F., Bailey J.A., Smith M.G., Ward M.J., 1989, ApJ 342, 666

[41] Evrard A.E., Summers F.J., Davis M., 1994, ApJ 422, 11

[42] Fall, S.M., Reviews of Modern Physics, 1979, 51, 21

[43] Fernández-Soto A., Lanzetta K.M., Yahil A. 1999, ApJ 513, 34

[44] Fixen D.J., Cheng E.S, Mather J.C., et al., 1996, ApJ 473, 576

[45] Fixen D.J., Hinshaw G., Bennett C.L., Mather J.C., 1997, ApJ 486, 623

[46] Foltz C.B., Chaffee F.H., Black J.H., 1988, ApJ 324, 267

[47] Forbes D.A., Brodie J.P., Grillmair C.J., 1997, AJ 113, 1652

[48] Francis P.J., Woodgate B.E., Warren S.J., et al., 1995, ApJ 457, 490

[49] Frayer D.T., Brown R.L., Vanden Bout P.A., 1994, ApJ 433L, 5

[50] Fukugita M., Hogan C.J., Peebles P.J.E., 1998, ApJ 503, 518

[51] Fukugita M., Shimasaku K., Ichikawa T., 1995, PASP 107, 945

bibitemF1Fynbo J.U, Møller P., Warren S.J., 1998, In: 'Structure and Evolution of the IGM from QSO Absorption Lines', ed. Petitjean P., Charlot S., (Editions Frontieres), p. 408

[52] Fynbo J.U, Møller P., Warren S.J., 1999a, MNRAS 305, 849 (Chapter 4)

[53] Fynbo J.U, Thomsen B., Møller P., 1999b, *The Messenger* 95, 32

[54] Ge J., Bechtold J., 1997, ApJ 477L, 73

[55] Ge J., Bechtold J., Walker C., Black J.H., 1997, ApJ 486, 727

[56] Giavalisco M., Steidel C. C., Macchetto F. D., 1996a, ApJ 470, 189

[57] Giavalisco M., Livio M., Bohlin R.C., Macchetto F.D., Stecher T.P., 1996b, AJ 112, 369

[58] Gilliland R.L., 1992, ASP conference series, vol. 23, 68

[59] Guillemin P., Bergeron J., 1997, A&A 328, 499

[60] Guzzo L., the 19th Texas Symposium on Relativistic Astrophysics and Cosmology, Paris, 1999, Eds.: J. Paul, T. Montmerle, and E. Aubourg (CEA Saclay), in press

[61] Haehnelt M.G., Steinmetz M., Rauch M., 1998, ApJ 495, 647

[62] Hamann F., 1997, ApJS 109, 279

[63] Hannestad S., 1999, MNRAS 309, 556

[64] Howk J.C., Sembach K.R., 1999, ApJ 523, L141

[65] Hu E.M., Kim T., Cowie L.L., Songaila A., Rauch M., 1995, AJ 110, 1526

[66] Hu E.M., Cowie L.L., McMahon R.G., 1998, ApJ 502, L99

[67] Hunstead R.W., Pettini M., Fletcher A.B., 1990, ApJ 356, 23

[68] Ivison R.J., Harrison A.P., Coulson I.M., 1998, A&A 330, 443

[69] Jimenez R., Friaca A.C.S., Dunlop J.S., et al., 1999, MNRAS 305, L16

[70] Jørgensen I., Franx M., Hjorth J., Van Dokkum P., 1999, MNRAS 308, 833

[71] Katz N., Weinberg D.H., Hernquist L., Miralda-Escudé J., 1996, ApJ 457, L57

[72] Kennicutt R.C, 1983, ApJ 272, 54

[73] Kennicutt R.C., 1989, ApJ 344, 685

[74] Kim T., Hu E.M., Cowie L.L., Songaila A., 1997, AJ 114, 1

[75] Kissler-Patig M., Forbes D.A., Minniti D., 1998, MNRAS 298, 1123

[76] Knudsen K.K., master thesis from Copenhagen Observatory

[77] Kolb E.W., Turner M.S., "The Early Universe", Addison-Wesley (1994), chapter 9

[78] Kulkarni V.P., Fall S.M., 1997, ApJ, 484, L17

[79] Landolt A.U., 1992, AJ 104, 340

[80] Landolt-Börnstein, 1982, volume 2b (Stars and Clusters), eds. K.-H. Hellwege, Springer, p.71-73

[81] Landy S.D., Szalay A.S., 1993, ApJ 412, 64

[82] Lanzetta K.M., McMahon R.G., Wolfe A.M., et al. 1991, ApJS 77, 1

[83] Lanzetta K.M., Wolfe A.M., Turnshek D.A., 1995, ApJ 440, 435

[84] Lanzetta K.M., Wolfe A.M., Altan H., et al., 1997, AJ 114, 1337

[85] Larsen G.B., Ph.D. Thesis, Århus University

[86] Le Brun V., Bergeron J., Boissé P., Deharveng J.M., 1997, A&A 321, 733

[87] Le Fèvre O., Hudon D., Lilly S.J., et al., 1996, ApJ 460, L1

[88] Lehnert M. D., Heckman T.M., Chambers K.C., et al., 1992, ApJ 393, 68

[89] Leibundgut, B., Robertson G., 1998, MNRAS 303, 711

[90] Leitherer C., Schaerer D., Goldader J.D., et al., 1999, ApJS 123, 3

[91] Levshakov S.A., Varshalovich D.A., 1985, MNRAS 212, 517

[92] Lidman C.E., Peterson B.A., 1996, MNRAS 279, 1357

[93] Longair M.S., Chapter 18 in : "Galaxy Formation", A&A Library (eds. I. Appenzeller et al.), Springer Verlag

[94] Lowenthal J.D., Hogan C.J., Green R.F., et al., 1991, ApJ 377, L73

[95] Lowenthal J.L., Hogan G.J., Green R.F., et al. 1995, ApJ 451, 484

[96] Lu L., Sargent W.L.W., Barlow T.A., Churchill C.W., Vogt S.S., 1996, ApJS 107, 475

[97] Lu L., Sargent W.L.W., Barlow T.A., 1997, ApJ, 484, L131

[98] Madau P., Ferguson H. C., Dickinson M. E., 1996, MNRAS 283, 1388

[99] Magain P., Courbin F., Sohy S., 1998, ApJ 494, 472

[100] McGaugh S., 1999, ApJ 523, L99

[101] McLure R.J., Kukula M.J., Dunlop J.S., et al., 1999, MNRAS 308, 377

[102] Meyer D.M., Welty D.E., York D.G., 1989, ApJ 343, L37

[103] Meylan G., Djorgovski S., Weir N., Shaver P. (1990), *The Messenger* 59, 47.

[104] Milgrom M., 1983, ApJ 270, 365

[105] Møller P., 1997, A&A submitted

[106] Møller P., 2000, In the proceedings of the conference "Astrophysics with the NOT", Turku, in press

[107] Møller P., Jakobsen P.., 1990, A&A 228, 229

[108] Møller P., Jakobsen P., Perryman M.A.C., 1994, A&A 287, 719

[109] Møller P., Kjærgaard P., 1992, A&A 258, 234

[110] Møller P., Warren S.J., 1993a, A&A 270, 43

[111] Møller P., Warren S., 1993b, In : "Observational Cosmology" ed. G.L. Chincarini, A. Iovino, T. Maccacaro, D. Maccagni, A. S. P. Conference series, 51, p.598

[112] Møller P., Warren S.J., 1996, in *Cold gas at high redshift*, eds. M.N. Bremer, P.P. van der Werf, H.J.A. Röttgering and C.L. Carilli, Kluwer Academic Publishers, p233

[113] Møller P., Warren S.J., Fynbo J.U., 1998, A&A 330, 19 (Chapter 3)

[114] Møller P., Warren S., 1998, MNRAS 299, 661

[115] Navarro J.F., Frenk C.S., White S.D.M., 1995, MNRAS 275, 56

[116] Oemler, 1976, ApJ 209, 693

[117] Oke J.B., 1990, AJ 99, 1621

[118] Osmer P.S., Porter A.C., Green R.F., 1994, ApJ 436, 678

[119] Pei Y. C, Fall S. M., Bechtold J., 1991, ApJ 378, 6

[120] Pei Y. C, Fall S. M., 1995, ApJ 454, 69

[121] Pei Y.C., Fall S.M., Hauser, M.G., 1999, ApJ 522, 604

[122] Petitjean P., Rauch M., Carswell R.F., 1994, A&A 291, 29

[123] Pettini M, Smith L.J., Hunstead R.W., King D.L., 1994, ApJ 426, 79

[124] Pettini M., Hunstead R.W., King D.L., et al., 1995, In: Meylan G. (ed.) QSO Absorption Lines, Springer-Verlag, Berlin, p.55.

[125] Pettini M, King D.L., Smith L.J., Hunstead R.W., 1997a, ApJ 478, 536

[126] Pettini M, Smith L.J., King D.L., Hunstead R.W., 1997b, ApJ 486, 665

[127] Pettini M., Kellogg M., Steidel C.C., et al., 1998, ApJ 508, 539

[128] Pettini M., Ellison S.L., Steidel C.C., Bowen D.V., 1999, ApJ 510, 576

[129] Phillips J., Weinberg D.H., Croft R.A.C., et al., 2000, ApJ submitted (astro-ph/0001089)

[130] Phillips A.C., Guzmán R., Gallego J., et al., 1997, ApJ 489, 543

[131] Postman M., Lauer T.R., Szapudi I., Oegerle W., 1998, ApJ 506, 33

[132] Priyamvada N., Pettini M., 1997, MNRAS 291, L28

[133] Prochaska J.X., Wolfe A.M., 1999, ApJS 121, 369

[134] Rao S., Briggs F., 1993, ApJ 419, 515

[135] Rao S., Turnshek D.A., preprint (astro-ph/9909164)

[136] Rauch M., 1998, ARA&A 36, 267

[137] Rauch M., Miralda-Escudé J., Sargent W.L.W., et al., 1997, ApJ 498, 7

[138] Reid I.N., Yan L., Majewski S., Thompson I., Smail I., 1996, AJ 112, 1472

[139] Rees M.J., Ostriker J.P., 1977, MNRAS 179, 541

[140] Roche N., Shanks T., Metcalfe N., Fong R., 1993, MNRAS 263, 360

[141] Robertson G., Leibundgut, B., 1998, In: 'Structure and Evolution of the IGM from QSO Absorption Lines', ed. Petitjean P., Charlot S., (Editions Frontières), p.271

[142] Sargent W.L.W., Boksenberg A., Steidel C.C., 1988, ApJS 68, 539

[143] Savaglio S., D'Odorico S., Møller P., 1994, A&A 281, 331

[144] Savaglio S., Panagia N., Stiavelli M., ApJ submitted (astro-ph/9912112)

[145] Schaeffer J.R., 1983, Ph.D. Thesis, Pittsburg University

[146] Sembach K.R., Steidel C.C., Macke R.J., Meyer D.M., ApJ 445, L27

[147] Silva D., Quinn P., 1997, *The Messenger* 90, 12

[148] Silva D., 1998, *The Messenger* 92, 20

[149] Songaila A., Cowie L.L., 1996, AJ 112, 335

[150] Spinrad H., Dey A., Stern D., et al., 1997, ApJ 484, 581

[151] Srianand R., Petitjean P., 1998, A&A 335, 33

[152] Steidel C.C., Hamilton D., 1992, AJ 104, 941

[153] Steidel C.C., Pettini M., Dickinson M, Persson S.E., 1994, AJ 108, 2046

[154] Steidel C.C., Pettini M., Hamilton D., 1995a, AJ 110, 2519

[155] Steidel C.C., Bowen D.V., Blades J.C., Dickinson M., 1995b, ApJ, 440, L45

[156] Steidel C.C., Giavalisco M., Dickinson M., Adelberger K.L., 1996a, AJ, 112, 352

[157] Steidel C.C., Giavalisco M., Pettini M., Dickinson M., Adelberger K., 1996b, ApJ 462, L17

[158] Steidel C.C., Adelberger K.L., Dickinson M., et al., 1999, In: "The Birth of Galaxies", the Xth Rencontres de Blois, in press

[159] Stetson P., 1997, "User's Manual for DAOPHOT II"

[160] Storrie-Lombardi L.J., Irwin M.J., and McMahon R.G., 1997, MNRAS 283, L79

[161] Terlevich R.J., Boyle B.J., 1993, MNRAS 262, 491

[162] Treu, T., Stiavelli, M., Casertano, S., Møller, P., Bertin, G., 1999a, MNRAS 308, 1037

[163] Treu T., Stiavelli M., Walker A.R., et al., 1999b, A&A 340, L10

[164] Tytler D., Fan X.-M., 1992, ApJS 79, 1

[165] Urbaniak J.J., Wolfe A.M., 1981, ApJ 244, 406

[166] Városi F., Dwek E., 1999, ApJ 523, 265

[167] Vernet J., et al., 1999, in prep.

[168] Villumsen J.V., Freudling W., da Costa L.N., 1996, ApJ 481, 578 (VFC).

[169] Warren S.J., Hewett P.C., Lewis G.F., et al., 1996, MNRAS 278, 139

[170] Warren S.J., Møller P., 1996, A&A 311, 25

[171] Weinberg D.H., Croft R.A., Hernquist L., Katz N., Pettini M., ApJ 522, 563

[172] Weinberg D.H., Davé Romeel, Gardner J.P., Hernquist L., Katz N., 1999, preprint (astro-ph/9908133)

[173] Williams R.E, 1972, ApJ 178, 105

[174] Williams R.E., and Weyman R.J., 1976, ApJ 207, L143

[175] Williams R.E., Brett B., Dickinson M., et al., 1996, AJ 112, 1335

[176] Williams R.E., Baum S.A., Bergeron L.E., et al., 1998, AAS 193, 7501

[177] Witt A.N., Gordon K.D., 1999, ApJ, in press

[178] Wolfe A.M., 1986, RSLPT 320, 503

[179] Wolfe A.M., Turnshek D.A., Smith H.E., Cohen R.D., 1986, ApJS 61, 249

[180] Wolfe A.M., , Lanzetta K.M., Turnshek D.A., Oke J.B., 1992, ApJ 385, 151

[181] Wolfe A.M., Lanzetta K.M., Foltz C.B., Chaffee F.H., 1995, ApJ 454, 698

[182] Woods D., Fahlman G.G., 1997, ApJ 490, 11

[183] Woudt P.A., Silva D., 1999, *The Messenger* 95, 18